INFORMATION TO USERS

This manuscript has been reproduced from the microfilm master. UMI films the text directly from the original or copy submitted. Thus, some thesis and dissertation copies are in typewriter face, while others may be from any type of computer printer.

The quality of this reproduction is dependent upon the quality of the copy submitted. Broken or indistinct print, colored or poor quality illustrations and photographs, print bleedthrough, substandard margins, and improper alignment can adversely affect reproduction.

In the unlikely event that the author did not send UMI a complete manuscript and there are missing pages, these will be noted. Also, if unauthorized copyright material had to be removed, a note will indicate the deletion.

Oversize materials (e.g., maps, drawings, charts) are reproduced by sectioning the original, beginning at the upper left-hand corner and continuing from left to right in equal sections with small overlaps. Each original is also photographed in one exposure and is included in reduced form at the back of the book.

Photographs included in the original manuscript have been reproduced xerographically in this copy. Higher quality 6" x 9" black and white photographic prints are available for any photographs or illustrations appearing in this copy for an additional charge. Contact UMI directly to order.

UMI

A Bell & Howell Information Company
300 North Zeeb Road, Ann Arbor MI 48106-1346 USA
313/761-4700 800/521-0600

SNOW AND ICE THICKNESS DISTRIBUTIONS IN THE SOUTH POLAR PACIFIC OCEAN

A

THESIS

Presented to the Faculty
of the University of Alaska Fairbanks

in Partial Fullfillment of the Requirements
for the Degree of

DOCTOR OF PHILOSOPHY

By

Ute Adolphs, M.S.

Fairbanks, Alaska
August 1997

SNOW AND ICE THICKNESS DISTRIBUTIONS IN THE SOUTH POLAR PACIFIC OCEAN

By

Ute Adolphs

RECOMMENDED:

Advisory Committee Chair

Department Head

APPROVED:

Dean of College of Science, Engineering and Mathematics

Dean of Graduate School

7-7-97

Date

ABSTRACT

Two sets of snow and ice thickness data of antarctic sea ice are presented in this study: drilling profiles on individual sea ice floes and spatially more extensive shipboard observations are investigated in order to reveal spatial and temporal characteristics of sea ice. The data were acquired between 1993 and 1995 in the Ross and the Amundsen/Bellinghausen Seas, two different regions of the south polar Pacific Ocean. Sea ice characteristics as well as their spatial distribution and temporal evolution are derived from the data sets. Strong regional trends are observed in ice thickness distributions of the drilling data. A spatial pattern is detected in the snow and ice thickness data as they were sorted according to distance from the ice edge. Flooding on sea ice floes is a widespread phenomenon in Antarctica and relevant for snow ice growth. Flooding is shown to correlate highly with snow loading, while it was much less distinctly correlated to ridging. Isostatic balance was tested on individual sea ice floes. Deviation from isostatic balance was shown to occur locally but was negligible on averaging scales of a few meters. With the help of ice thickness and roughness criteria an unbiased and reproducible ice classification scheme is developed. A combination of different methods from spectral and spatial statistics was used to describe the surface roughness characteristics of the three ice groups in detail. As a practical outcome from the roughness characteristics, air, water and ice surface drag coefficients were derived. With the goal to enhance sampling efficiency, the methodology of data sampling is investigated and optimized strategies are presented. Finally, a statistical ice thickness model managed to explain regional differences in the shape of the ice thickness distribution and therefore the relative significance of ice growth and development processes for a certain region.

TABLE OF CONTENTS

LIST OF FIGURES

LIST OF TABLES

ACKNOWLEDGMENTS

I am thankful to Paul Layer, Paul Reichardt and Joseph Kan, who made it possible for me to finish my thesis this last year. Financially I was supported by a thesis completion fellowship provided by the graduate school. Field work was covered by NSF grants OPP-9117721 and OPP-9316767. I want to thank the P.I. of these grants (Martin Jeffries) for the opportunity to take part in three Antarctic cruises of the RV. *N.B.Palmer*. For their valuable scientific advice and suggestions I want to thank the members of my committee which include Paul Layer, Lewis Shapiro, Willy Weeks and Gunter Weller. I am especially grateful to Willy Weeks, who was always willing to supply advice and helpful comments from long-distance and who also came up from Portland to Fairbanks for my defense. For their scientific comments on the first paper I am grateful to Will Harrison and Matthew Sturm. Many thanks also to a great number of people (science team and ASA personnel) who were doing ice observations and helped acquiring data on the sea ice floes. Finally I want to give my special thanks to the scientists who were working in the ice thickness group during the 1995 cruises: André Belem, Liz Chilton, Gwyneth Hufford, Ricardo Jaña, Erika Lawson, Ted Maksym, Joe Sapiano, Jennifer Simmons and Jane Stevens. They often worked extra hours on the ice, drilling and measuring holes. For moral support and scientific discussions I want to thank my husband Bernhard Rabus.

SEA ICE PROPERTIES DERIVED FROM SNOW AND ICE THICKNESS DISTRIBUTIONS IN THE SOUTH POLAR PACIFIC OCEAN

Introduction

Knowledge of the spatial and temporal thickness distribution of sea ice and its associated snow cover is important for understanding interaction processes between ocean and atmosphere in the Polar regions. Since the albedo of sea ice is significantly higher than the albedo of open water, sea ice concentration determines the radiation budget. Further, observations and model simulations provide evidence that the surface sensible heat fluxes from the open water (e.g. leads and polynyas) to the atmosphere are one to two orders of magnitude larger than from the surface of thick pack ice [*Meleshko et al.*, 1991].

Sea ice variability is also believed to be an indicator of possible climatic warming. For the Arctic a small decrease in sea ice extent has been observed, but no corresponding trend has been found for Antarctica [*Jones*, 1995]. In contrast to the Arctic, sea ice extent in the Antarctic may be dominated by sea ice motion and dynamics. Therefore, a constant sea ice extent could mask a net decrease in total sea ice mass that is due to a change in the ice thickness distribution.

Upward looking sonar records from submarines provide extensive and spatially representative ice thickness data for the Arctic. In contrast, Antarctic sea ice thickness information is largely limited to drilling data with extensive data sets being available mainly for the Weddell Sea. In this study I will investigate snow and ice thickness data, which were acquired in the Ross, Amundsen and Bellingshausen Seas during five cruises on board of the research vessel *Nathaniel B. Palmer* (NBP), between September 1993 and September 1995.

This thesis consists of three chapters which represent papers investigating various aspects of sea ice thickness data. An immediate goal of the thesis is to find spatial and temporal trends within the snow and ice thickness distributions. The adequate assessment of these trends is essential for monitoring future climate change. As a further goal, roughness measures are derived from the snow and ice thickness profiles and are shown to be relevant for ice classification and hereby indirectly connected to the question of an area averaged energy budget. Surface roughness also determines drag coefficients, which are important parameters for the turbulent energy exchange. Finally, with the goal to minimize future time and cost consumption of data acquisition, optimized sampling strategies of sea ice thickness are discussed. In a more global context, the various aspects studied in the following three chapters, provide an assembly of methods and methodology to monitor future global climate change with respect to Antarctic sea ice.

In the first chapter two different data sets are presented: drilling data (*Set A*), which were acquired on individual sea ice floes and continuous shipboard observations (*Set B*). The respective advantages and disadvantages of the two data sets in representing different sea ice regimes are presented. Spatial and temporal variability of snow and ice thickness is investigated in connection with thermodynamic and dynamic sea ice growth and development processes as well as oceanographic conditions. Flooding is a typical antarctic sea ice phenomenon and of major consequence for the snow ice formation. Sea ice surface wetness and flooding prior to and after drilling, are studied in relation to ridging and/or snow loading. This leads to questions of how severely isostatic balance can be disturbed and how the observed isostatic imbalances depend on the observation scale. Knowing to which extent isostatic balance is fulfilled is important for sea ice models including ice stresses and would be of major significance for inferring sea ice thickness from laser profiling.

The second chapter studies roughness characteristics of the snow, ice and ice underside surfaces of the sea ice drilling profiles. Roughness criteria are important for

classifying sea ice according to its degree of deformation. Furthermore, surface roughness is a crucial parameter that influences the turbulent heat transfer processes between the ocean and the atmosphere. A variety of different approaches to deriving roughness properties are presented in the second paper and are shown to appropriately describe the various aspects of roughness.

The objective of the third chapter is a statistical examination of the two data sets with respect to representativeness and robustness to subsampling. Subsampling errors of mean ice and snow thickness values are studied for different subsampling methods. The shapes of the probability density functions (PDFs) of snow and ice thickness are more sensitive to subsampling than are the corresponding mean thickness values. Whether this increased sensitivity causes a crucial loss of information when collecting less data leads to the more general question on what determines the shape of a PDF. The latter question is approached in two ways. First, theoretical statistical distributions are fitted to the real data ice thickness PDF's. Second a statistical ice thickness model is developed in order to simulate how sea ice growth and development processes influence the shape of an ice thickness distribution.

The following general implications for future Antarctic sea ice sampling can be drawn from the studies in these three chapters. With respect to monitoring sea ice thickness change future, sampling has to be done truely comparable with respect to region and position from the ice edge. Further, it would be best to sample more regions, possibly at the expense of sampling fewer floes per region and/or fewer, wider spaced data points per floe. However, roughness information would suffer as a consequence of wider spacing between drilling points. Also, for regional ice classification and energy budget calculation roughness determinations are needed over larger areas. In order to fulfill this last goal the development and improvement of alternative methods, such as laser profiling, ultrasonic minisubs or remote sensing is desirable.

Jones, P.D., 1995, Recent variations in mean temperature and the diurnal temperature range in the Antarctic, *Geophys.Res.Lett.*, 22, 1345-1348.

Meleshko, V.P., B.E.Sneerov, A.R.Sokolov and V.M.Kattsov, 1991, Sea ice anomaly impact on surface heat fluxes and atmospheric circulation as evaluated by the MGO GCM, Report of the Workshop on Polar Radiation Fluxes and Sea-Ice Modeling, Bremerhaven, Germany, November 1990, WMO/TD No.442.

I. Spatial and Temporal Variability of Snow and Ice Thickness in the South Polar Pacific Ocean

I.1 Abstract

Spatial and temporal characteristics of snow and ice thickness were determined for data, acquired during five cruises into the Bellingshausen/Amundsen and Ross Seas between September 1993 and 1995. When sorted in distance classes from the ice edge, snow and ice thickness showed a pattern of spatial and temporal variability that was linked to sea ice growth processes, sea ice motion and deformation as well as to oceanographic processes. Investigations of moisture and wetness at the snow/ice interface prior to drilling were correlated to freeboard measurements. Flooded locations correlated well with negative freeboard while sites of moist snow showed a lesser correlation. Wetness and flooding also showed high correlations to ratios of snowload to ice thickness; the relation to the amount of ridging was less conclusive. Isostatic balance was tested locally and on various spatial scales. The isostatic equation was formulated, including the slush densities, leading to a definition of a generalized density weighted snow/ice thickness ratio (GSI) which was used as a measure of the degree of isostatic balance. Deviations from isostatic balance occurred locally but decreased quickly on spatial averaging scales of a few meters. Sea ice was generally closer to isostatic balance in early winter as opposed to later in the season. Exact fits of the data points to isostatic equilibrium proved to be sensitive to the choice of both slush and snow density. As an output of adjusting the isostatic balance of a floe, a mean snow density for the floe was inferred. Using the isostatic equation an order of magnitude comparison between the depression of a floe due to snowload and bottom melting and its uplift due to ice growth was carried out. As a further result the contribution of snow ice formation to the overall ice growth was calculated.

I.2 Introduction

The variable extent and thickness of sea ice in the south polar ocean reflects a sensitive interaction with the Antarctic climate. The most relevant property of any sea ice cover is its insulating effect on the ocean by diminishing energy exchange with the atmosphere. Oceanic heat and moisture fluxes in the Arctic regions are reduced by up to two orders of magnitude in the presence of a winter sea ice cover. Variations in oceanographic and atmospheric temperatures as well as precipitation rates are also intricately linked to changes in the sea ice cover. In various studies [*Fletcher*, 1969; *Budd*, 1975; *Ackley and Keliher*, 1976; *Streten and Pike*, 1980; *Ackley*, 1981; *Carleton*, 1981; *Cavalieri and Parkinson*, 1981; *Gordon and Taylor*, 1975; *Gordon*, 1981; *Hibler and Ackley*,1983; *Sturman and Anderson*, 1986] evidence was found that increased energy flux through open water areas that develop within the sea ice can lead to enhanced cyclogenesis, thus affecting the atmospheric circulation and the global climate. Conversely, atmospheric temperatures and winds can affect processes like freezing, melting and transport of sea ice. Atmospheric conditions as well as sea ice growth and dynamics are mutually dependent on oceanographic circulation [*Jacobs and Comiso*, 1989; *Martinson*, 1993]. For instance, how much a sea ice field is set in motion by atmospheric forcing is sensitive to the magnitude of the oceanic sensible heat flux [*Martinson*, 1993]. A low oceanic sensible heat flux initiates more freezing and as a result more release of latent heat to the atmosphere and salt to the ocean. This causes destabilization and convection in the ocean and leads to more divergence in the ice pack. On the other hand, with a high oceanic sensible heat flux the ocean can balance atmospheric heat loss without growing ice. This stabilizes the ocean and dampens ice motions. Divergent and convergent motions within the pack, initiated as the result of atmospheric forcing, in turn affect thinning or thickening of the sea ice field.

The climatic influence of a sea ice field is further complicated through the presence of snow cover [*Ackley et al.*, 1990; *Ledley* 1991, 1993; *Massom et al.*, 1996; *Sturm et al.*,

submitted]. Snow acts as an insulator, thus keeping the sea ice warm and thin, but at the same time it also raises the albedo, thus leading to lower temperatures and thicker sea ice. The role of snow becomes even more ambiguous through the process of flooding [*Eicken et al.*, 1995a; *Lytle and Ackley*, 1996] which initiates brine and seawater infiltration into near-surface snow-layers. Once a snow layer is flooded it freezes and snow ice forms. As field studies have proven [*Eicken et al.*,1994; *Lange et al.*, 1990] flooding and snow ice formation are widespread in Antarctica and their impact on sea ice processes is important. *Lytle and Ackley* [1996] showed that the presence of liquid water in slush during the formation of snow ice initiates convective processes which increase the heat transfer from the base to the surface of an ice floe. This in turn may reduce the amount of bottom melting. Flooding also effects changes in the albedo (and hence the local radiation budget) of sea ice and alters its passive and active microwave signatures [*Drinkwater et al.*, 1993; *Hosseinmostafa et al.*, 1995]. Finally, the intrusion of seawater plays an important role in biological processes as it promotes the development of algae communities at the snow ice interface [*Fritsen et al.*, 1994; *Ackley and Sullivan*, 1994].

Compared to the Arctic, snow and ice thickness data of the Antarctic ocean are sparse as they are limited to drilling data to date. Several expeditions have been made in the Weddell Sea [*Wadhams et al.*, 1987; *Lange and Eicken*, 1991] and to East Antarctica [*Allison*, 1989; *Allison et al.*, 1993; *Allison and Worby*, 1994]. Between 1993 and 1995 the research vessel *Nathaniel B. Palmer* (NBP) made four voyages into the pack ice of the South Polar Pacific Ocean. The two main sectors which were visited are the Amundsen and Bellingshausen Seas and the Ross Sea embayment. This was a first opportunity for systematic snow and ice thickness measurements as well as for quantitative studies about the extent of flooding in these regions. For the Ross Sea which, next to the Weddell Sea, represents a region of great variability in sea ice extent [*Streten and Pike*, 1980], it was the first midwinter visit since Shackleton's historic voyage in 1902.

This study is a comparative spatial and temporal analysis of all snow and ice thickness data acquired during these cruises with a focus on the characteristics of the two major geographic areas. The methods used in collecting the data are described in section 2. In section 3 snow and ice thickness data are presented as well as results about the relation between wetness and negative freeboard. Finally sections 4, 5 and 6 deal with problems related to isostatic balance, including questions of depression, flooding and isostatic uplift and their connection to snow loading and ridging.

I.3 Fieldwork and Data

I.3.1 Geographical data coverage

Figure I.1 and Table I.1a show ship tracks, geographical areas covered, dates and seasons of NBP cruises. Cruise NBP 93 crossed the Bellingshausen and Amundsen Seas. Cruise NBP 94 started in the Amundsen Sea and ended by touching part of the north western Ross Sea. NBP 95-3 was an early winter Ross Sea expedition which was the first and only opportunity for the ice breaker to enter deep into the pack ice. Its closest approach to the continent was only 19 km from the Ross Ice Shelf at position 77.8° South and 179.5° West. Cruise NBP 95-5 is divided into two parts; part 1 was a late winter Ross Sea cruise and part 2 transversed the Amundsen and Bellingshausen Seas, thus covering a similar area to NBP 93.

I.3.2 Data and methods

Two fundamentally different sets of snow and ice thickness data were acquired for all these cruises.

Set A consists of ice thicknesses obtained by drilling holes at spacings of 2 m (for the 1993 and 1994 cruises) and 1 m (for the 1995 cruises) along transects that typically included 50 to 100 holes. One to three such profiles were obtained per floe. An attempt was always made to select a floe which was characteristic of the region in which the ship

was operating on that particular day. Transects were laid out in an effort to be representative for a given floe. Because of the common occurrence of features caused by the deformation of ice each transect typically crossed at least one ridge or raft.

Set B is a set of snow and ice thickness measurements which were made hourly while the ship was in motion. Twenty-five visual estimates of snow and ice thickness were made once every hour for individual floe pieces that were tipped over by the ship. A buoy of known diameter, which was attached to the side of the ship, was used as a scale.

Each of the two methods has its specific sampling bias [*Worby et al.*, 1994; *Jeffries and Adolphs*, in press]. *Set A* contains mostly medium thick floes with moderate ridging and does not adequately represent thin ice (<30cm) because in-situ sampling in thin ice areas was commonly dangerous. A benefit of the drilling method is the additional information about freeboard, a measure of how much the ice surface lies above or below the water surface, which in the latter case leads to flooding and snow ice formation. The lesser number of observations of *Set A* as opposed to *Set B* is balanced by a higher measurement accuracy of the drilling data (about 1 cm for snow and ice thickness and 0.5 cm for freeboard). *Set B* does not contain representative data about ridges and thick ice, since the latter were either avoided by the ship or more commonly were broken into pieces. However, it does adequately represent medium to thin ice with a slight bias in low concentration pack ice where thin ice was often pushed away rather than turned over. The lesser accuracy of method *B* (about 5 to 10 cm) as compared to method *A* is balanced by its ability to give more continuous geographical coverage and many more observations. Because of the large number of observations random errors cancel out. An overview of statistical parameters for *Set A* and *Set B* is given in Table I.1b. For the 1995 cruises the snow/ice interface of each drilling location was qualitatively examined prior to drilling and classified as dry, moist, wet or flooded. Finally, in addition to the snow and ice thickness data, which were acquired at each ice station, snow densities were measured at one to three sites per floe.

I.4 Results

I.4.1 Comparability and bias of the two methods

Figure I.2 shows the Probability Density Function (PDF) of the ice thicknesses measured by the two methods showing their extent of comparability and hence representativeness. Figure I.2c shows the PDF of ice thickness obtained by drilling (method *A*) during NBP 95-3. Figure I.2a displays the corresponding distribution of ice thickness which was sampled by method *B* for this particular cruise.

In order to compare the results of the two methods an attempt was made to remove their respective biases. For *Set A* a Rayleigh ridge criterion [*Wadhams and Horne*,1980, *Wadhams et al.*,1992] was applied to the data. In analogy to *Eicken et al.* [1995b] level ice was identified for sections with a minimal length of 20 m, which were bounded where the local ice thickness departed by more than 50% from the mean thickness over the section. Using this criterion, level ice can be separated from deformed ice as shown by the shaded areas in Figure I.2c. Figure I.2b shows the resulting level ice PDF of the drilling data (*Set A*). Subtraction of the thin ice bin (0-30 cm ice) from the *Set B* PDF in Figure I.2a and recalculation of mean and standard deviation (57 cm and 24 cm, respectively) shows a reasonably close agreement to the respective values for the level ice PDF of *Set A* (Figure I.2b).

It must be noted that the attempt to remove the biases of both methods occurred *a priori* and is only approximate. Even at significance levels ($\alpha<0.001$) statistical *t*- and *f*-tests reject the null hypothesis of equal mean and standard deviation, respectively. Due to the large sample sizes ($n > 2000$) for both data sets, their means and standard deviations should agree at the sub-centimeter level for the null-hypothesis to hold. Hence, the failure of the *t*- and *f*-tests suggests the presence of more unresolved systematic errors in one or both methods. Nevertheless it seems reasonable to assume that most of the initial bias present in both methods was indeed removed by this simple approach. Within their region

of overlap, between roughly 30 to 100 cm ice thickness, both methods will likely give representative estimates of the real ice thickness distribution.

I.4.2 Snow and ice thickness data grouped in distance classes

Snow and ice thickness data in two major geographical areas, the Ross Sea and the Bellingshausen/Amundsen Seas, can be distinguished and grouped into classes in terms of distance from the ice edge. Figure I.3 is a presentation of mean sea ice and snow thickness data sorted in such distance classes for both *Set A* and *Set B* Ross Sea data in early (Figure I.3a,b) and late winter (Figure I.3c,d). Figure I.4 is a similar presentation of the late winter data, which were obtained in the Amundsen and Bellingshausen Seas in 1993 and 1995. Values of standard deviations, σ, are given along the lines of mean snow and ice thicknesses. Standard errors are generally two orders of magnitude less than all thickness values. As σ of the snow thickness distributions is slightly smaller than for the ice distributions, the corresponding errors for the snow thicknesses are even smaller. Errors are slightly larger for the *Set A* data than for the *Set B* data, since they contain fewer ice observations per distance class.

A similar grouping in distance classes has been done by *Worby et al.* [1996] and by *Allison and Worby* [1994] for East Antarctic snow and ice. As presented in detail in *Jeffries and Adolphs* [in press] one can clearly discern three characteristic zones for both data sets of the Ross Sea in early winter (Figure I.3a,b). The first zone is the area in the vicinity of the continent at > 1200 km from the ice edge where the mean ice thickness is low. The second zone between 800-1200 km from the ice edge consists of thick ice for both *Set A* and *B* (Figure I.3 a,b). Zone 3 (< 800 km from the ice edge) is characterized by a distinctly lower mean ice thickness which declines towards the ice edge. Absolute values of ice and snow thickness are higher for the drilling data (Figure I.3a, c) than for the continuous shipboard measurements (Figure I.3b, d), but the tendency of relative variability with space is similar for both sets of each cruise. The graphs for the late winter

Ross Sea (Figure I.3 c,d) cover only the distances between 0 and 800 km, but they show the same trend as zone 3 of Figure I.3 a and b for the early winter cruise. The distance class between 0-200 from the ice edge appears only in the *Set B* data (Figure I.3 b,d) and shows distinctly lower ice and snow thicknesses than in zone 3.

During late winter sea ice conditions also restricted the research vessel to the outer pack ice (< 800 km from the ice edge) in the Amundsen and Bellingshausen Seas (Figure I.4). As in the Ross Sea (Figure I.3), there is a general increase in ice thickness from the ice edge towards the continent. However, contrary to the data from the Ross Sea where different distance classes are similar for *Set A* and *Set B*, the trend of thickening towards the continent in the Bellingshausen and Amundsen Seas is much more pronounced for the drilling data than for the continuous observations (Figure I.4c and d). Since the 1993 cruise in the Amundsen and Bellingshausen Seas only covers the relatively small area between 50 and 450 km from the ice edge, it is difficult to make comparisons between distance classes. As in the Ross Sea, there is also a distinct class of thin ice with thin snow cover in the *Set B* data (Figure I.4 b,d) for the Bellingshausen/Amundsen Seas at distances < 200 km from the ice edge. In the classes > 200 km, the *Set A* data contain higher mean ice and snow thickness values than *Set B* data (Figure I.4c, d) as well as a more pronounced increase towards the continent, especially in the class > 450 km. This pattern of greater difference between *Set A* and *Set B* in the Amundsen and Bellingshausen Seas can also be seen in Table I.1b.

I.4.2.1 Seasonal comparison of distance classes in the Ross Sea

As discussed in *Jeffries and Adolphs* [in press] the steep decline towards a very small mean ice thickness for both *Sets A* and *B* of the early winter Ross Sea (zone 1 in Figure I.3a,b) gives evidence of the fact that ice production takes place in near coastal polynyas and leads. From its origin near the continent the thin ice drifts then away towards the interior pack ice zone where it thickens by deformation and thermodynamic growth (zone

2). A similar observation, however not as obvious, was reported by *Allison and Worby* [1994] in East Antarctica. As further shown in *Jeffries and Adolphs* [in press] the marked difference in ice thickness between zones 2 and 3 can be explained by a combination of oceanographic and atmospheric influences. The boundary between zone 2 and 3 coincides approximately with the location of the continental slope which separates the colder continental shelf water from the deep ocean water to the north. This suggests that the lower oceanic heat fluxes over the continental shelf in combination with calmer sheltered atmospheric conditions in the Ross Sea embayment favor thermodynamic congelation ice growth in the interior pack (zone 2) as opposed to the outer pack ice (zone 3). The trend of similar relative variability with distance for both *Sets A* and *B* (Figure I.3 a and b) can be taken as a proof of the general comparability (section 2.2) of the two methods despite the difference in sampling range. An exception is the thin ice zone (zone 4) which only shows up in *Set B* (Figure I.3 b,d) and represents young ice near the ice edge consisting of pancakes and small cake floes.

The graphs of the late winter Ross Sea cruise (Figure I.3c, d) include only observations between 0-800 km from the ice edge which can be compared to zone 3 of the early winter cruise. Despite the three months time gap, there are no marked differences between the changes in snow and ice thickness in the *Set B* data of the late winter Ross Sea in comparison to the 0-800 km zone of the early winter Ross Sea. Both continuous data sets from the Ross Sea display a strikingly similar, seasonally independent pattern in the common zone of overlap from 0 to 800 km distance from the ice edge. A comparison of the drilling data (*Set A*) in the zone of overlap (200-800 km) also shows a similar tendency, but slightly higher ice and snow thickness values for the late winter set (Figure I.3a, c). This shows that medium to large ice floes which are suitable for drilling are thicker later in the season (Table I.1b). Since this thicker ice does not fall in the sampling range of the shipboard measurements, it is not reflected in *Set B*.

I.4.2.2 Annual comparison of distance classes in the Amundsen and Bellingshausen Seas

Mean ice thickness of the drilling data is high in the Amundsen and Bellingshausen Seas (Figure I.4a,c) as compared to the other cruises and to the less variable mean values of the *Set B* data (Figure I.4b,d, Table I.1b). This characteristic feature coincides with more frequent ridging in the *Set A* data of the Bellingshausen and Amundsen area as compared to other geographical regions (Table I.1b). It has already been suggested that the Bellingshausen and Amundsen Seas appear to be areas of heavy ridging [*Worby et al.*, 1994; *Jeffries et al.*, 1994].

Since sampling of deformed ice is one of the deficiencies of the shipboard measurements, ridges are hardly contained in the *Set B* data. Consequently increased rates of ridging turn up predominantly in the *Set A* data, mainly towards the inner pack where ice motion is more convergent. This also explains the steep increase in ice thickness in the class > 450 km in Figure I.4c. It is worth noting that ice thickness increases rapidly at this transition while snow thickness shows little change. This suggests that in this region ice thickness increases result from deformation and hence are not correlated with similar increases in snow thickness.

I.4.3 PDF's of ice and snow thicknesses and freeboard

Since the two Ross Sea cruises made it possible to study the same area twice within four months in 1995, it is useful to define a common geographic area (between 64.87° and 70.62° southern latitude) where the two cruises overlapped. The drilling data for this common area are shown in Figure I.5. Since a larger area was sampled in early winter than in late winter, Figure I.5 contains all the drilling data of late winter but only part of the *Set A* data for early winter. It is clear that there is a tendency for the snow and ice PDF's to become flatter and to shift towards higher thickness values later in the season. Mean snow and ice thickness values are also larger in late winter and there is a slight increase in the variance. A comparison between the two freeboard distributions (Figure I.5e and f) shows

a considerable number of freeboard measurements in the 0 to 5 cm bin in early winter and a larger number of negative than positive freeboard values in late winter.

Figure I.6 shows PDF's of the drilling data for the Bellingshausen and Amundsen Seas in 1993 and 1995. Data from the 1994 cruise (Figure I.1) are also included for comparison. Shaded areas indicate the amount of ridged ice in each particular ice thickness bin. One sees that deformation plays a much greater role in the Bellingshausen and Amundsen Seas (Figure I.6a and b) as compared to the late winter Ross Sea (Figure I.5d) and to cruise 94 (see also Table I.1b). The PDF's for the Bellingshausen and Amundsen area are broader and shifted towards larger ice thicknesses (Table I.1b) as compared to both the Ross Sea (Figure I.5d) and to NBP-94 (Figure I.6c). Furthermore they exhibit a slightly bimodal appearance, that is shared with the ice distribution of NBP-94.

Figure I.7 shows a comparison of *Set B* PDF's between the Amundsen and Bellingshausen Seas (Figure I.7a, b and c) and the Ross Sea (Figure I.7 d, e and f) in late winter 1995. Besides showing slightly higher mean values for the Amundsen Sea, the most obvious difference between the two geographical areas appears to be the shape of the PDF's with the distribution functions being more irregularly shaped in the Amundsen Sea as compared to the Ross Sea

I.4.3.1 Drilling PDF's, ridging and level ice

The increase in ice thickness shown in Figure I.5 (a and d) is undoubtedly due to the fact that by late winter sea ice has had more time to grow thermodynamically and to show thickness increases resulting from mechanical deformation than in early winter. An increase in snow thickness follows since older ice has also had more time to accumulate snow. A comparison between freeboard PDF's (Figure I.5c and f) shows that a high flooding potential apparent in early winter (bin 0-5cm) has been realized in late winter as shown by the large increase in the number of negative freeboard values.The increase in

flooding could also partly be attributed to the proportionately greater increase in snow thickness as opposed to ice thickness later in winter.

The drilling PDF's for the Bellingshausen and Amundsen Seas (Figure I.6a and b) show asymmetrical and irregular shapes at larger ice thicknesses. In section 3.2.2 it was inferred that deformation plays an important role in the Bellingshausen and Amundsen Seas. Therefore, one can interpret the asymmetric shape of the distribution functions in Figure I.6a and b as a consequence from and hence as an indicator of pronounced ridging. The two Ross Sea areas (Figure I.2c and Figure I.5d), which are clearly less ridged than the ice in the Amundsen and Bellingshausen Seas (Table I.1b), also show distinctly less flattened and more symmetrical ice thickness PDF's. The ice thickness distribution for cruise 1994 shows a mixture of Amundsen and Bellingshausen characteristics and Ross Sea characteristics. Like the Ross Sea distribution it shows less ridging and a confined range of ice thicknesses and like the Amundsen and Bellingshausen Seas there is a bimodal tendency and a high mean ice thickness value.

As can be seen in Table I.1b there does not appear to be a significant correlation between a high frequency of ridging and a high amount of negative freeboard. The Bellingshausen and Amundsen Seas, which were highly ridged in 1993 and 1995, show the least amount of negative freeboard. However, during the 1994 cruise and in the late winter Ross Sea the number of ridges were lowest and more than 50% of the freeboard was negative. Compared to the Weddell Sea [*Wadhams et al.*,1987; *Lange and Eicken*, 1991] the frequency of negative freeboards is similar in the Amundsen and Bellingshausen area but much higher in the Ross Sea.

Table I.1b shows similar values for level ice thicknesses from all the late winter cruises with the exception of the low value of the Bellingshausen and Amundsen Seas in 1993, where ridging was predominant. The value for the level ice thickness is similar to the ice thickness for undeformed first year ice found by *Lange and Eicken* [1991] in the North Western Weddell Sea in 1989. However it is higher than the corresponding value in

the 1989 Winter Weddell Sea [*Wadhams*, 1994]. The mean ice thickness for deformed first year ice for the Weddell Sea in 1989 [*Wadhams*, 1994] was similar to the mean thickness of ridged ice for the Bellingshausen and Amundsen Seas; the same value for 1988 found by *Lange and Eicken* [1991] was somewhat higher. Even if such a comparison has its limits due to differences in sampling methods it can be concluded that level ice thicknesses for all cruises, including the early winter Ross Sea, is at least as high as, if not higher than, the mean thickness of undeformed first year ice found in the Weddell Sea or in East Antarctica in late winter [*Allison and Worby*, 1994].

I.4.3.2 Comparison between the shipboard measurements of the Ross and Amundsen Seas in 1995 late winter

The *Set B* PDF's of the Amundsen and Bellingshausen Seas shown in Figure I.7 are irregular and slightly bimodal in the interior pack ice zone (class 200-400 km). In comparison the *Set B* PDF of the Ross Sea is close to symmetrical for all classes. The irregular shape of the Bellingshausen and Amundsen PDF suggests that continuous congelation ice growth plays a lesser role than rafting and ridging in this region. A comparison of the corresponding snow PDF also showed a more irregular and bimodal distribution for the Amundsen Sea as compared to the Ross Sea. This can be interpreted as a further sign of increased ridging and rafting as ridges favor a spatially variable snow cover with heavy build up of snow on their lee sides and only thin snow layers on their crests [*Sturm et al.*,submitted].

I.4.4 Investigations of flooding prior to and after drilling - spatial and seasonal differences

As noted in section 2.2 all drilling locations of the 1995 cruises were qualitatively examined prior to drilling and classified as dry, moist, wet or flooded. The results of this examination will be presented in section 3.4.2. in order to study the relation between the degree of wetness before drilling and the freeboard after drilling. In this analysis the

influence of the field party and their activities on the measurements may be a non-negligible factor. For that reason an upper limit of this influence is calculated in section 3.4.1.

I.4.4.1 Estimation of the depression of a floe due to the weight of the field party

Two cases are considered. First, the sea ice floe is viewed as a rigid plate which is depressed by the weight of the field party due to simple isostatic balance. In a second, much more realistic case, the elasticity of the floe is taken into account by assuming the floe to be a two-dimensional elastic plate and calculating its flexure in response to an external load.

Case 1: Consider a rigid, quadratic floe of sidelength 100 m; if an upper limit of 20 persons with average weight of 75 kg is assumed, the corresponding isostatic depression Δw is

$$\Delta w = \frac{20 \times 75 \text{ kg}}{(\rho_w - \rho_i)(100 \times 100 \text{ m}^2)} = 0.15 \text{ cm},$$

with $(\rho_w - \rho_i) = 0.1$ g cm^{-3} being the difference between the densities of water and ice.

Case 2: The ice floe is now assumed to be a two-dimensional elastic plate (horizontal coordinates x-y) on a fluid medium [*Parmerter*, 1974]. The corresponding plate equation for the vertical deflection $w(x)$ due to an external load $q(x)$ [*Turcotte*, 1982] is

$$D\frac{d^4w}{dx^4} + (\rho_w - \rho_i)gw = q(x). \qquad (1)$$

Here $g = 10$ N/kg is the earth acceleration and D is the flexural rigidity, defined as

$$D = \frac{Eh^3}{12(1-\upsilon^2)},$$

with h being the plate thickness, E is the Youngs modulus and υ the Poisson ratio of sea ice. Typical values for first year ice are $E = 3 \times 10^4$ Ncm^{-2} and $\upsilon = 0.3$ [*Parmerter*, 1974].

A load concentrated along a line in the y direction at $x = 0$ representing people along the drilling profile is assumed so that

$$q(x) = V_o \delta(x),$$

with $\delta(x)$ being the Dirac delta function. This gives a maximum deflection w_{max} (at $x = 0$) of

$$w_{max} = \frac{0.5 V_0 \alpha^3}{4D}. \qquad (2)$$

with α, the flexural parameter being equal to

$$\alpha = \left[\frac{4D}{(\rho_w - \rho_i)g}\right]^{\frac{1}{4}}.$$

To obtain an upper limit for w_{max} a minimum floe thickness of $h = 40$ cm and a field party of 20 persons, uniformly distributed along a 50 m line, is assumed. The latter gives

$$V_o = \frac{20 \times 750 \text{ N}}{50 \text{ m}} = 300 \frac{\text{N}}{\text{m}}$$

for the line load and a value of $\alpha = 9.2$ m for the flexural parameter. The resulting maximum deflection is

$$w_{max} = 1.6 \text{ cm}.$$

and w_{max} depends linearly on the number of persons and is proportional to $h^{-3/4}$. This means that for the same problem, 10 persons would still cause a deflection of 0.8 cm whereas the deflection would be still 0.95 cm for a mean floe thickness of 80 cm (which is a more realistic average value).

The conclusion is that the influence of the field party seen in the picture of rigid isostatic depression is negligible. However, considering typical freeboard values of -1 to +3 cm, the field party can have a noticable impact on the locally measured freeboard if the floe is treated as an elastic plate.

I.4.4.2 Freeboard statistics of the wetness groups

Figure I.8 shows the freeboard distribution functions for the early winter Ross Sea cruise (column 1), the late winter Ross Sea cruise (column 2) and the late winter Amundsen Sea cruise (column 3) for all wetness groups. Wetness increases in descending order from dry to slushy and/or flooded locations. In this investigation group 3 (slushy and/or flooded) shows the most obvious results (Figure I.8 j,k,l); most locations which were flooded or slushy had negative freeboards after drilling. In the late winter Ross Sea not a single positive freeboard was measured at any location belonging to group 3 whereas in the early winter (Figure I.8 j) and in the Amundsen Sea (Figure I.8 l) a few positive freeboards were observed. Negative freeboards also dominate the moist and wet groups (group 1 and 2, Figure I.8 d-i). The only exception is the moist group of the late winter Amundsen Sea, where only 45% of the freeboards were equal or below zero. Even locations that were dry prior to drilling show a substantial number of cases where freeboards were at or below zero (Figure I.8 a, b and c). For example, up to 25% of the freeboard measurements from the Ross Sea during late winter were negative and an additional 20% were zero. Less than 5% of the freeboards, observed at flooded locations in the Amundsen and Bellingshausen Seas in late winter were positive; a value that can probably be considered negligible. Group 2 (wet locations) show on the average 3-5% positive freeboards with a maximum contribution of 12% for the Amundsen Sea. Finally about 20% positive freeboards seem to be characteristic for the moist group (group1) excluding the Amundsen Sea where 55% of the holes measured had positive freeboard values.

I.4.4.3 Processes effecting the freeboard statistics of the wetness groups

The statistics shown in Figure I.8 suggests that several possible processes could be affecting local isostacy and hence flooding. For the flooded groups (group 3) of the early winter Ross Sea and the late winter Amundsen Sea (Figure I.8 j,l) 2 % and 5 % of the

sites showed positive freeboards. This finding could be associated with either young ice or deformation, as both can create conditions conducive to the formation of negative freeboards as compared to older and less deformed ice. Because young ice is thin and often consists of small floes, a horizontal influx of water could result from flooding over the floe edges, even if the ice surface is generally above the waterline. This occurrence of unstable edge regions can also be the result of deformation.

As seen in Figure I.8a, b and c a considerable percentage of dry locations show many freeboards that are equal to or lower than zero. This can have different reasons. Negative freeboard could have been caused by the weight of the field party in the course of the drilling action (section 3.4.1). Another possibility is that sea water was hindered in trickling into the snow layer due the low permeability of the underlying ice [*Massom et al.*,1996; *Eicken et al.*, 1994].

The number of positive freeboards within the moist and wet groups (groups 1 and 2) was also seen to be generally not negligible (Figure I.8d to i). At these locations, where the ice surface is still above the water level, water could have entered as the result of capillary suction. This could have been effected in detail by various processes. First, brine or seawater could have been expelled upwards through the brine channels into the snow cover on top of the ice surface. [*Lytle and Ackley*, 1996]. Further, small cracks, mostly formed as a by-product of ice deformation, could serve as openings for seawater to be sucked into the snow-cover by capillary pressure [*Massom et al.*,1996]. Finally the depression and flooding of neighboring areas could similarly (by vertically as well as horizontally acting capillary attraction) influence regions with positive freeboard. The occurrence of high salinity pockets in the snow above the level of flooding confirms the importance of these processes [*Sturm et al.*, submitted, *Massom et al.*,1996].

Inspection of Figure I.8 shows a good correlation between the degree of wetness to the snow/ice thickness ratio, and a less conclusive relation to the percent ridging. Snow to ice thickness ratios become progressively greater as the degree of wetness increases. A

larger amount of ridging is correlated with a higher degree of moisture for the early winter Ross Sea but there is an anticorrelation for the late winter Ross Sea. A slight tendency towards anticorrelation between these two variables is also seen for the Amundsen and Bellingshausen Seas. That ridging seems to reduce the overall percentage of negative freeboard values observed can be seen in Table I.1b, where areas with little ridging such as the Ross Sea in late winter show the highest percentages of negative freeboards (51%) (see section 3.3). This fact could be explained by the observation that the load distribution of keel and sail causes depression of the ice sheet adjacent to the ridge, thus inducing flooding, while the ridge itself is strongly uplifted (see section 3.4).

It can be concluded that there is effectively a 1 to 1 correlation between flooding and negative freeboard (results of group 3) with an uncertainty of up to 5%. The correlation is still fairly good for locations identified as wet prior to drilling which had only 5 to 10% of positive freeboard. Places which were classified as moist prior to drilling had an average of about 20% positive freeboard with maximum values up to 55%. The wetting of these locations is believed to occur by various processes which were initiated by the effect of capillary action. Locations which were dry prior to drilling were observed to have freeboards that are lower or equal to zero with percentages up to 45%.

I.5 Correlation between thickness variables on different spatial scales as indicators of isostatic balance

I.5.1 Relation between sail and keel

As indicated in the preceding sections, deformation (ridging and rafting) plays a important role in determining the characteristics of the snow and sea ice thickness distribution. The contribution of ridged ice to the total measured sea ice in the drilling data (*Set A*) was determined using the Rayleigh ridge criterion [*Eicken et al.*, 1995b, *Wadhams and Horne*,1980, *Wadhams et al.*,1992] and the percentages are given in Table I.1b. For

Arctic sea ice it was found [*Weeks et al.*,1980; *Wadhams and Horne*,1980; *Wadhams et al.*,1992; *Comiso et al.*,1991] that sail and keel thickness distributions of sea ice, selected with the Rayleigh ridge criterion, obey a negative exponential distribution of the form

$$n(h)dh = A_{sa/ke} \exp(-a_{sa/ke} h)dh \qquad (3)$$

where $n(h)$ is the probability that the thickness value h lies between h and $(h+dh)$. The amplitude A and the decay parameter a are parameters characteristic of the ice regime and the subscripts *sa* and *ke* refer to sail or keel. It has also been observed by *Dierking* [1995] that best fits to ridge height distributions of Antarctic sea ice are also achieved by negative exponentials.

When the sail and keel distributions of the ridged ice for the entire drilling data set of each of the cruises were fitted to equation (3), the values for the parameters $[A,a]$ given in Table I.2 were obtained. It can be seen that both A and a are larger for sails than for keels. This indicates a steeper exponential decline for the sail distribution with proportionally more values at lower thicknesses. The fit to equation (3) was very similar for all data sets with standard errors of one to two orders of magnitude smaller than the amplitude and generally smaller by two orders of magnitude than the decay parameter. Figure I.9a shows a strong linear correlation (r=0.99) between the amplitudes and the decay parameters for the keel distributions of the different cruises. A positive correlation was found between the two amplitudes A_{sa} and A_{ke} and a strongly linear correlation between the two decay parameters a_{sa} and a_{ke} can be seen in Figure I.9b (r=0.97).

A strongly linear correlation between the two decay parameters for Arctic sea ice was also found by *Wadhams et al.* [1992]. But in comparison to the Arctic values, the Antarctic amplitudes A presented here seem to be generally lower and decay parameters a are higher. Figure I.9a and b further indicate that the decay parameter of both sail and keel distributions as well as the underside amplitudes are visibly higher for the Ross Sea than for the Amundsen and Bellingshausen area. This probably reflects the fact that

distributions of heavily ridged areas tend more towards higher thicknesses, which in turn diminish the amplitude. The parameters A and a describe the shape of a distribution and hence are a measure of the degree of deformation of an ice field [*Wadhams*, 1994].

The generally good correlation between top and bottom parameters suggests that it should be possible to develop a useful transfer function between the sail and keel distributions. The practical value of obtaining such a transfer function is evident since it would allow one to measure sail profiles of large sea ice areas with a laser altimeter and use these to derive keel distributions. This would be especially useful for future sea ice sampling in Antarctica, where submarine data are not available and drilling data are sparse and difficult to attain. *Comiso et al.*[1991] and *Wadhams et al.*[1992] have successfully developed such a transformation suitable for regions of the Arctic, where sonar as well as lidar data were available. This was accomplished by making a scale transformation on the sail distribution with the density ratio

$$R = \frac{\rho_m}{\rho_w - \rho_m} \tag{4}$$

where ρ_w is the near surface sea water density and ρ_m is the mean density of the snow and ice given by

$$\rho_m = \rho_i h_i + \rho_s h_s \Big/ h_i + h_s$$

with ρ_i and ρ_s being densities of ice and snow and h_i and h_s being their thicknesses respectively. Via the isostatic relationship $< (h_{sa} + h_{ka}) > \rho_m = < h_{ka} > \rho_w$ with h_{sa} and h_{ka} being sail and keel thickness respectively and the brackets < > denote averaging, it can be shown that R equals the ratio of mean keel depth to mean sail height

$$R = \langle h_{ka} \rangle \Big/ \langle h_{sa} \rangle .$$

Conversion of a sail distribution into the corresponding keel distribution requires (i) stretching the x-axis by R to adjust the range of thickness and (ii) compressing the y-axis

by *1/R to* renormalize the distribution, which should then resemble the keel distribution. According to *Comiso et al.* [1991] a successful transformation means that the ice cover behaves as if surface features are mirrored on the underside but are magnified by the factor *R*.

Can a single *R*, calculated from the mean sail and keel apply to the distribution of a whole cruise? The scale transformation with this *R* should be generally more successful the more ice floes were isostatically balanced on an intermediate spatial scale. However, the exact reproduction of the shape of the keel distribution via such a transformation will also depend on the size of deviations from the local isostatic balance.

Table I.2 shows the values for R for the different cruises. It can be seen that they vary with geographic region and time and range from 2.9 to 3.8. Typical values of *R* for the Arctic range between 7.2 and 8.7 [*Comiso et al.*,1991; *Wadhams et al.*,1992], again dependent on the specific region. This shows that surface features are still enhanced on the underside of Antarctic ice but by about a factor 2 less than in the Arctic. Figure I.10a shows the keel distribution resulting from a sail transformation with factor *R* in comparison to the measured keel transformation for the drilling data of the second Ross Sea cruise (NBP 95-5). The agreement is encouraging with the transformed keel PDF being only slightly broader and flatter than the measured PDF. This tendency was generally observed for all cruises. The scale transformation generally worked better for the two Ross Sea data sets than for the data from the Amundsen and Bellingshausen Seas. Figure I.10b shows the result of a scale transformation with the factor *R* for a single profile of the second Ross cruise from Julian day 230. It shows a good agreement between the measured and transformed keel indicating that this particular floe was close to isostatic balance.

I.5.2 Correlations of thicknesses on different scales

In order to further investigate the correlations between the different snow and ice thickness variables, these values were calculated on different spatial scales. In order to access different spatial scales the thickness profile f_j was averaged using gaussian filters of the form

$$G_{ij} = \frac{1}{\sqrt{2\pi\tilde{n}}} \exp\left(\frac{(i-j)^2}{2\tilde{n}^2}\right),$$

where $\tilde{n} = \rho/\Delta x$ defines the Gaussian width ρ in terms of the spacing $\Delta x = 1m$. A spatially averaged profile $\tilde{f}_i$, over the width $\tilde{n} = \rho/\Delta x$, is thus obtained from the original profile surface f_j by

$$\tilde{f}_i = \sum_j G_{ij} f_j \ .$$

It thus was consecutively averaged over widths of 1 m, 2 m, 5 m and over the total profile length (about 100m).

As a general outcome of this correlation analysis three major coefficients of significant correlations ($|r|>0.5$) could be identified on every scale. The first coefficient was a high correlation ($|r|>0.9$) between ice and keel thickness or between snow and sail thicknesses, which is a consequence of the freeboard generally being an order of magnitude smaller than the other thickness variables. The second coefficient usually was a significant positive correlation between sail and keel thickness and the third mode was a negative correlation between the ratio of snow/ice thickness and the freeboard. The last two correlations closely reflect how well the data demonstrate isostatic equilibrium on the particular spatial scale on which the correlation was investigated.

The changes of the correlation coefficients observed when going from local, unaveraged data to averages calculated over spatial scales of width 2 m, 5 m, and the total length of the profiles are presented in Table I.3. It can be seen that even if correlations are

initially insignificant on the local scale, they usually become significant on the 2 m level and the significance level typically increases as the averaging scale increases. Although not shown, it should be noted, that anticorrelations between the snow/ice thickness ratio and freeboard improve with higher averaging scale whereas anticorrelations between just snow and freeboard remain low (mostly << 0.3). This indicates that in accordance with the isostatic relationship it is *not* snow load in itself that determines flooding but rather the ratio of snow to ice thickness.

In order to further illustrate the behavior of the second correlation coefficient in Table I.3 and hence the relation of isostacy to flooding, freeboard is graphed versus the snow/ice thickness ratio for all measurements of the two 1995 late winter cruises in the Ross and Amundsen/Bellingshausen Seas in Figure I.11a and d. In analogy with the work of *Massom et al.*[1996] in the Weddell Sea, these graphs can be used to examine the extent to which flooding is connected with isostatic imbalance and hence ice stresses, and how this connection depends on the scale of observation. The same sets of data which are presented without averaging in Figure I.11a and d are shown on scales of 2 m and 5 m in Figure I.11b, e and c, f respectively.

The flooding criterion, derived from the isostatic balance equation [*Ackley et al.*,1990; *Eicken et al.*,1994],

$$\frac{h_s}{h_i} \geq \frac{\rho_w - \rho_i}{\rho_s}, \qquad (5)$$

with ρ_w being the density of seawater (about 1.03 g cm^{-3}) and ρ_i the density of sea ice (approximately 0.91 g cm^{-3}), is used to investigate this question. As can be seen, for a certain ratio of snow to ice thickness, the occurrence of negative freeboard is mainly dependent on snow density (ρ_s). The arrows in Figure I.11 indicate the snow/ice thickness ratio that equals the righthand side of equation (5) with the mean value of snow density measured for the each corresponding cruise. The maximum possible spread around this mean snow density is indicated by dashed straight lines at snow/ice thickness values 0.6

(corresponding to a density of new snow of about 0.20 g cm^{-3}) and 0.17 (corresponding to an assumed density of slush of about 0.70 g cm^{-3}). The two hatched areas mark possible imbalances where the freeboard is dominated by stresses in the ice (possibly associated with ridging or rafting) rather than by isostatic load. In the first area A_1 snow densities higher than 0.70 g cm^{-3} would be required in order to induce flooding. In the second area A_2 the snow density had to be smaller than 0.20 g cm^{-3} in order to not induce flooding.

As can be seen in Figure I.11a and d, the number of points that are isostatically imbalanced on a local, unaveraged scale is small but not negligible. Surprisingly, there are almost no points in the imbalance area A_1 in the Amundsen and Bellingshausen Seas (Figure I.11d); and also the number of measurements with negative freeboard to the left of the mean snow density (arrow) is small.

Investigating the situation on larger spatial scales (2 m and 5 m) Figure I.11b shows that area A_1 is depleted of data points on a scale of 2 m for the Ross Sea. It further can be seen that A_1 does not contain points anymore on a scale of 1m for the Amundsen and Bellingshausen Seas (Figure I.11e). On a scale of 5 m it can be seen (Figure I.11c and f) that A_2 is also devoid of data points and all points have almost completely contracted in the stable area outside of A_1 and A_2. It therefore follows that although isostatic imbalance does occur locally it quickly disappears when spatial averaging of only a few meters is applied.

Viewing the results shown in Figure I.11 it can be seen that negative freeboards initiated by ice stresses are rare even on the local scale. Interestingly there are few points in the imbalance areas of the Amundsen and Bellingshausen Seas (Figure I.11d). On the other hand the Amundsen and Bellingshausen Seas are shown to be regions of prevalent ridging (Table I.1b, section 3.2.2). Therefore it can be concluded that not every ridging or rafting event automatically leads to a situation of isostatic imbalance. It was further seen in Figure I.11 that local imbalance areas can disappear quickly on an averaging scale of 1 to 5 meters. Hence it can be concluded that deformation does not change the isostatic balance on a scale of 1 to 5 meters and in many cases not even on a local scale.

I.6 Spatial and seasonal differences revealed by examination of isostatic balance

I.6.1 Formulation of a more generalized isostatic equation and its validity for the different geographical areas

The correlation analysis in chapter 4.2 has shown correlations between different snow and ice thickness variables. However for a proper investigation of isostatic balance the densities of snow, ice, and seawater have to be involved. Since negative freeboards (Table I.1b) and hence flooded snow was observed quite frequently at drilling locations, a more detailed isostatic equation will be developed that includes the density of slush (flooded snow). From this a density weighted, "generalized" snow to ice thickness ratio will be derived which more accurately describes the problem of isostatic balance. Depending whether freeboard is positive or not one obtains for the isostatic equation

$$\rho_s h_s + \rho_i h_i = (h_i - h_{fb})\rho_w \qquad \text{for} \quad h_{fb} \geq 0 \qquad (6a)$$

$$\rho_s (h_s + h_{fb}) + \rho_i h_i - \rho_{sl} h_{fb} = (h_i - h_{fb})\rho_w \qquad \text{for} \quad h_{fb} \leq 0, \qquad (6b)$$

with freeboard h_{fb} and slush density ρ_{sl}. It should be noted that the snow thickness h_s includes h_{fb} for the case of negative freeboard that is given in equation (6b). The *generalized ratio of density weighted snow/ice thickness* (GSI) for the two cases in equation (6) shall be defined as

$$Gen\left\{\frac{h_s}{h_i}\right\} = \frac{\rho_s h_s}{\rho_i h_i} \qquad \text{for} \quad h_{fb} \geq 0 \qquad (7a)$$

$$Gen\left\{\frac{h_s}{h_i}\right\} = \frac{\rho_s (h_s + h_{fb}) - \rho_{sl} h_{fb}}{\rho_i h_i} \qquad \text{for} \quad h_{fb} \leq 0. \qquad (7b)$$

Eliminating the snow and slush densities with equation (6), this GSI gives for both cases a straight line with the freeboard/ice thickness ratio as variable,

$$Gen\left\{\frac{h_s}{h_i}\right\} = \left(\frac{\rho_w}{\rho_i} - 1\right) - \left(\frac{\rho_w}{\rho_i}\right)\left(\frac{h_{fb}}{h_i}\right). \quad (8)$$

Assuming constant values for ρ_i and ρ_w (0.91 and 1.03 g cm^{-3} respectively) isostatic balance or imbalance of a floe can be investigated by how much individual points in equations (7), with given snow and slush densities, deviate from the isostatic line given in equation (8).

Figure I.12a shows the GSI plotted versus the freeboard/ice thickness ratio for all measured drilling points of the early winter Ross Sea cruise (NBP95-3). At each drilling location h_s, h_i and h_{fb} were measured and used to compute the GSI values. For ρ_s the mean bulk snow density was used for the corresponding cruise. Due to difficulties in measuring ρ_{sl} a value of 0.70 g cm^{-3} was assumed. The dotted line in Figure I.12a is a least squares regression line for the data points. It can be compared to the isostatic line (equation (8)) in Figure I.12a (solid line). Similarly to Figure I.11, deviations of single points from the regression line can be caused by local deviations from the assumed mean density values (ρ_s, ρ_i and ρ_{sl} in the case of Figure I.12a). However, as compared to the local scale graphs in Figure I.11, the overall scatter seems to be less in the data of Figure I.12a. The regression line in Figure I.12a fits the data with a correlation of 0.8 and therefore it can be assumed that the regression line is a good representation for the data in comparison the isostatic line. The difference between these two straight lines will hence be used as a measure of how well the isostatic equation is satisfied by the data. Figure I.12b shows the data of Figure I.12a averaged on a 5 m scale. It can be seen that the correlation between the points has increased to 0.9 and there is less scatter. At the same time the regression line has approached the isostatic line.

In Figure I.13 the correlation coefficients between GSI and the freeboard to ice thickness values are listed for each cruise for the local scale as well as for the scale of the complete profiles. In general it can be seen that the use of the GSI provides significantly higher correlations as compared to the corresponding values in Table I.3 where the

simpler snow/ice thickness ratio was used. In addition the correlation coefficients become higher with increased spatial averaging. Figure I.13 and Table I.3 both show that correlations are clearly higher for the early winter cruise (NBP95-3) than for all other late winter cruises. This could be explained by the fact that in early winter sea ice is younger and hence should have less time to accumulate a history of ice motion and deformation events which commonly lead to isostatic imbalances.

Finally, it can stated that by defining a GSI which included densities it was possible to more accurately describe isostatic balance. Even on a local level measured points were generally found to be close to being in isostatic balance. Further, with increasing spatial averaging a decreasing scatter of the data was observed, indicating that imbalance is a function of scale. Single points that deviate from the line of isostatic balance can be caused by either measuring inaccuracies (mainly in the densities) or by stress-induced local depression or rise of the ice floe. The depressions were found dry prior to drilling but showed a negative freeboard due to up-welling seawater as the result of drilling (section 3.4).

I.6.2 Influence of snow and slush density on isostatic balance or imbalance

The analysis in section 4.1 raises the question of how far the choice of the two free density parameter ρ_s and ρ_{si} can influence the correlations and the agreement between the regression line and the isostatic line. The use of a mean bulk snow density for each cruise in column 1 of Figure I.13 was superior to using the one or two snow pits available per floe to define separate snow densities for individual floes. From this it is obvious that snow pits on individual floes usually do not provide representative snow densities for these floes. Since the choice of a constant snow density for all floes (zero variance) gives higher correlations, it can also be concluded that the variance of the measured densities between floes exaggerates the variance of the true mean densities per floe. More unknowns are

involved in the proper choice of a slush density. There is no satisfactory procedure known yet for accurately measuring the density of slush. Since water is invariably lost during the measurement procedure it is assumed that even the highest measured values (about 0.70 g cm^{-3}) represent a lower limit of real slush densities.

In the following an upper bound for the slush density shall be determined from a theoretical standpoint. If snow is viewed as ice particles surrounded by interstitial pockets of air where the density of the latter can be neglected against those of ice and water one finds ρ_s/ρ_i for the volume fraction occupied by ice particles and $(1-\rho_s/\rho_i)$ for the volume fraction of air. If all air pockets of this 'snow sponge' are filled with water one obtain the maximum possible slush density

$$\rho_{sl/max} = \rho_w - \left(\frac{\rho_w}{\rho_i} - 1\right)\rho_s. \qquad (9)$$

If ρ_w and ρ_i are taken as constants, the value of maximum slush density only depends on the snow density.

Real slush can be assumed to have a density that is smaller than or equal to this maximum density and will depend on the detailed process of slush formation. During the process of flooding not all air pockets necessarily fill with water and parts of the upper snow pack may fall into the flooded layer leading to an increase in the ice volume to water volume ratio. Both effects decrease the slush density with respect to equation (9). For NBP 95-3 with a mean bulk snow density of 0.34 g cm^{-3}, equation (9) gives a maximum slush density of 0.96 g cm^{-3}. Using this value instead of 0.70 g cm^{-3} in Figure I.12b on the 5 m scale leads to Figure I.12c. One sees that the correlation between the GSI and h_f/h_i has increased and that the agreement between the regression line and the isostatic line has improved. On larger averaging scales (scale of profiles) it can be seen in Figure I.12d that the variance of the data around the line of regression is even more reduced.

Also for data sets of the other cruises it was generally found that a fit of equation (8) to the data was improved by using slush densities higher than the assumed value of 0.70 g

cm^{-3}. On the other hand it can be seen that correlation coefficients (Figure I.12 and Figure I.13) between the GSI and h_f/h_i are only marginally increased by using the maximum slush density.

I.6.3 Investigations of single profiles

Examination of data points measured on single profiles further clarifies how the values for slush and snow densities influence the fit of the data to the isostatic line. Only profiles that cover a sufficient freeboard range are suitable for such an examination.

Figure I.13 shows three 1995 examples of such profiles, two from the early winter Ross Sea (Figure I.13a) and one from the late winter Amundsen and Bellingshausen Seas (Figure I.13e, i). The graphs to the right of the profiles show the GSI versus freeboard/ice thickness ratio for all data (without spatial averaging) using the mean bulk snow density of the particular cruise and 0.70 g cm^{-3} for the slush density (Figure I.13b, f and j). As a next step the slush density was varied to fit the line of regression better to the isostatic line (Figure I.13c, g and k). Finally the snow density was adjusted in order to improve the fit (Figure I.13d, h and l).

Figure I.13b shows the data points of the ridged profile (Figure I.13a) using the mean bulk snow density and 0.70 g cm^{-3} for the slush density. Changing the slush density to its maximum value (0.96 g cm^{-3}) the regression line (solid line) agrees distinctly better with the isostatic line (dotted line, Figure I.13b). Subsequent adjustment of the snow density (from 0.34 to 0.37 g cm^{-3}) results in an even more improved fit (Figure I.13d).

Figure I.13e shows another profile of the same cruise which is only half as long as the profile in Figure I.13a but which offers a well distributed large freeboard range. Variation of the slush density from 0.70 g cm^{-3} to 0.80 g cm^{-3} gives Figure I.13g resulting in a rotation of the regression line until it is almost parallel to the isostatic line. Variation of the snow density from 0.34 g cm^{-3} to 0.39 g cm^{-3} again gives an almost perfect fit and

in this case reproduces exactly the measured value for the snow density of that particular floe.

Figure I.13i shows a typical rough profile close to the ice edge in the late winter Amundsen Sea, displaying the underlying pancake structure of its origin. Figure I.13j displays its GSI versus freeboard/ice thickness ratio on a local scale. But since there are very few data points in the x-axis range -0.3 and 0.1 it is advisable in this case to diminish the range by averaging. On a 5 m averaging scale the correlation between the data points has visibly increased and, by enlarging the slush density to 0.80 g cm^{-3}, the line of regression has become parallel to the isostatic line (Figure I.13k). Reduction of the snow density from the mean value 0.37 g cm^{-3} to 0.33 g cm^{-3} gives a perfect agreement between both lines. In this last example the adjustment procedure leads to a smaller than average snow density even if the measured mean snow density on this floe was higher (0.40 g cm^{-3}). This suggests that this particular snow pit was not representative for this floe.

The results of Figure I.13 illustrate that adjustment of the density parameters of individual profiles generally results in an improved fit between the regression line of the data and the isostatic line. This method of adjusting the two density parameters can therefore be proposed for floes where the snow pit values do not seem to be representative. However, in order to confirm that the adjusted densities are generally improved estimates of the real values, a finely sampled density profile parallel to the drill profile needed to be measured.

In summary the method of density adjustment almost always leads to higher than assumed slush densities (0.7 g cm^{-3}) and provides a good way to find a value for the mean snow density of a floe. It was further observed that the slope of the regression line is most sensitive to variations in slush density, while parallel displacement of the regression line seems to be sensitive only to variations in the snow density. This could be verified by examining the theoretical expressions for the two parameters of the linear least squares fit.

I.7 Isostatic depression and uplift of a floe

The previous section showed that most floes are close to being isostatically balanced if an averaging scale of a few meters is used. These results suggest that the isostatic uplift and subsidence of a floe may be estimated by idealizing it as being level with a constant snow and ice thickness equal to the mean values of the floe. The following simplified scenarios of snow loading, ice growth and bottom melting can be applied to this idealized floe (section 6.1). As a further consequence they can be applied to estimating snow ice growth (section 6.2).

I.7.1 Snowload, bottom melting and ice growth

First subsidence due to increasing snow load will be considered. This process becomes crucial when the upper surface of the floe sinks below the waterline (i.e. the freeboard becomes zero). At this point the snow layer will start to flood, a process which adds further weight to the snow and ice column leading to more depression and more flooding. The incremental subsidence of the floe therefore seems to be a never ending process.

In the following it will be assumed that below the waterline all the snow is flooded and that all its air pores actually become water-logged. If it is further assumed the snow density at the ice interface to be equal to the snow layer on top ($=\rho_s$), a new snow fall Δx_s will depress the floe by $\Delta x_s\rho_s/\rho_w$ of which, in turn, $(1-\rho_s/\rho_i)$ parts will be filled with water at the bottom of the floe. The infinite summation of the subsidence increments results in the following geometric series

$$\Delta y_s = \Delta x_s \frac{\rho_s}{\rho_w}\left[1+\left(1-\frac{\rho_s}{\rho_i}\right)+\left(1-\frac{\rho_s}{\rho_i}\right)^2+\ldots\right]=\frac{\rho_i}{\rho_w}\Delta x_s \qquad (10)$$

for the value of the depression Δy_s of an isostatically balanced floe with freeboard zero in response to an additional snowload of Δx_s. It also shows that the floe will find a finite and

stable equilibrium even if the underlying processes are complicated. This new state of the floe is again isostatically balanced; the same result (equation(10)) can be found by assuming the isostatic equation (6) for zero freeboard initially and solving the isostatic equation for negative freeboard $(-\Delta y_f)$ with an snowload increased by Δx_s.

In a similar fashion bottom melting creates isostatic subsidence. Melting the ice underneath by Δx_m will make the floe sink by an amount Δy_m which can be derived as

$$\Delta y_m = \frac{1}{\rho_{sb}} \frac{\rho_i(\rho_w - \rho_i)}{\rho_w} \Delta x_m , \tag{11}$$

by solving the isostatic equation (6).

Finally, if one considers how the growth of congelation ice counteracts the above two processes of subsidence (equations (10) and (11)) by isostatically uplifting the floe one obtains

$$\Delta y_g = -\frac{\rho_i}{\rho_w} \Delta x_g \tag{12}$$

for the uplift in response to an ice growth of Δx_g. Positive y values here refer to subsidence and negative y values to uplift.

Given these formulas an order of magnitude comparison between these different processes and their significance can be carried out. Table I.5 provides equations (10), (11) and (12) again, with the numeric values for ρ_w and ρ_i (1.03 and 0.91 g cm^{-3} respectively), and ratios between them. It is assumed now a typical average snowfall rate of 0.01 cm d^{-1} for the months between February and November in Antarctic coastal regions [*Parkinson*, 1982; *Bromwich*, 1990]. Further in Antarctic areas where bottom melting occurs mean melt rates are suggested to be about 0.4 cm d^{-1} [*Lange et al.*, 1990]. Using these values together with a typical snow density ρ_s of about 0.3 g cm^{-3} to compute the ratio of $\Delta y_s/\Delta y_g$ (Table I.5) the effect of depression due to snowfall as compared to bottom melting is 6:100. The effect of bottom melting thus could be 1 to 2 orders of magnitude higher than the effect of snow load. However, for bottom melting to occur at this magnitude ice

surface temperatures should not fall below -5°C and oceanic heat fluxes should be at least as high as 20-30 W m^{-2} as shown by *Lange et al.*[1990]. Recent studies [*Lytle and Ackley*, 1996] in the western Weddell Sea however have shown that actual oceanic heatfluxes there range between 4-12 W m^{-2}. This indicates that bottom melting presumably plays a minor role in Antarctica. This conclusion is further supported by *Lytle and Ackley* [1996] who also found that flooding and snow ice formation, both widespread phenomena in Antarctica, further reduce the magnitude of bottom melting.

Finally, if one applies a growth rate of 0.4 cm d^{-1} [*Wadhams et al.*, 1987] for Antarctic sea ice and compares the ratio of the depression due to snowfall to the counteracting effect due to ice growth (Table I.5) a ratio of 1:40 results.

I.7.2 Estimation of snow ice growth

A simple *gedankenexperiment* can be carried out to determine the snow ice growth between the early and late winter Ross Sea cruises from mean thickness values for snow, ice and freeboard spaced three months apart (see Table I.1b). As a first step a layer of snow which accounts for the snow ice formation Δx_{si} between the two cruises needs to be added to the difference in measured snow thickness Δx_s. As a second step the layer of snow which did not contribute to flooding and snow ice formation has to be subtracted. The effective snow layer Δx_s^{eff} which is significant for flooding and snow ice formation thus can be calculated as

$$\Delta x_s^{eff} = \left[\Delta x_s + \Delta x_{si}\frac{\rho_i}{\rho_w}\right]_1 - \left[\left(fb_1 + |\Delta y_g(\Delta x_g)|\right)\frac{\rho_i}{\rho_s}\right]_2 , \qquad (13)$$

with fb_1 the positive mean freeboard of the first Ross Sea cruise and $\Delta y_g(\Delta x_g)$ the uplift due to congelation ice growth Δx_g according to equation (12). It can be seen that the first expression in equation (13) is the sum of the actually measured difference in snow thickness plus the additional layer of snow which would have been measured if it had not been transformed to snow ice. The second expression describes the part of the snow fall

which did not contribute to flooding and snow ice formation. The difference between both expressions is thus the effective snow layer Δx_s^{eff} which induces flooding and/or snow ice formation. The total measured ice growth Δx_i further is given by

$$\Delta x_i = \Delta x_g + \Delta x_{si} ,$$

the sum of congelation ice growth and snow ice growth. The depression Δy_s due to the effective snow layer Δx_s^{eff} is, according to equation (10)

$$\Delta y_s\left(\Delta x_s^{eff}\right) = \Delta x_{si}\frac{\rho_i}{\rho_w} - fb_2 ,$$

with fb_2 being the mean, negative freeboard value of the second, late winter Ross Sea cruise. Assuming again ($\rho_{sb}=\rho_{st}=\rho_s$) the final equation for determining the snow ice growth Δx_{si} therefore becomes

$$\Delta x_{si} = \frac{\left(\Delta x_s - \frac{\rho_i}{\rho_s} fb_1 - \frac{\rho_i^2}{\rho_s\rho_w}\Delta x_i + \frac{\rho_w}{\rho_i} fb_2\right)}{\left(1 - \frac{\rho_i}{\rho_w} - \frac{\rho_i^2}{\rho_s\rho_w}\right)} . \qquad (14)$$

Inserting Δx_s = 11 cm for the mean snow accumulation, Δx_i =12 cm for the mean ice growth between the two Ross Sea cruises, fb_1 = 1.4 cm and fb_2 = -0.3 cm for the corresponding freeboard values and ρ_s = 0.37 g cm^{-3} for the mean snow density gives 9.1 cm of mean snow ice growth compared to 2.9 cm of congelation ice growth in the course of three months. It can be concluded that under simplified, isostatically balanced conditions, which exclude any deformation processes, snow ice formation would be the major contribution to the overall ice growth.

I.8 Conclusions

A comparative analysis of five snow and ice thickness data sets which were acquired during four voyages within two years in the South Polar Pacific Ocean has been

completed. Annual and seasonal contrasts are discussed as is the spatial variability on several different scales. The following conclusions were reached.

Two different methods for the acquisition of snow and ice thickness data were discussed and their mutual representativeness and applicability was shown in their area of overlap. Level ice thicknesses for all observed areas including the early winter Ross Sea were similar or higher than corresponding values for other Antarctic regions in late winter. Negative freeboards were observed at least as frequently in the Amundsen and Bellingshausen Seas and much more frequently in the Ross Sea as compared with the Weddell Sea.

The Amundsen and Bellingshausen Seas could be characterized as regions of persistent deformation, whereas the pack ice in the atmospherically calmer and more protected Ross Sea embayment is less dominated by ridging and rafting. As a result distribution functions for the ice of the Amundsen and Bellingshausen Seas are more irregularly shaped and show a broader range of ice thicknesses. As a further consequence, the scale transformation of the sail distribution to match the measured keel distribution worked somewhat better for the less disturbed Ross Sea region than for the Amundsen and Bellingshausen Seas.

A thorough investigation of the drilling area prior to drilling revealed to what extent moisture, wetness and flooding of an undisturbed floe are related to subsequent negative freeboard measurements. There was a good correlation with negative freeboard at places where flooding had occurred and a lesser correlation where the snow was only moist. The latter finding is likely caused by effects of capillary suction. Many locations were also found which were dry but had an ice surface at or below the water level after drilling. Human impact or low permeability of the ice can both result in this observation. Furthermore, moisture, wetness and flooding are well correlated to the ratio of snowload to ice thickness. However, the relation to the amount of ridging is less conclusive.

Correlations between snowload, ice thickness and freeboard were examined. Isostatic balance was investigated in detail on various spatial scales with help of a formulation of an isostatic balance equation which included slush density. Deviations from isostatic equilibrium occurred locally but decreased drastically on a spatial averaging scale of only a few meters, even for heavily ridged areas. Exact fits of the data to isostatic equilibrium showed a sensitive dependence on the proper choice of snow and slush density. In this context an estimation of a maximum possible value for the slush density proved to be useful. Sea ice seemed to be closer to isostatic balance in early winter when it is still young as contrasted to later in the season.

With help of a simple isostatic model the effect of increasing snowload, bottom melting and ice growth on the depression and uplift of a floe could be calculated. This also gave a tool for making rough estimates of how much snow ice growth contributes to the total ice growth.

To find classifying qualities for sea ice from different geographical regions and possibly to find characteristics which will extend beyond spatial borders, it will be necessary to find a group classification for the different sampled floes of first year ice. Mean thickness of snow and ice alone will not be sufficient input for such a classification, as the spatial variabilities of these variables along a profile line are also important classifiers. This question of classification will be considered in a following study where roughness characteristics of the different snow and ice surfaces will be examined.

I.9 References

Ackley, S.F. and T.E. Keliher, Antarctic sea ice dynamics and its possible climatic effects, *AIDJEX Bull., 33*, 53-56, 1976.

Ackley, S.F., A review of sea-ice weather relationships in the Southern Hemisphere, in *Sea Level, Ice, Climate Change, 131*, 127-159, 1981.

Ackley , S.F., M.A. Lange and P.Wadhams, Snow cover effects on Antarctic sea ice thickness, in Sea Ice Properties and Processes, edited by S.F. Ackley and W.F.Weeks, *CRREL Monograph 90-1*, pp. 16-21, U.S. Army Corps of Engineers, Hanover, NH, 1990.

Ackley, S.F. and C.W. Sullivan, Physical controls on the development and characteristics of Antarctic sea ice biological communities - a review and sythesis, *Deep-Sea Research 1, 41*, 1583-1604, 1994.

Allison, I., The East Antarctic sea ice zone: ice characteristics and drift, *GeoJournal, 18.1*, 103-115, 1989.

Allison, I., R.E. Brandt and S.G. Warren, East Antarctic sea ice: albedo, thickness distribution and snow cover, *J. Geophys. Res., 98*(C7), 12,417-12,429,1993.

Allison, I. and A.P. Worby, 1994, Seasonal changes of sea-ice characteristics off East Antarctica, *Ann. Glaciol., 20*, 195-201.

Bromwich, D.H., Snowfall in high Southern latitudes, *Rev.Geophys., 26*(1), 149-168, 1988.

Bromwich, D.H., Estimates of Antarctic precipitation, *Nature, 343*, 627-628, 1990.

Budd, W.F., Antarctic sea ice variations from satellite sensing in relation to climate, *J. Glaciol., 15*, 417-427, 1975.

Carleton, A.M., Monthly variability of satellite-derived cyclonic activity for the SouthernHemisphere winter, *J. Climatol., 1*, 21-38, 1981.

Cavalieri, D.J. and C.L. Parkinson, Large-scale variations in observed Antarctic sea ice extent and associated atmospheric circulation, *Monthly Weather Review, 109*, 2323-2336, 1981.

Comiso, J.C., P.Wadhams, W.B.Krabill,R.N.Swift, J.P.Crawford and W.B.Tucker III, Top/Bottom multisensor remote sensing of Arctic sea ice, *J.Geophys.Res., 96*(C2), 2693-2709, 1991.

Eicken, H., M.A. Lange, H.W. Hubberten and P.Wadhams, Characteristics and distribution patterns of snow and meteoric ice in the Weddell Sea and their contribution to the mass balance of sea ice, *Ann. Geophys., 12*, 80-93, 1994.

Eicken, H., H. Fischer and P. Lemke, Effects of the snow cover on Antarctic sea ice and potential modulation of its response to climatic change, *Ann. Glaciol., 21*, 369-376, 1995a.

Eicken, H., M.Lensu, M.Leppaeranta, W.B.Tucker, A.J.Gow and O.Salmela, Thickness, structure, and properties of level summer multiyear ice in the Eurasian sector of the Arctic ocean, *J.Geophys.Res.*,*100*(C11), 22,697-22,710, 1995b.

Dierking, W., Laser profiling of the ice surface topography during the Winter Weddell Gyre Study 1992, *J.Geophys.Res.*,*100*(C3), 4,807-4,820, 1995.

Drinkwater, M.R., D.G.Long and D,S. Early, Enhanced resolution scatterometer imaging of Southern Ocean sea ice, *ESA Journal*, *17*, 307-322, 1993.

Fletcher, J.O., Ice extent on the southern ocean and its relation to world climate, *Rand Corp. Memo.* RM-5793-NSF, 1969.

Fritsen, C.H., V.I. Lytle, S.F. Ackley and C.W. Sullivan, Autumn bloom of Antarctic pack-ice algae, *Science*, *266*, 782-784, 1994.

Gordon, A.L. and H.W. Taylor, Seasonal change of Antarctic sea ice cover, *Science*, *87*, 346-347, 1975.

Gordon, A.L., Seasonality of Southern Ocean Sea Ice, *J.Geophys.Res.*, *86*(C5), 4193-4197,1981.

Hibler, W.D., III, and S.F. Ackley, Numerical simulations of the Weddell Sea pack ice, J. *Geophys. Res.*, *88*(C5), 2873-2888, 1983.

Hosseinsmostafa, A.R., V.I. Lytle, K.C.Jezek, S.P. Gogineni, S.F. Ackley and R.K.Moore, Comparison of radar backscatter from Antarctic and Arctic sea ice, *J. Electromagn. Waves and Applications*, *9*(3), 421-438, 1995.

Jacobs, S.S. and J.C. Comiso, Sea ice and oceanic processes on the Ross Sea continental shelf, *J.Geophys.Res.*, *94*(C12), 18,195-18,261, 1989.

Jeffries, M.O. and U. Adolphs, Early winter ice and snow thickness distribution, ice structure and development of the western Ross Sea pack ice between the ice edge and the Ross ice shelf, *Antarc.Sci.*, *9*(2), 1997, in print.

Jeffries, M.O., K.Morris, A.P. Worby and W.F. Weeks, Late winter sea ice properties and growth processes in the Bellingshausen and Amundsen Seas, *Ant. J. U.S.*, 29, 11-13, 1994.

Jeffries, M.O., R. Jana, S. Li and S. McCullars, Sea ice and snow thickness distributions in late winter 1993 and 1994 in the Ross, Amundsen and Bellingshausen Seas, *Ant. J. U.S.*, 30, 1995.

Lange, M.A., P. Schlosser, S.F. Ackley, P. Wadhams and G.S. Dieckmann, ^{18}O concentrations in sea ice of the Weddell Sea, Antarctica, *J. Glaciol.*, *36*(124), 315-23, 1990.

Lange, M.A. and H.Eicken, The sea ice thickness distribution in the Northwestern Weddell Sea, *J. Geophys.Res.*, *96*(C3), 4821-4837, 1991.

Ledley, T.S., Snow on sea ice: competing effects in shaping climate, *J. Geophys. Res.*, *96*(D9),17,195-17,208, 1991.

Ledley, T.S., Sea ice: a factor in influencing climate on short and long time scales, in *Ice in the Climate System*, edited by W. Peltier, pp 532-556, Springer-Verlag, New York,1994.

Lytle, V.I. and S.F. Ackley, Heat flux through sea ice in the western Weddell Sea: convectice and conductive transfer processes, *J.Geophys.Res.*, *101*(C4), 8853-8868, 1996.

Martinson, D., Ocean heat and sea ice thickness in the Southern Ocean, in *Ice in the Climate System*, edited by W. Peltier, pp 597-610, Springer-Verlag, New York, 1994. Massom, R.A., M.R. Drinkwater and C. Haas, Winter snowcover sea ice in the Weddell Sea, *J.Geophys.Res*, accepted, 1996.

Parkinson, C., Sensitivity studies on a model of the Weddell ice pack, *Ant. J. U.S.*, *17*(5), 94-95, 1982.

Parmerter, R.R., A mechanical model of rafting, *AIDJEX Bulletin*, 23, 97-115, 1974.

Streten, N.A. and D.J. Pike, Characteristics of the broadscale Antarctic sea ice extent and the associated atmospheric circulation 1972-1977, *Arch. Meteor. Geophys. Bioklim.*, *A29*, 279-299, 1980.

Sturm, M., K. Morris and R. Massom, The character and distribution of the winter snow cover on the sea ice of the Bellingshausen, Amundsen and Ross Seas, Antarctica, 1994-1995, submitted.

Sturman, A.P. and M.R. Anderson, On the sea-ice regime of the Ross Sea, Antarctica, *J. Glaciol.*, *32*, 54-59, 1986.

Turcotte, D.L. and G. Schubert, Geodynamics, 450p, 1982.

Wadhams, P. and R.J. Horne, An analysis of ice profiles obtained by submarine sonar in the Beaufort Sea, *J.Glaciol.*, *25*(93), 1980

Wadhams, P., W.B. Tucker III, W.B. Krabill, R.N. Swift, J.C. Comiso and N.R. Davis, Relationship between sea ice freeboard and draft in the Arctic basin, and implications for ice thickness monitoring, *J.Geophys.Res.*, *97*(C12), 20,325-20,334, 1992.

Wadhams, P., M.A. Lange and S.F. Ackley, The ice thickness distribution across the Atlantic sector of the Antarctic Ocean in midwinter, *J.Geophys.Res.*, *92*(C13), 14,535 -14,552, 1987.

Wadhams, P., Sea ice thickness changes and their relation to climate, in *The Polar oceans and their role in shaping the global environment*, Geophysical Monograph 85, pp. 337-361, 1994.

Weeks, W.F., W.B. Tucker III, M. Frank and S. Fungcharoen, Characterization of Surface Roughness and Floe Geometry of Sea Ice over the Continental Shelves of the Beaufort and Chukchi Seas, in Sea Ice Processes and Models, edited by R.S. Pritchard, 1980.

Worby, A.P., W.F. Weeks, M.O. Jeffries, K. Morris and R. Jana, Late winter sea ice and snow thickness distribution in the Bellingshausen and Amundsen Seas, *Ant. J. U.S.*, 29, 13-15, 1994.

Worby, A.P., M.O. Jeffries, W.F. Weeks, K. Morris and R. Jana, The thickness distribution of sea ice and snow cover during late winter in the Bellingshausen and Amundsen Seas, Antarctica, *J. Geophys. Res.*, *101*(C12), 28,441-28,455, 1996.

I.10 Figures

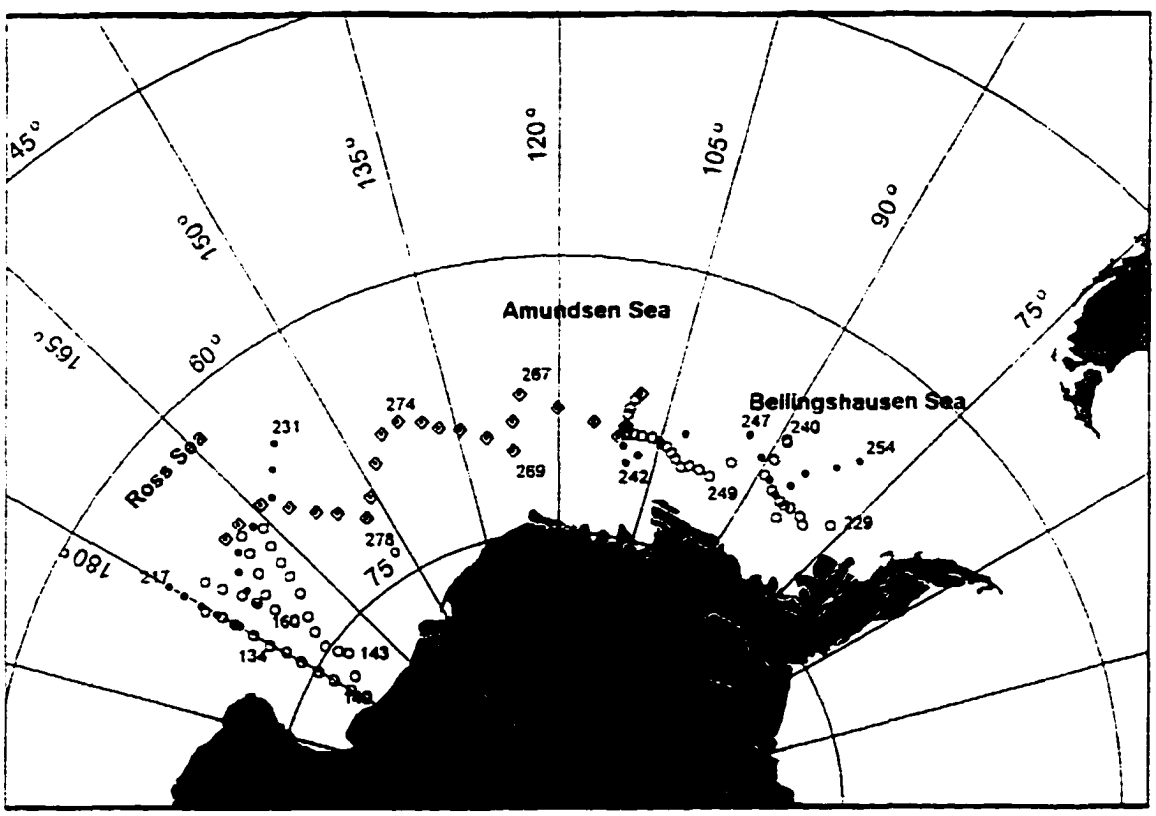

Figure I.1: Ice stations along five track lines which were followed by the Nathaniel B. Palmer (NBP) between August 1993 and September 1995. NBP 95-3 (open circles) covered the Ross Sea in early winter; NBP 95-5/1 (filled circles) covered the Ross Sea in late winter. NBP 93 (open circles) went in the Amundsen/Bellingshausen Seas in late winter 1993; NBP 95-5/2 (filled circles) revisited the same area in 1995. NBP 94 (dotted diamonds) spanned the area of the Amundsen Sea to the North Western Ross Sea.

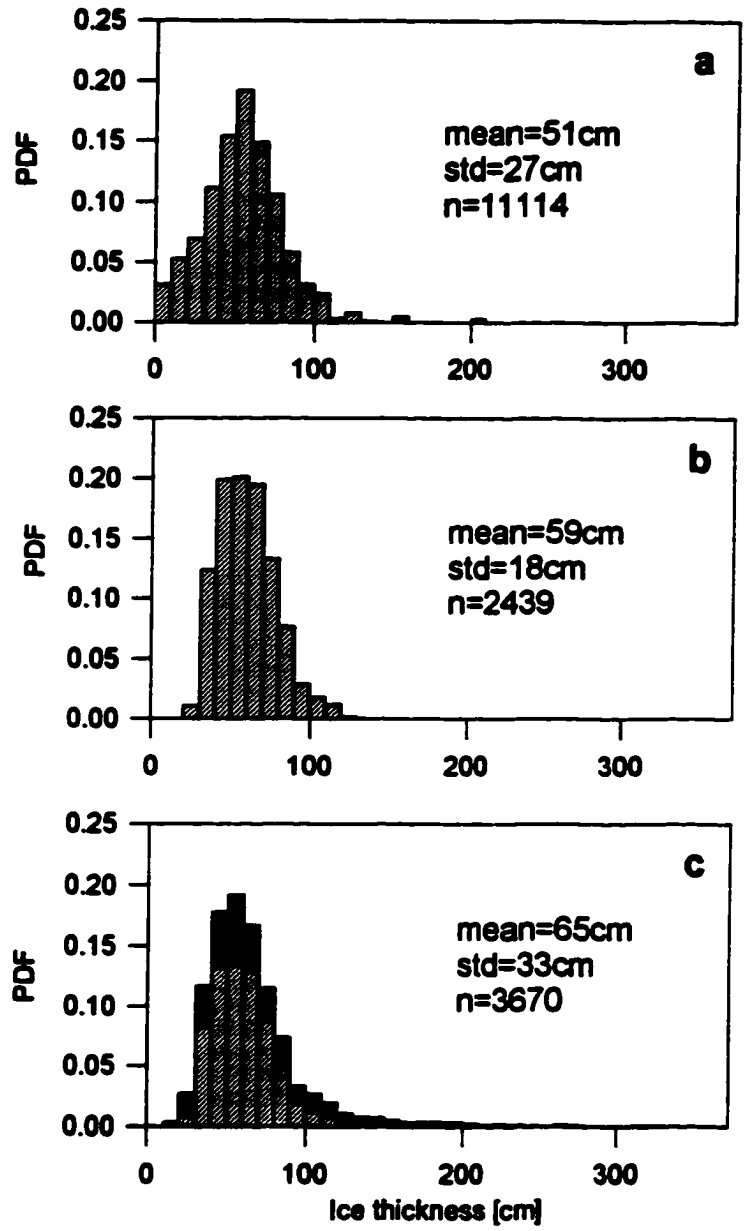

Figure I.2: Probability Density Functions (PDF) of (a) Set B data, of (b) Set A level ice and (c) for all drilling data of NBP 95-3. Shaded areas in (c) indicate the relative distribution of ridging, which contributed 34%.

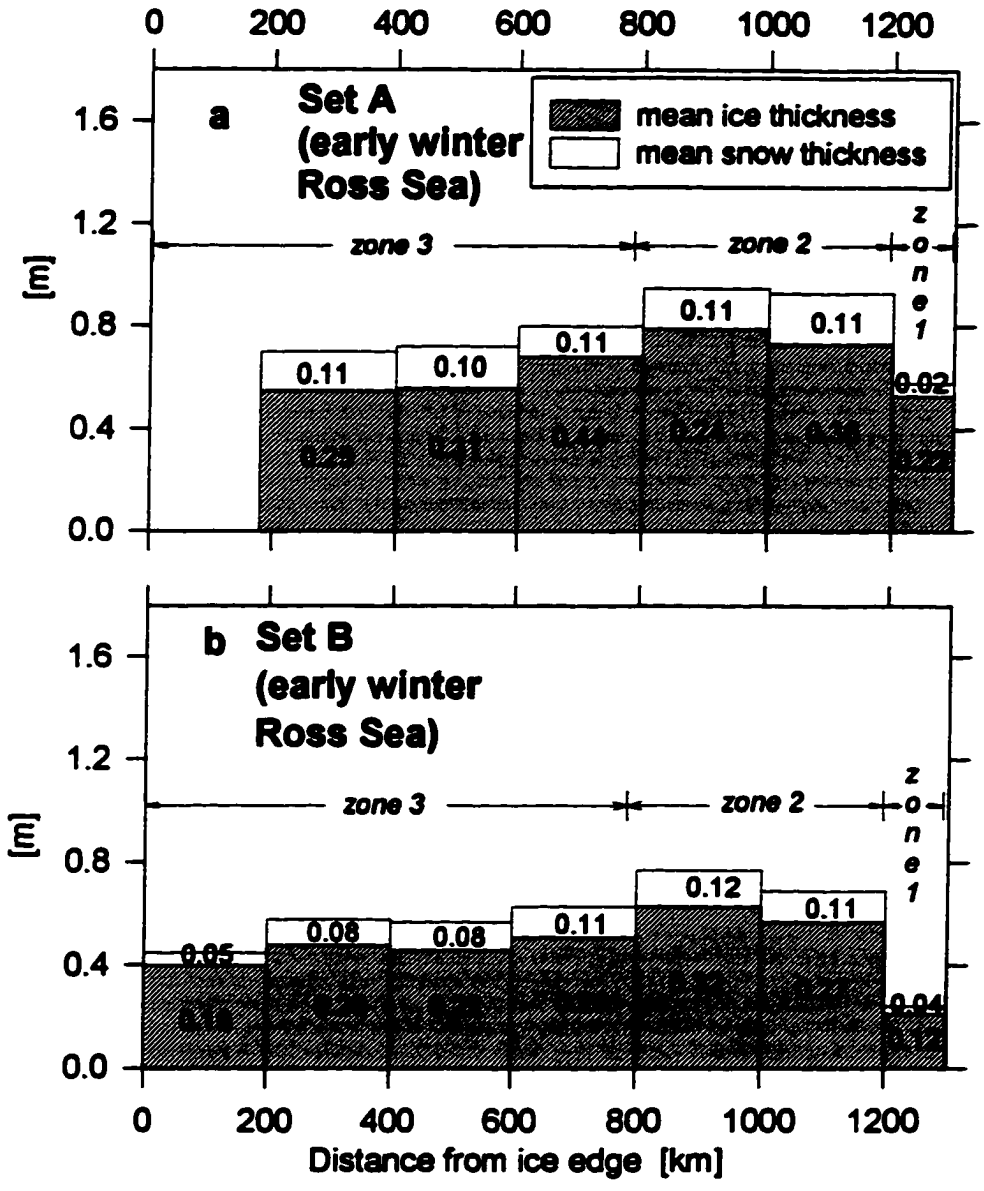

Figure I.3. Mean values of ice thicknesses and snow depth sorted in distance classes from the ice edge: a), b) for Set A and Set B data of the early winter Ross Sea cruise, c), d) for Set A and Set B data of the late winter Ross Sea cruise. Corresponding standard deviations are indicated as numbers.

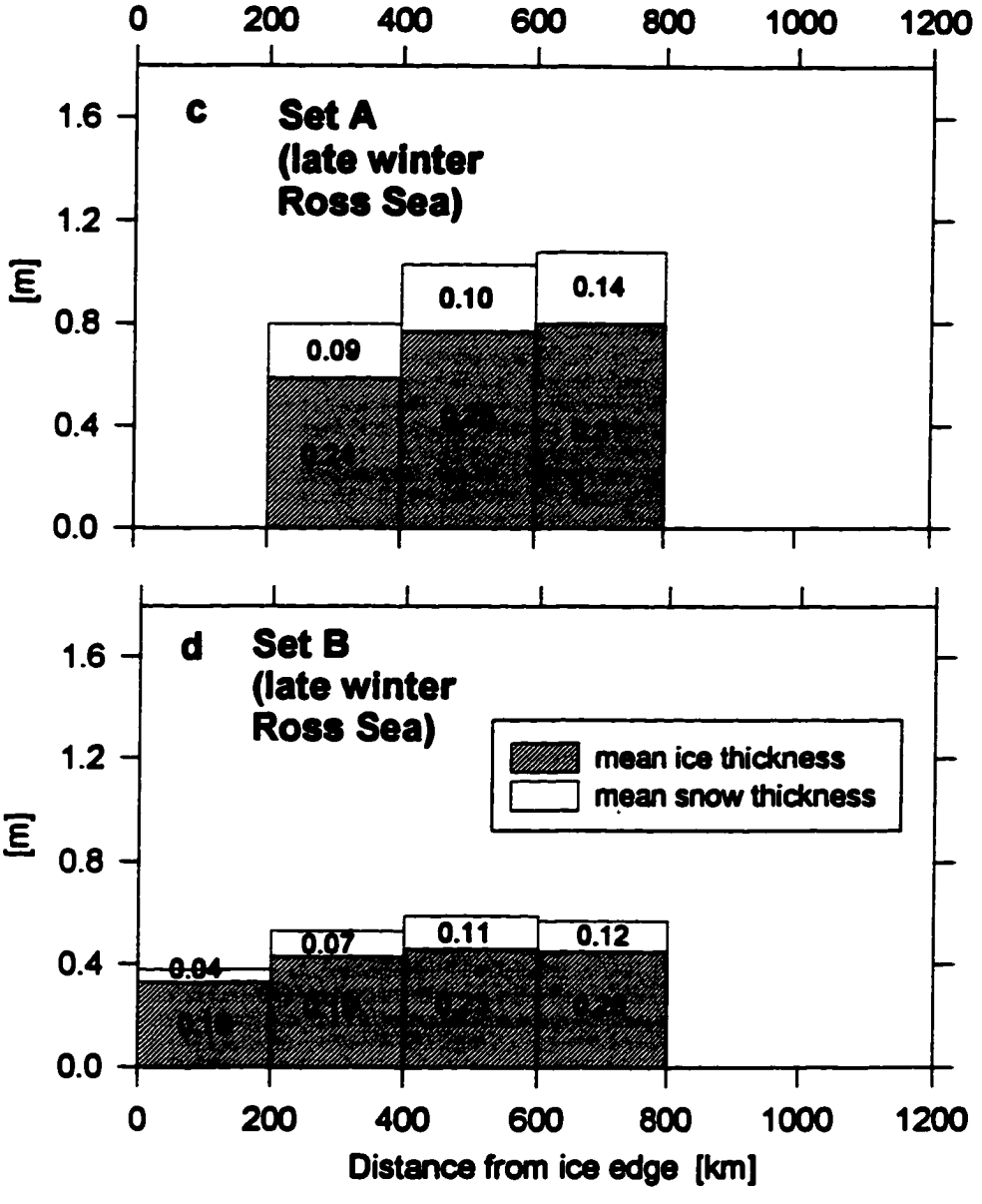

Figure I.3: (continued).

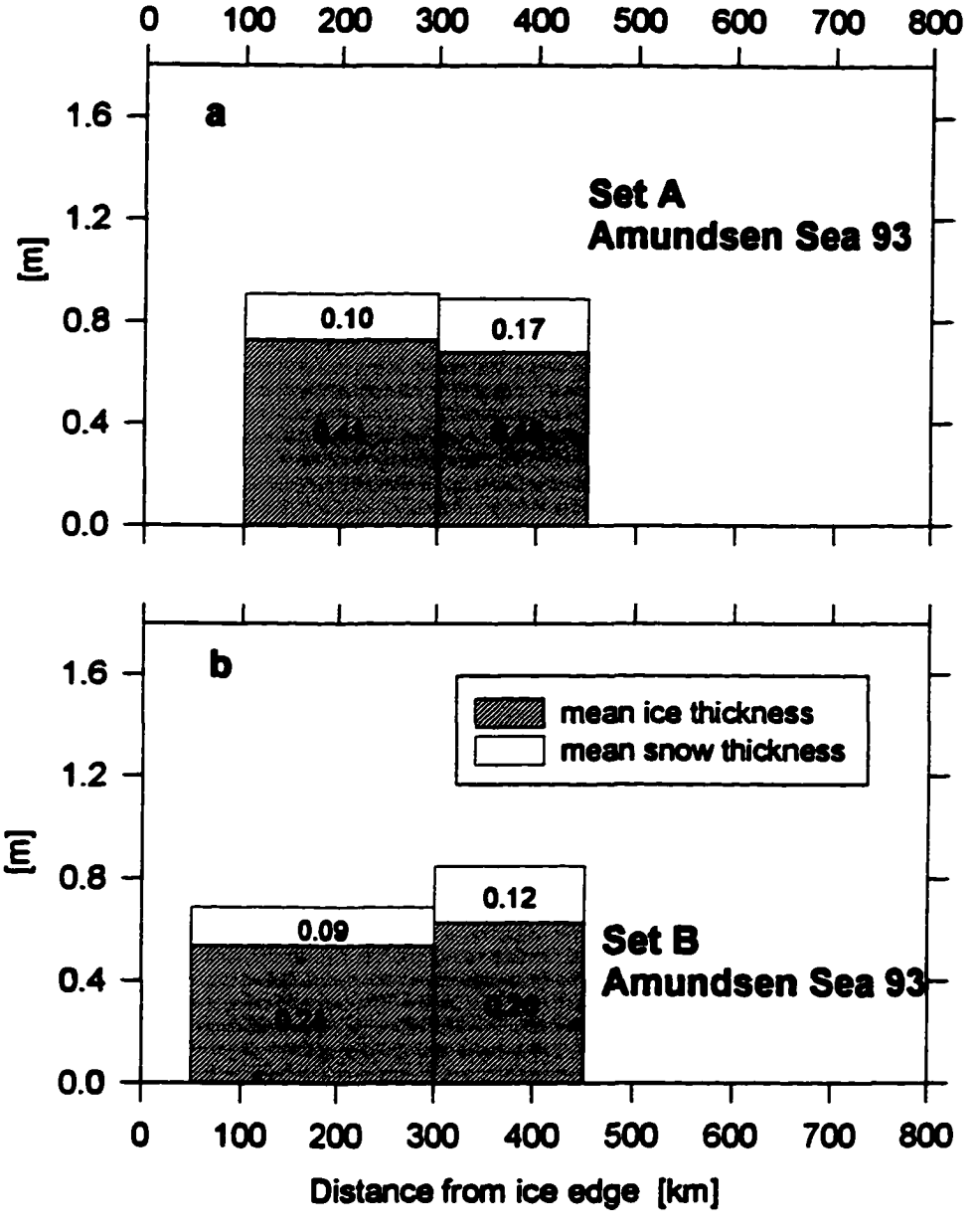

Figure I.4. Mean values of ice thicknesses and snow depth sorted in distance classes from the ice edge: a), b) for Set A and Set B data of the Amundsen and Bellingshausen Seas in late winter 1993, c), d) in late winter 1995. Corresponding standard deviations are indicated as numbers (in [m]).

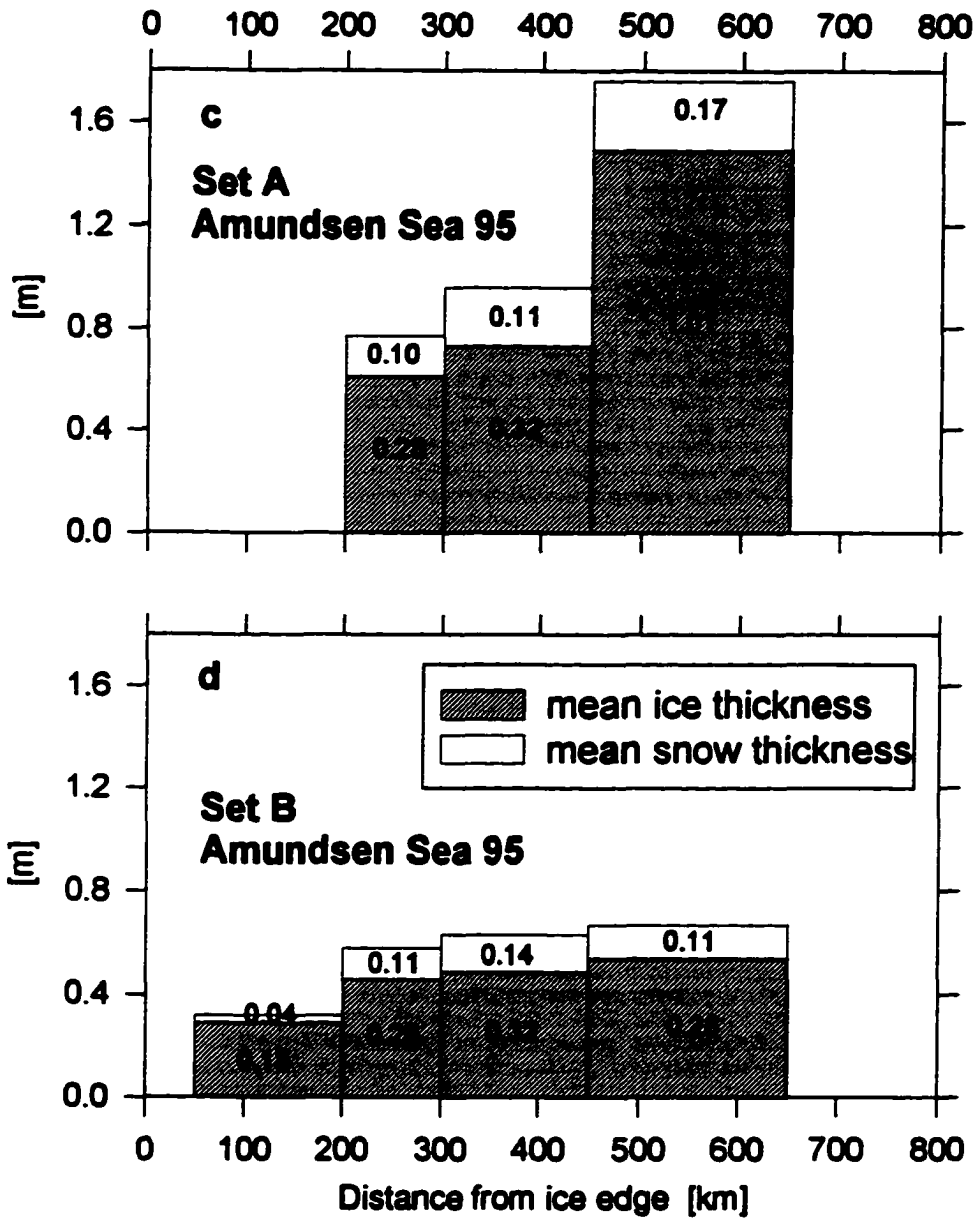

Figure I.4: (continued).

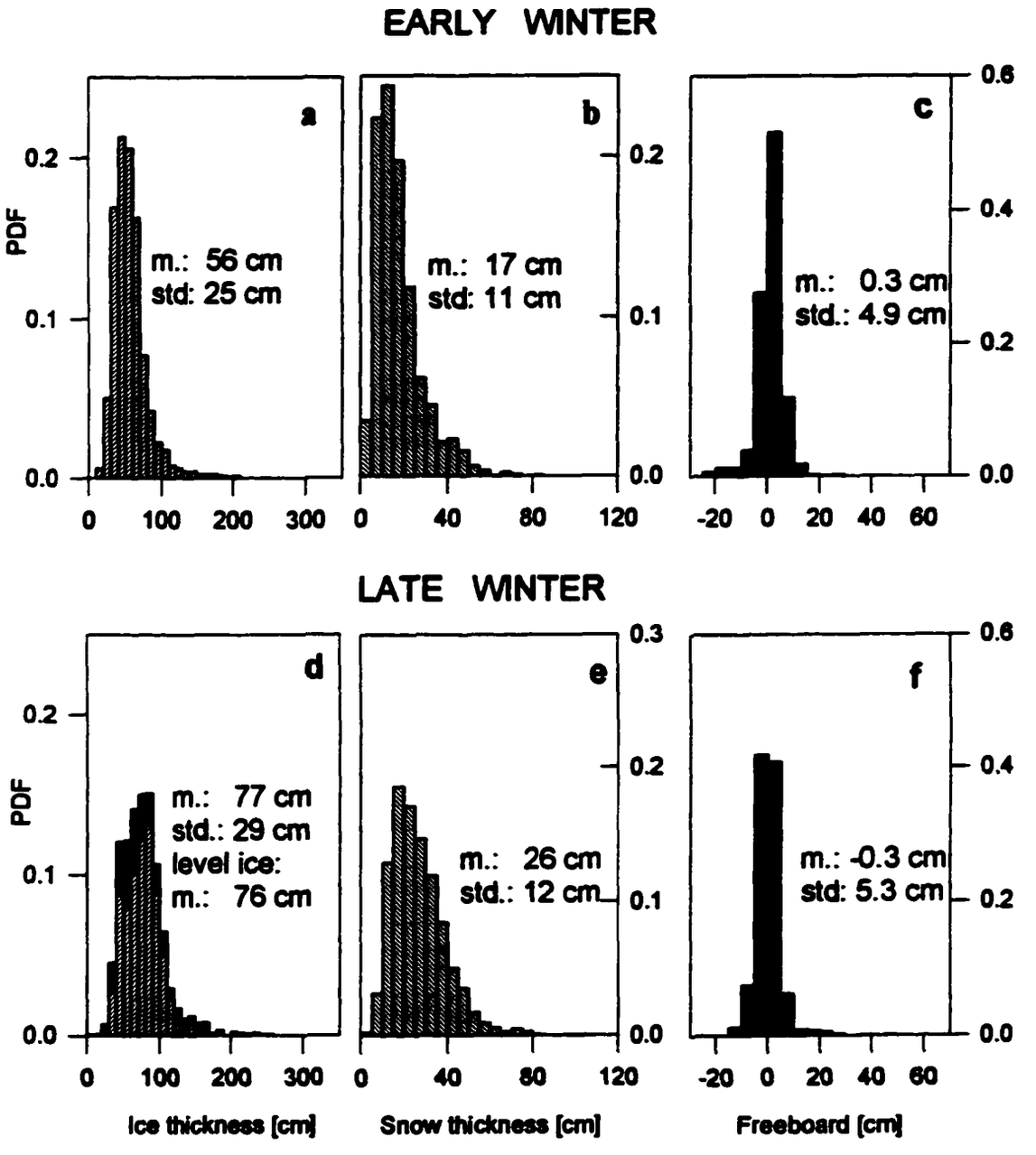

Figure I.5. Probability Density Functions (PDF) of drilling data (Set A) for the early (a,b,c) and late winter (d,e,f) Ross Sea cruises in their common area of overlap between 64.87° S and 70.62° S. Dark areas in (d) indicate the contribution of ridging for the late winter Ross Sea.

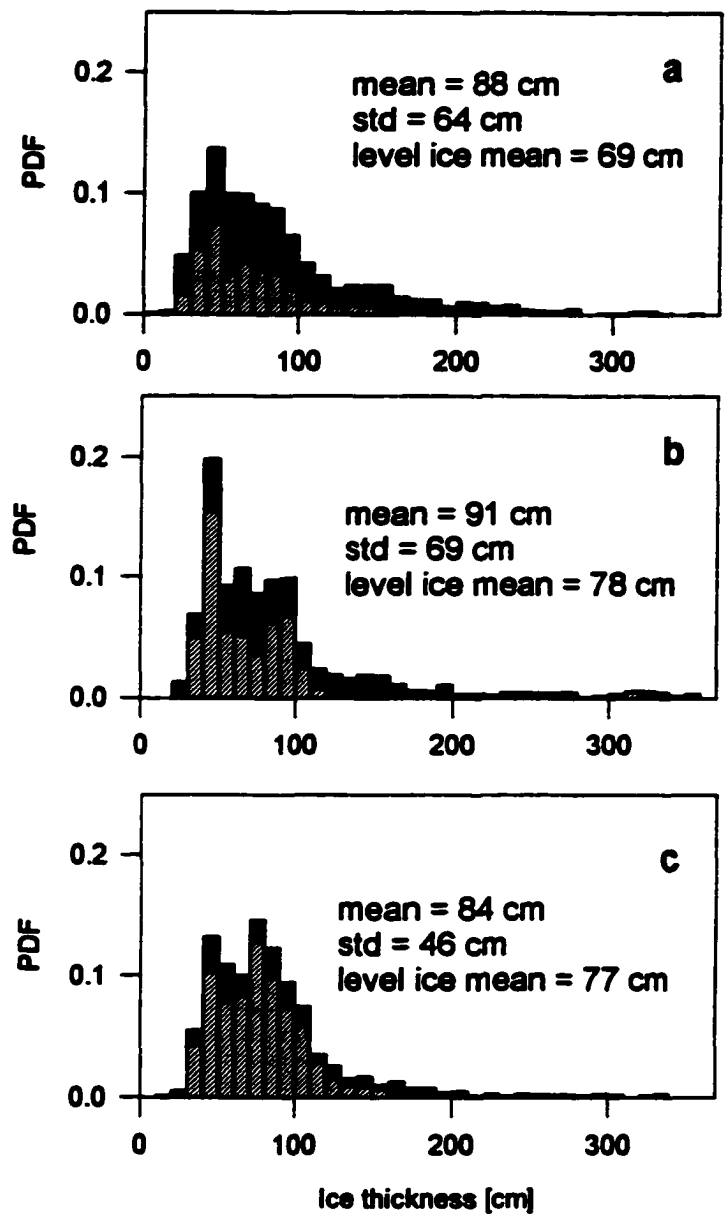

Figure I.6: Probability Density Functions (PDF) of ice thickness for the drilling data (Set A) of the Amundsen and Bellingshausen Seas in 1993 (a), 1995(b) and for cruise NBP 94(c). Means, standard deviations (std) and mean level ice thicknesses are also indicated. Shaded areas show the contribution of ridging in the respective areas.

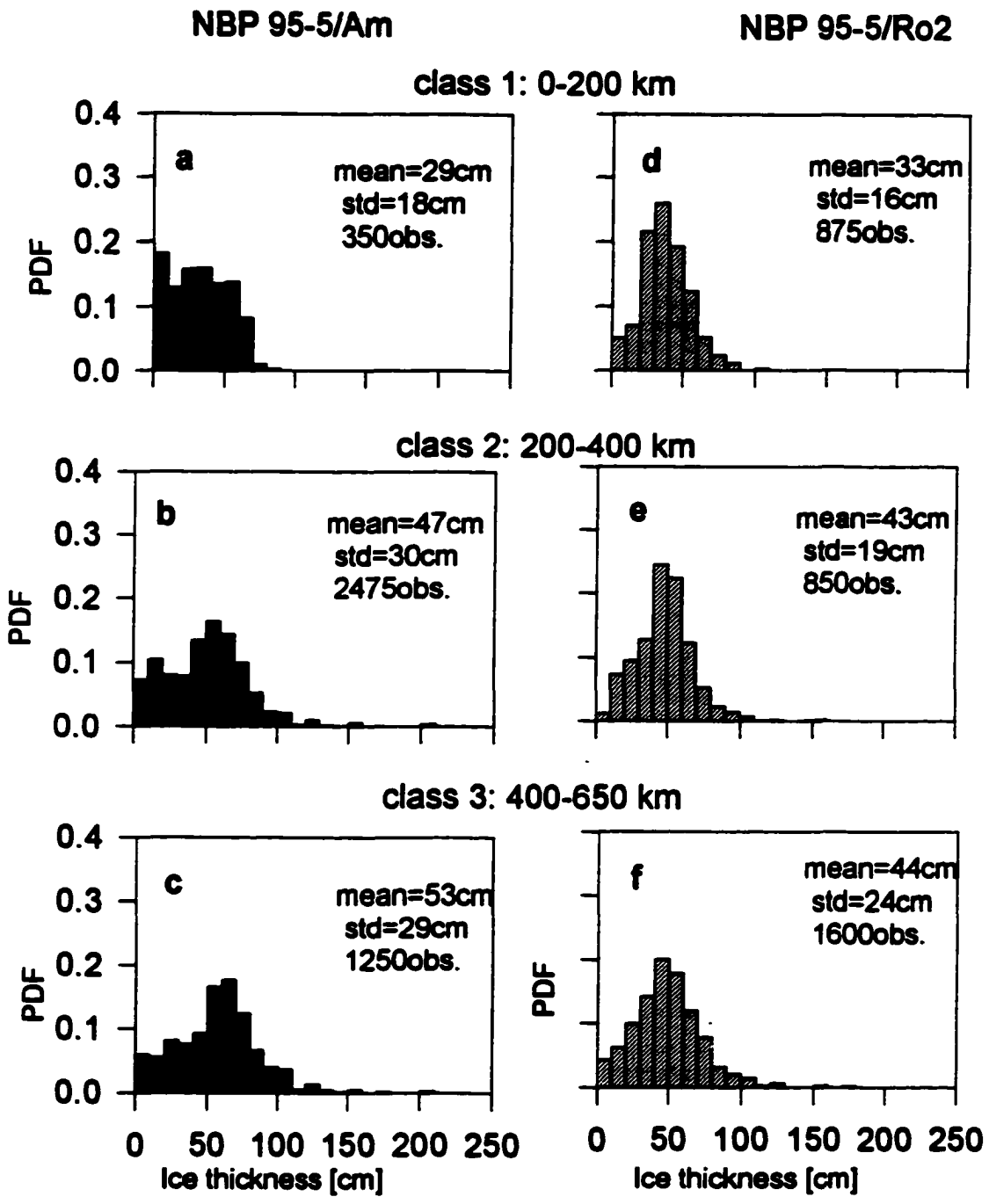

Figure I.7: Ice thickness distribution functions (PDF) of the continuous shipboard measurement (Set B) for the Amundsen and Bellingshausen Seas (a, b and c) and the Ross Sea (d, e and f) in late winter 1995, sorted in three, common distance classes from the ice edge. Mean values, standard deviations (std) and numbers of observations are indicated in the graphs.

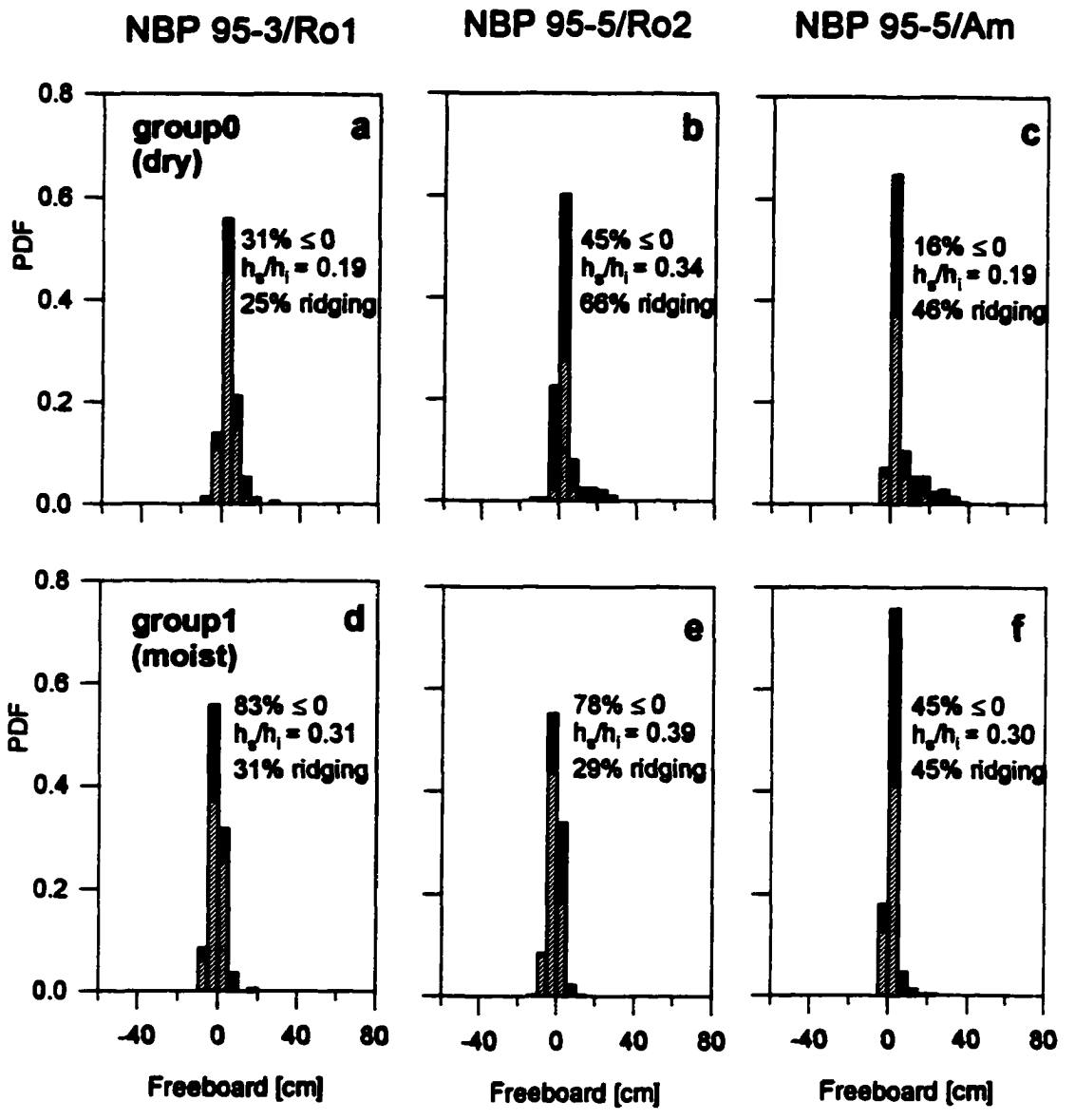

Figure I.8. Probability Density Functions (PDF) of freeboard for the early winter Ross Sea (first column), the late winter Ross Sea (second column) and the late winter Amundsen and Bellingshausen Seas (third column) in 1995, sorted into groups of different degree of moisture prior to drilling. Group 0 (a,b,c) indicates dry locations, group 1 (d,e,f) moist locations, group 2 (g,h,i) wet locations and group 3 (j,k,l) locations, which were detected as slushy or flooded. The relative amount of zero or negative freeboard (in %), mean snow/ice thickness ratios and the contribution of ridging (dark areas) are also indicated in the corresponding graphs.

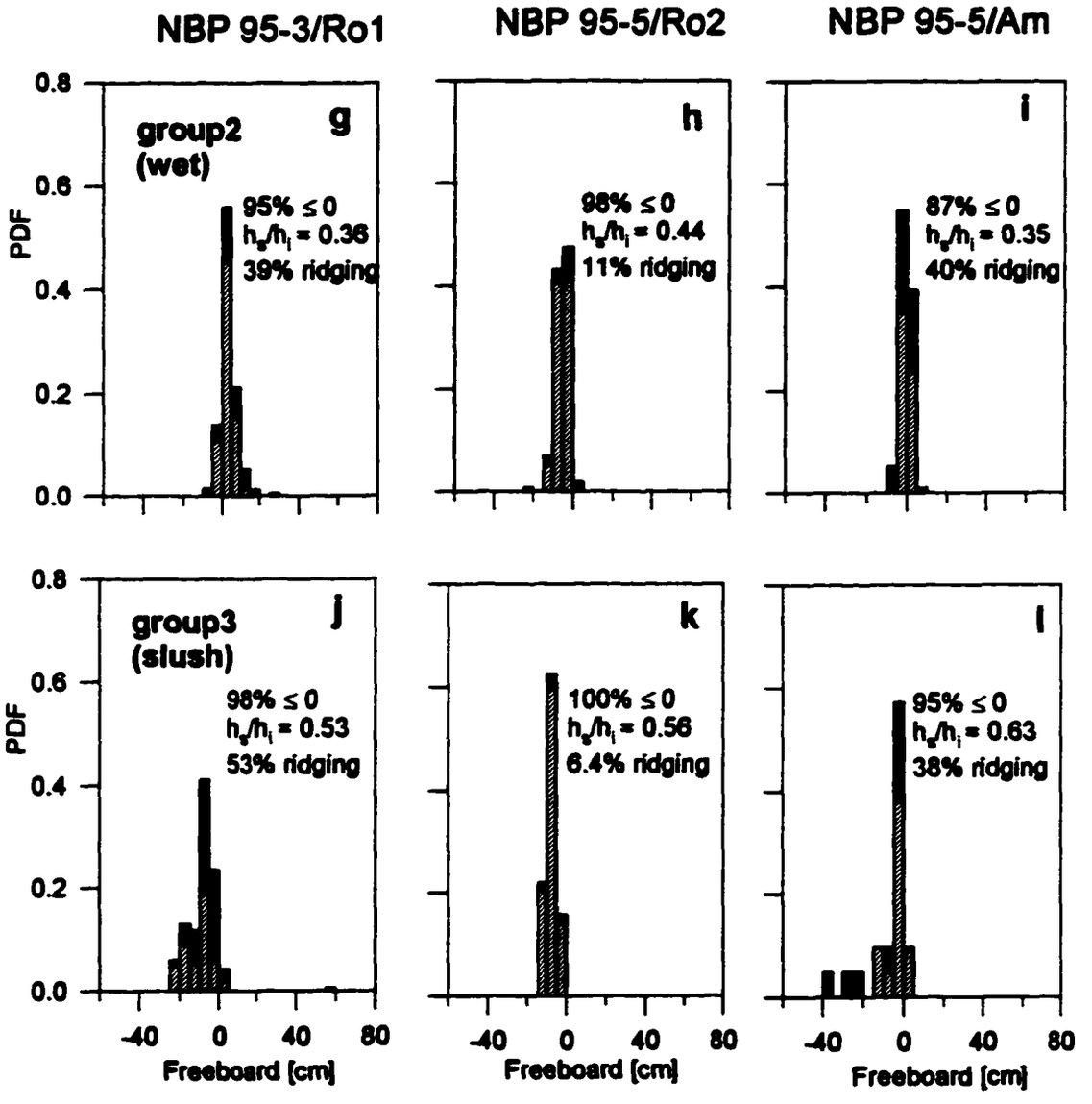

Figure I.8. (continued)

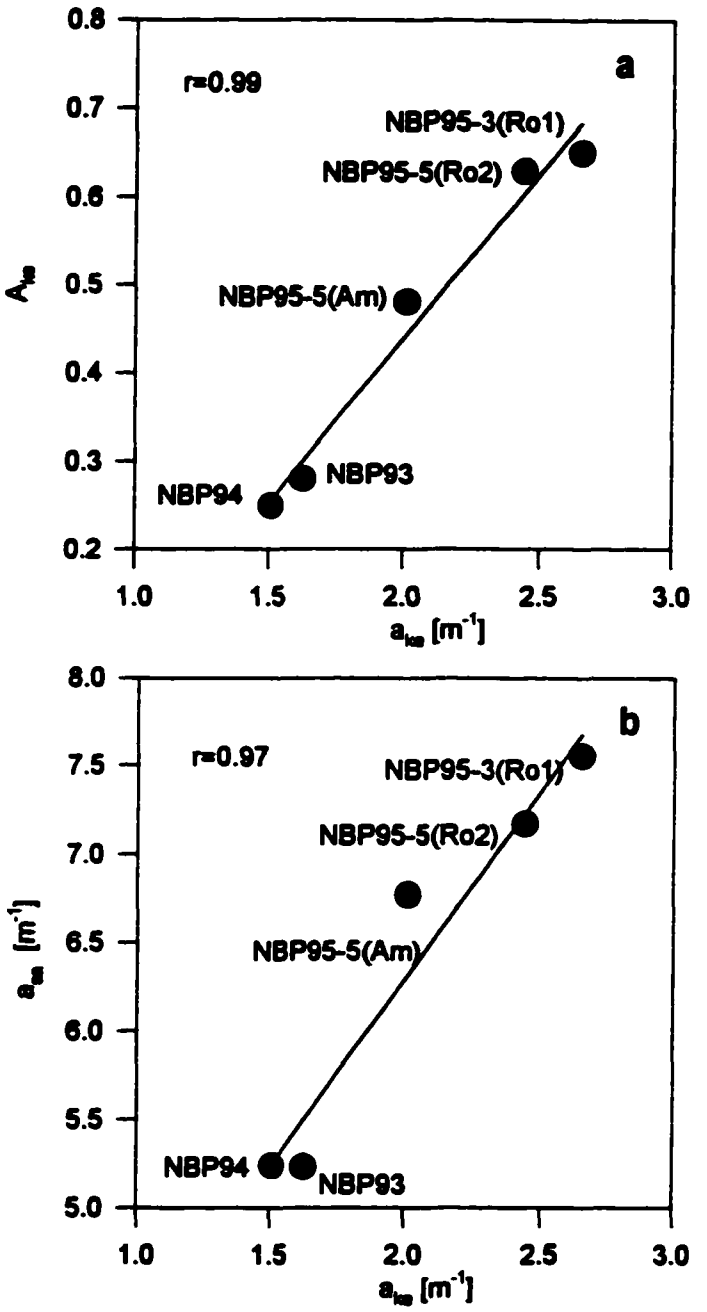

Figure I.9: Linear fits (a) between underside amplitudes A_{ke} (ke=keel) and decay parameter a_{ke} and (b) between decay parameters of sail (sa) and keel (ke) distributions. Amplitudes and decay parameter are given for the entire data set of each cruise.

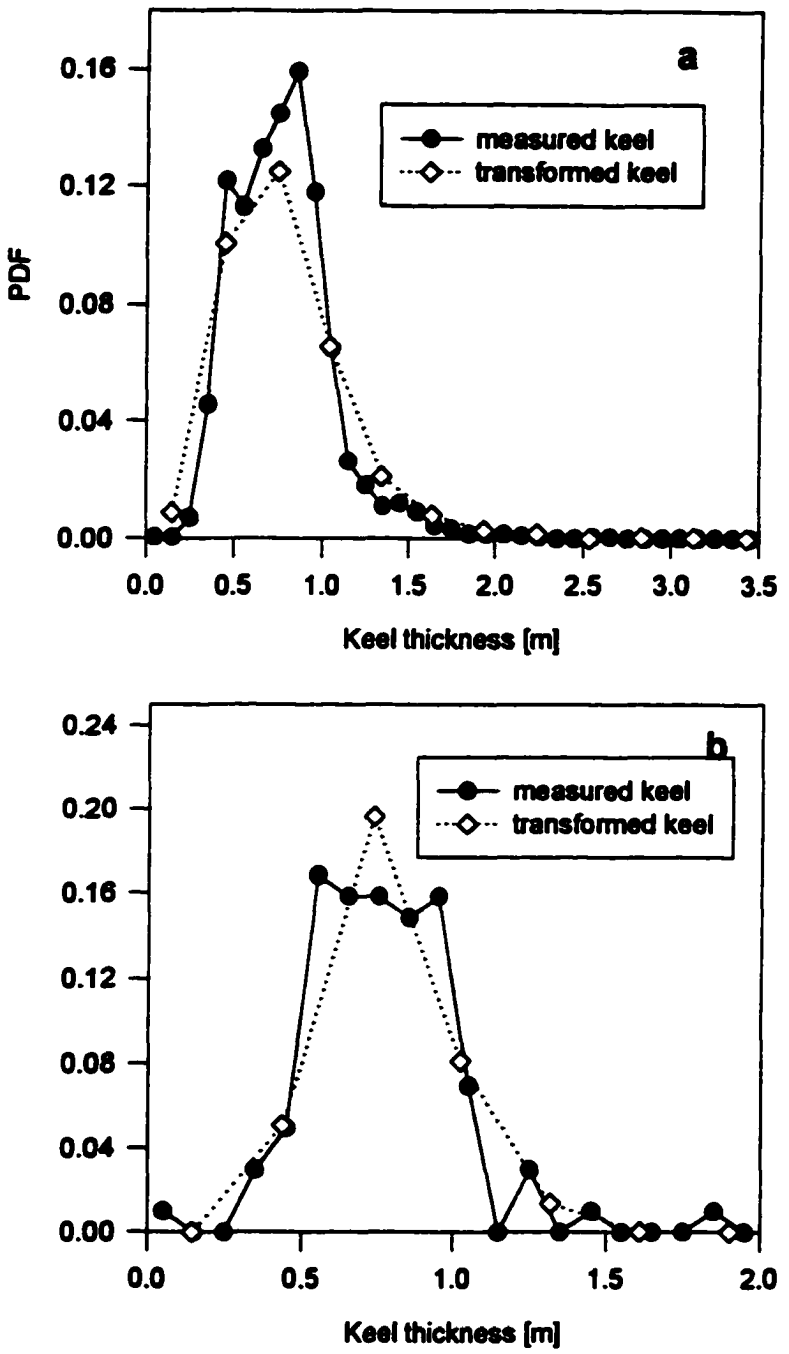

Figure I.10. Results of a scale transformation with factor R for all data of the late winter Ross Sea cruise (a) and for a single profile (b) at julian day 230 of that cruise. The transformed sail distribution (diamonds) is compared to the measured keel distribution (circles).

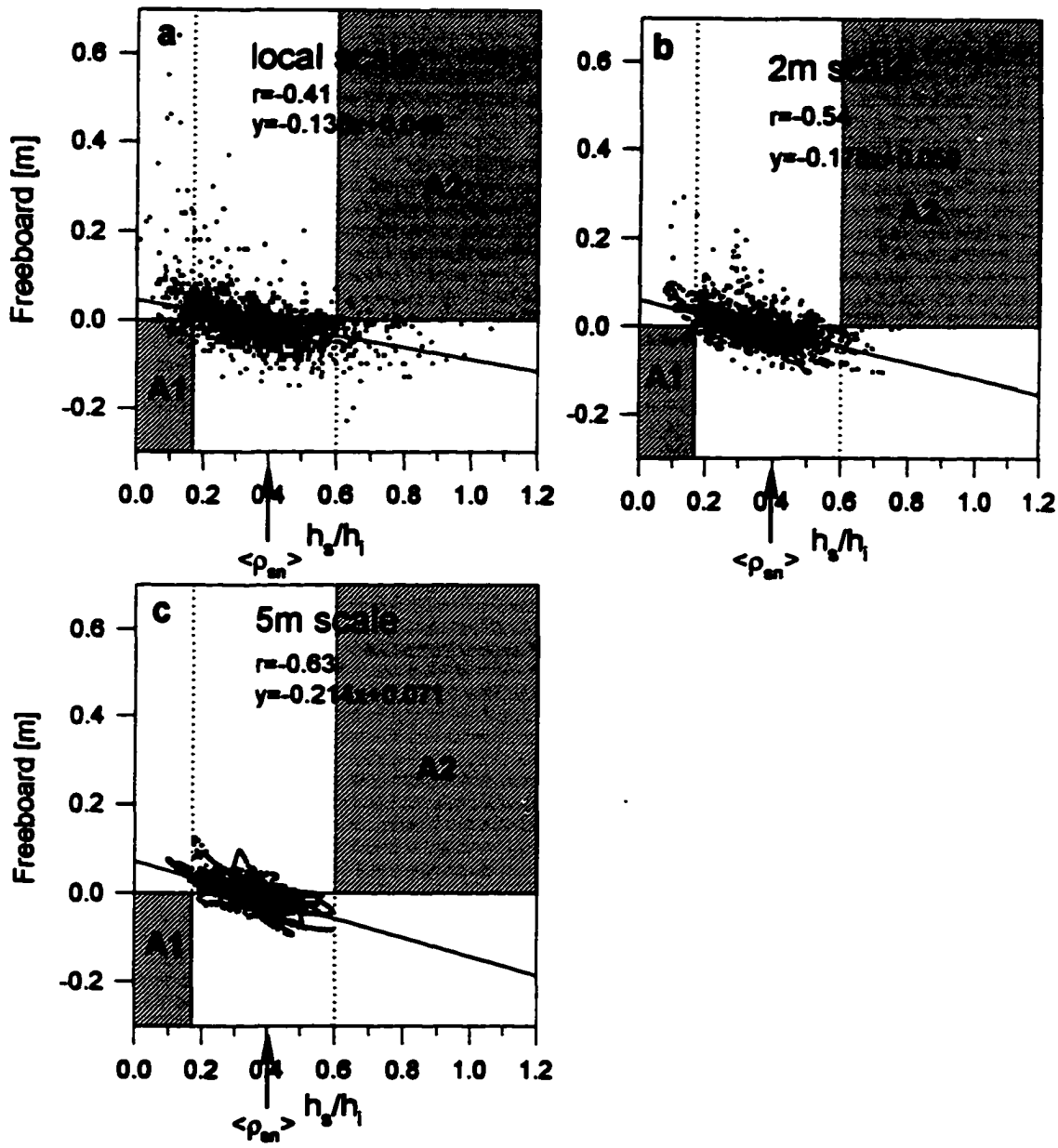

Figure I.11. Snow/ice thickness ratios graphed versus freeboard for the late winter Ross Sea (a, b and c) and the Bellingshausen and Amundsen Sea (d, e and f) in 1995. The scale of averaging advances from left (local scale for a and d), to right (2 m average in b, 1 m average in e, 5 m average in c and f). The region within the two dotted lines refers to snow/ice thickness values which correspond to a maximum snow density range of 0.20 to 0.70g cm-3. The hatched areas A1 and A2 indicate the two regions of isostatic instability. Arrows point to the minimal snow/ice thickness vaiue which leads to flooding for the corresponding mean snow density of the cruise. Correlation coefficients and regression lines and their equations are shown in the graphs.

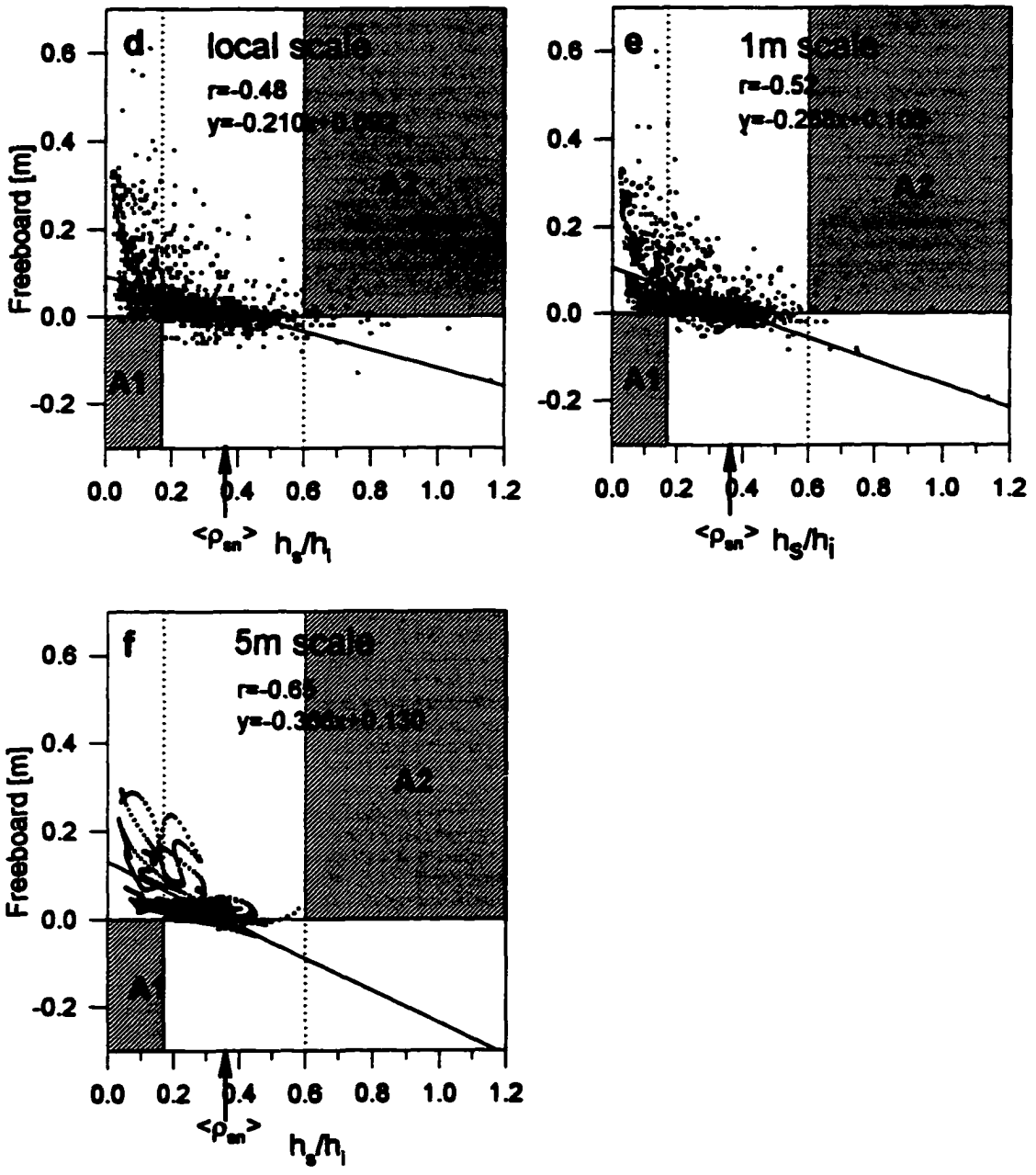

Figure I.11: (continued)

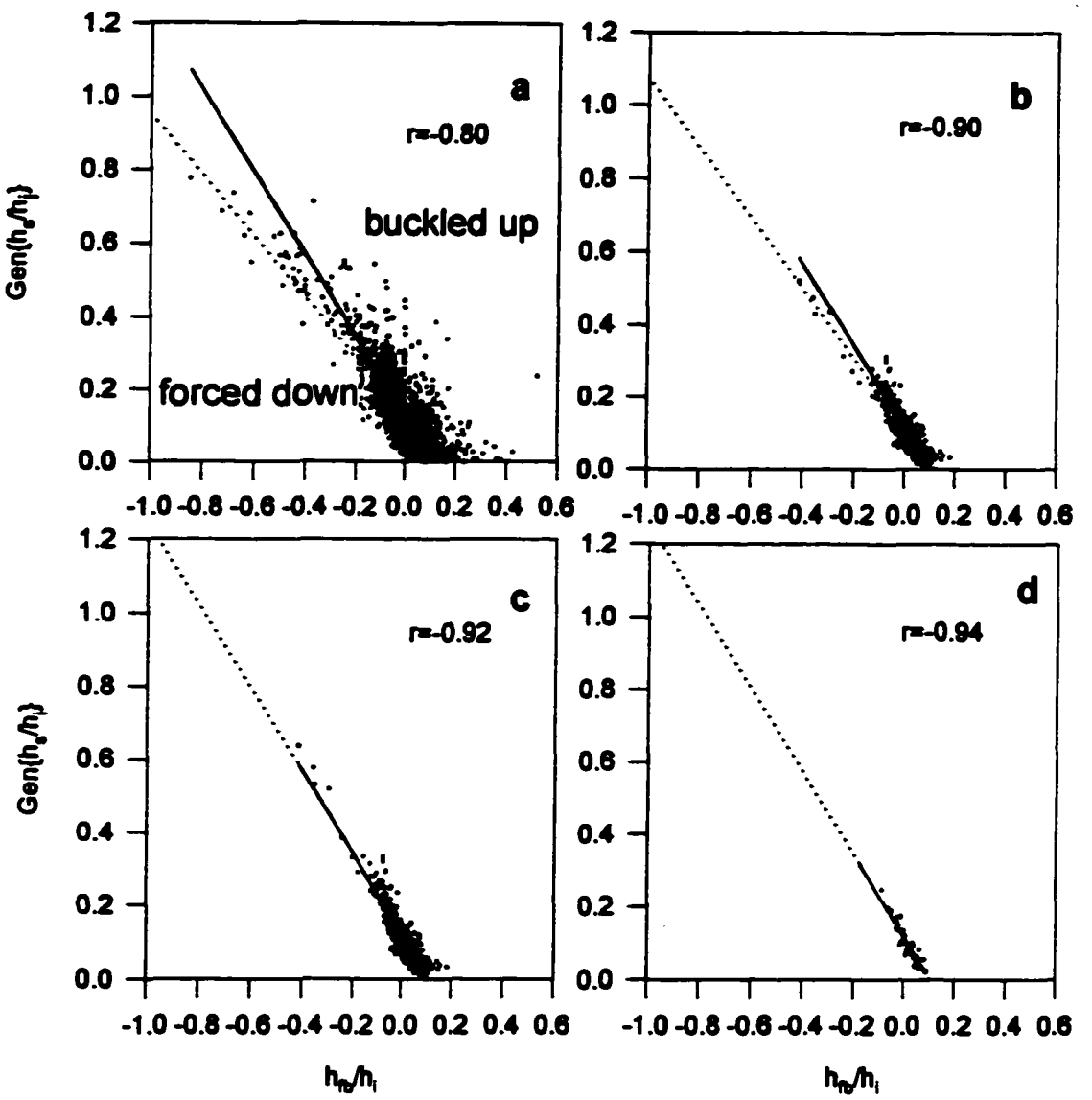

Figure I.12. GSI versus freeboard/ice thickness for all data of the early winter Ross Sea cruise. (a) shows all data on a local scale by applying the mean snow density (0.34g cm^{-3}) and a slush density of 0.70g cm^{-3} (highest measured value), (b) shows the result of a 5 m average, (c) shows the 5 m average by applying a maximum slush density of 0.96g cm^{-3} (calculated), (d) is the result of further averaging to the level of profiles. Lines of regression (dotted lines) can be compared to the isostatic line (solid line).

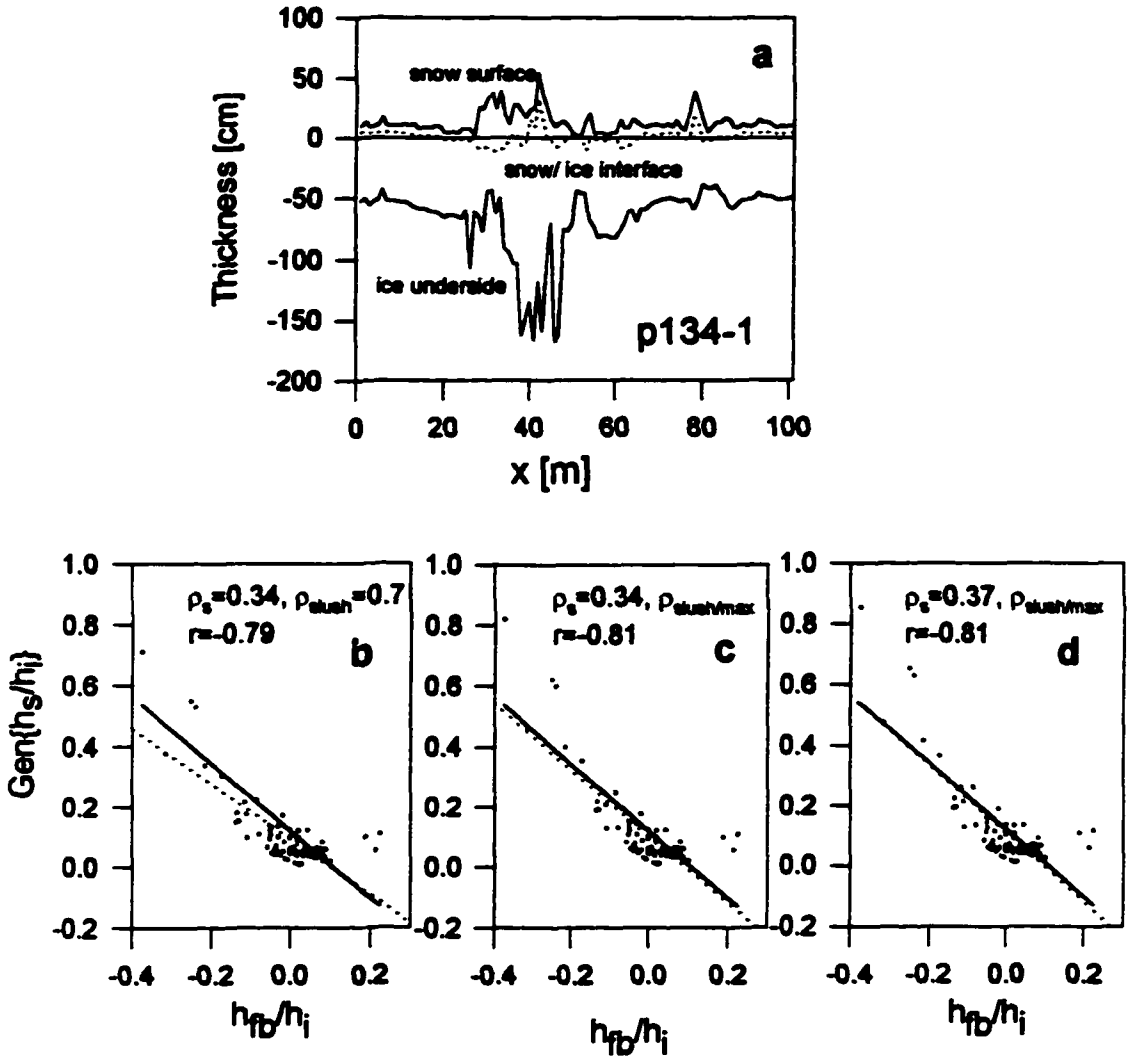

Figure I.13: GSI versus freeboard/ice thickness for single profiles of the early winter Ross Sea (a, e) and the late winter Amundsen and Bellingshausen Seas (i). The lines of regression (dashed lines) approach the isostatic line (solid line) by variation of snow and slush density. Data are shown on a local, non averaged scale except graphs (k) and (l) where 5 m averaging was necessary.

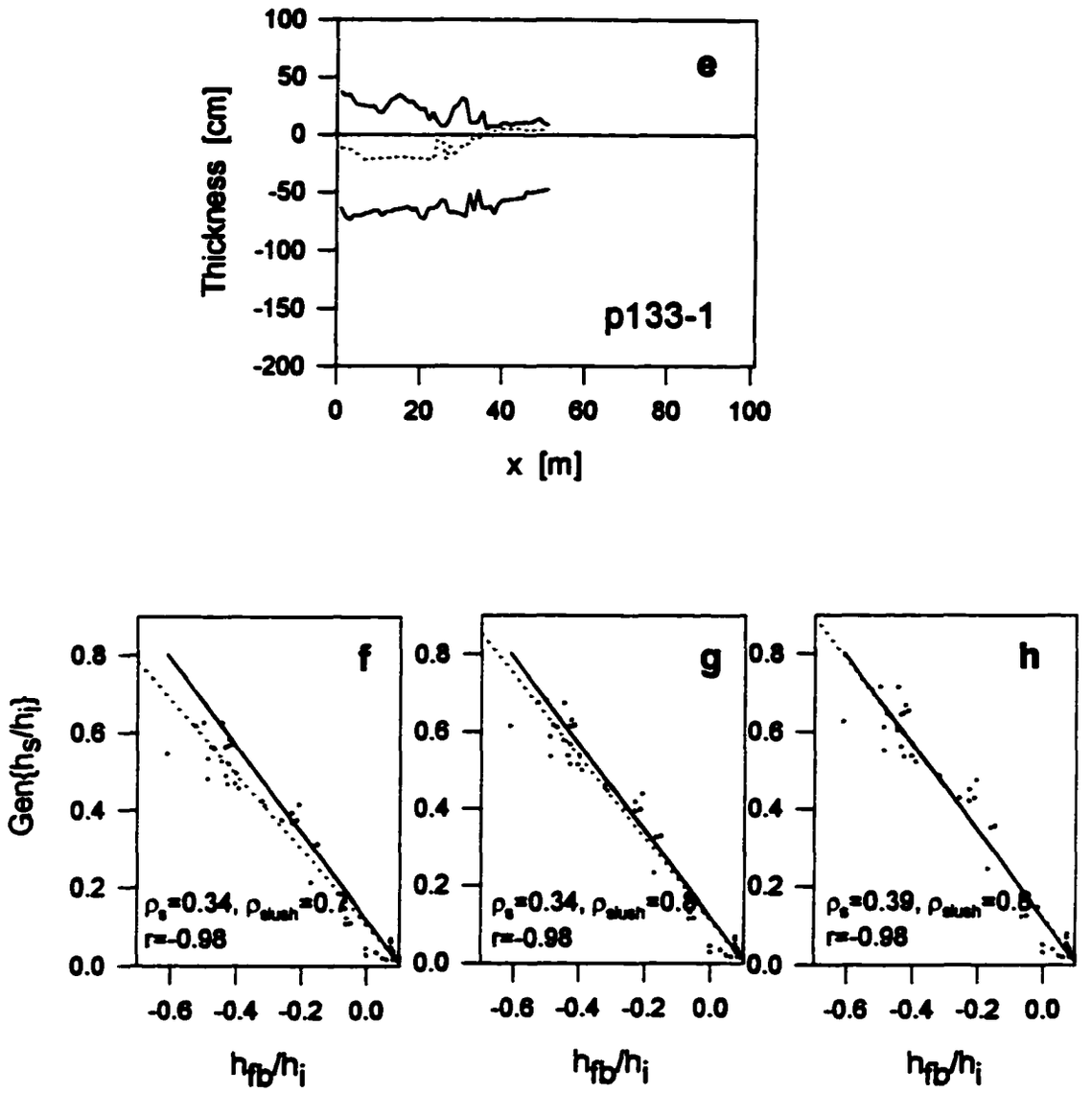

Figure I.13: (continued - 1)

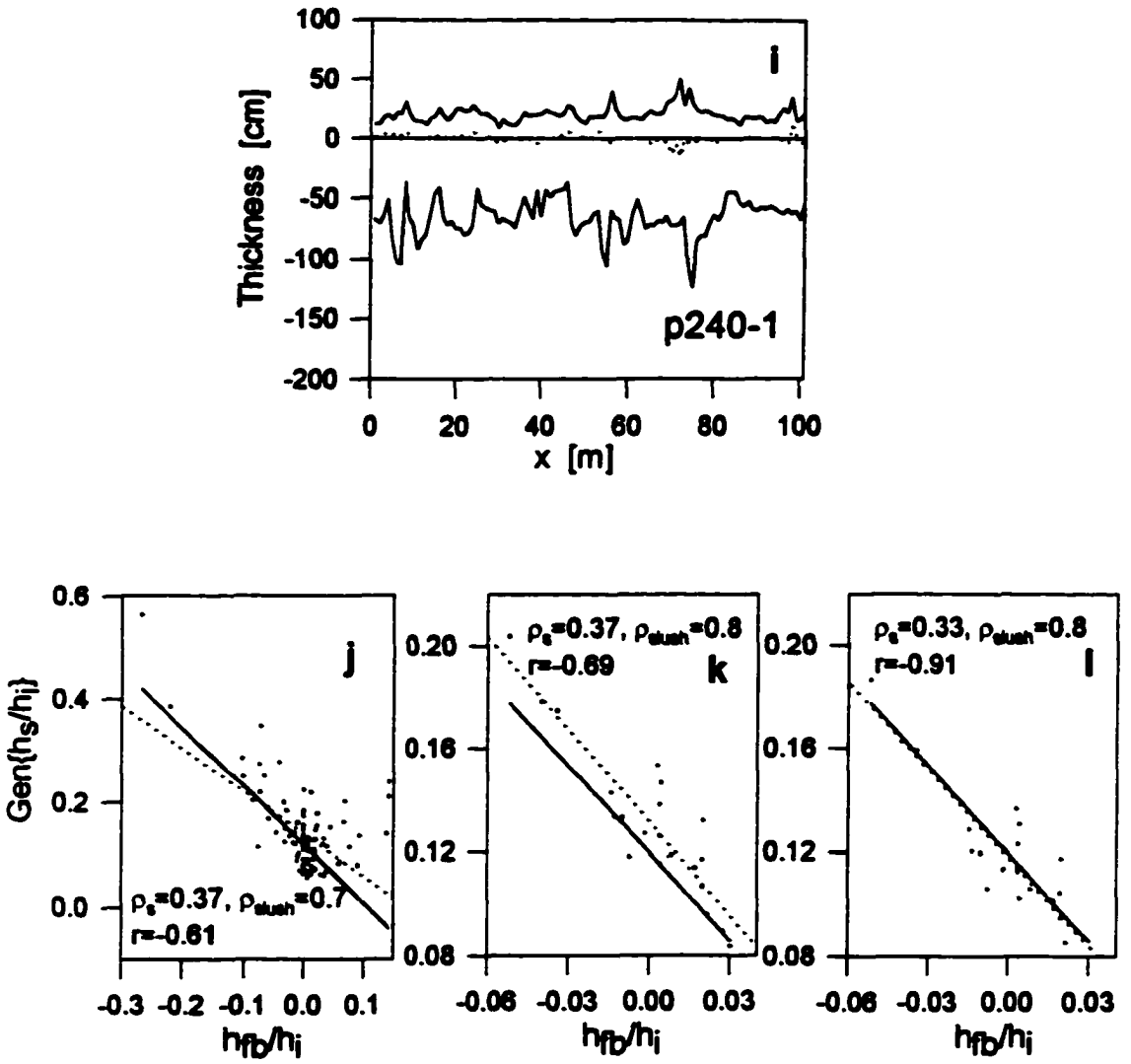

Figure I.13: (continued - 2)

I.11 Tables

Table I.1 a. Geographical coverage, dates and seasons of the NBP cruises discussed in the text. b. Snow and ice thickness mean values and standard deviations (std), given in cm, for data Sets A and B for all cruises.

cruise	area	dates	season
NBP 93	Amundsen and Bellingshausen Seas	August 17-September 23, 1993	late winter 93
NBP 94	Amundsen and north western Ross Sea	September 19-October 12, 1994	late winter 94
NBP 95-3/Ro1 [1)]	Ross Sea	May 10-June 13, 1995	early winter 95
NBP 95-5/Ro2 [2)]	Ross Sea	August 5-August 19, 1995	late winter 95
NBP 95-5/Am [3)]	Amundsen and Bellingshausen Seas	August 28-September 11, 1995	late winter 95

Table I.1b

cruise	ice stations (Set A)									continuous measurements (Set B)		
	number of holes	number of floes	h_{ice} (std)	h_{snow} (std)	$h_{freeboard}$ (std)	free-board < 0 (≤ 0)	ridging [4]	$h_{levelice}$ (std)	$h_{ridgedice}$ (std)	number of observa-tions	h_{ice} (std)	h_{snow} (std)
NBP 93	1142	29	88 (64)	23 (16)	2.6 (6.8)	18 (32)	62	69 (35)	98 (68)	4051	61 (27)	21 (12)
NBP 94	2235	23	84 (46)	28 (16)	-0.8 (6.0)	50 (64)	25	77 (28)	106 (73)	9673	52 (25)	16 (10)
NBP 95-3/Ro1 [1]	3670	29	65 (33)	15 (11)	1.4 (5.5)	29 (46)	34	59 (18)	76 (48)	11114	51 (27)	11 (10)
NBP 95-5/Ro2 [2]	2078	14	77 (29)	26 (12)	-0.3 (5.3)	51 (66)	25	76 (25)	77 (40)	7167	45 (27)	12 (11)
NBP 95-5/Am [3]	2095	14	91 (69)	22 (14)	3.4 (7.4)	14 (30)	45	78 (59)	108 (75)	6949	50 (31)	13 (13)

[1] early winter Ross Sea (May/June 1995)

[2] late winter Ross Sea (August 1995)

[3] late winter Amundsen and Bellingshausen Seas (August/September 1995)

[4] Negative freeboard and ridging are given in percent. Ridging, mean thicknesses for ridged and level ice in the drilling data were obtained using the Rayleigh ridge criterion.

Table I.2. Decay parameters (a) and amplitudes (A) of an exponential fit for the sail (sa) and keel (ke) distributions of all cruises.

cruise	sail		keel		R [4]
	A_{sa}	a_{sa} [1/m]	A_{ke}	a_{ke} [1/m]	$= \frac{\langle h_{ke} \rangle}{\langle h_{sa} \rangle}$
NBP 93	1.04	5.23	0.28	1.63	3.27
NBP 94	1.05	5.24	0.25	1.51	3.16
NBP 95-3/Ro1 [1]	1.43	7.55	0.65	2.65	3.79
NBP 95-5/Ro2 [2]	2.09	7.17	0.63	2.44	2.98
NBP 95-5/Am [3]	2.00	6.77	0.48	2.01	3.49

[1] early winter Ross Sea (May/June 1995)
[2] late winter Ross Sea (August 1995)
[3] late winter Amundsen and Bellingshausen Seas (August/September 1995)
[4] R is the factor for a scale transformation which converts from sail to keel distribution.

Table I.3. Correlation coefficients between thickness variables of snow, freeboard, ice, sail and keel on different spatial scales for all data of each cruise.

	scale	r (h_{sail},h_{keel})	r (h_{snow}/h_{ice},h_{fb})
NBP 93	local[4]	0.65	-0.33
	2m	0.75	-0.48
	5m	0.79	-0.58
	profile[5]	0.80	-0.67
NBP 94	local	0.74	-0.55
	2m	0.82	-0.68
	5m	0.86	-0.75
	profile	0.89	-0.83
NBP 95-3/Ro1 [1]	local	0.41	-0.64
	2m	0.53	-0.78
	5m	0.59	-0.85
	profile	0.70	-0.89
NBP 95-5/Ro2 [2]	local	0.56	-0.41
	2m	0.70	-0.54
	5m	0.78	-0.63
	profile	0.88	-0.65
NBP 95-5/Am [3]	local	0.71	-0.48
	2m	0.78	-0.57
	5m	0.82	-0.65
	profile	0.89	-0.70

[1] early winter Ross Sea (May/June 1995)
[2] late winter Ross Sea (August 1995)
[3] late winter Amundsen and Bellingshausen Seas (August/September 1995)
[4] local scale refers to unaveraged scale
[5] a typical profile scale corresponds to about 100m

Table I.4. Correlations between GSI and freeboard/ice thickness ratio for mean snow densities and different slush densities on two different spatial levels.

		correlations between Gen{h_{snow}/h_{ice}} and h_f/h_{ice}		
		local scale		scale of profiles
cruise	$<\rho_{snow}>$	ρ_{slush}=0.7	$\rho_{slush/max}$ [5]	ρ_{slush}=0.7
NBP 93	0.36 [4]	-0.43	-0.48	-0.85
NBP 94	0.36	-0.76	-0.81	-0.86
NBP 95-3/Ro1 [1]	0.34	-0.80	-0.83	-0.93
NBP 95-5/Ro2 [2]	0.40	-0.53	-0.58	-0.75
NBP 95-5/Am [3]	0.37	-0.69	-0.72	-0.87

[1] early winter Ross Sea (May/June 1995)
[2] late winter Ross Sea (August 1995)
[3] late winter Amundsen and Bellingshausen Seas (August/September 1995)
[4] assumed value, since no mean bulk density was calculated for this cruise
[5] value for maximum slush density according to equation (9)

Table I.5. A comparison of equations (10), (11) and (12) and their ratios. Values of ρ_w and ρ_i of 1.03 and 0.91 g cm $^{-3}$ were used.

effect	equation	cause	ratios
subsidence	$\Delta y_s=0.88\Delta x_s$	due to snow fall Δx_s	$\Delta y_s/\Delta y_m=8\rho_s(\Delta x_s/\Delta x_m)$
subsidence	$\Delta y_m=0.11/\rho_s(\Delta x_m)$	due to bottom melting Δx_m	$\Delta y_s/\Delta y_g=(\Delta x_s/\Delta x_g)$
uplift	$\Delta y_g=-0.88\Delta x_g$	due to ice growth Δx_g	$\Delta y_m/\Delta y_g=0.13/\rho_s\,(\Delta x_m/\Delta x_g)$

II. Roughness variability of sea ice and snow cover thickness profiles in the Ross, Amundsen and Bellingshausen Seas

II.1 Abstract

An investigation of top and bottom surface roughness was carried out on snow and ice thickness profiles sampled on 57 floes in the Ross, Amundsen and Bellingshausen Seas between May and September 1995. An objective classification scheme was used to group the studied sea ice floes according to the degree of deformation they had undergone. Different roughness criteria and methods were applied to the classified floes. Roughness variance and properties derived from the Fourier spectra, such as fractal dimensions, depend critically on the deformational history of the floes under consideration. Semivariograms of the sea ice profiles indicate that the snow surface and the ice underside are smoother than the snow-ice interface, which is the roughest surface. The wavelet transform is presented as a new method to find dominant structure lengths as well as to localize these structure lengths in the studied profiles. For individual profiles the maximum entropy method provided spectra that are less noisy than corresponding Fourier power spectra. Finally, air, water and ice surface drag coefficients are calculated from the surface roughness characteristics. Air drag coefficients ranged between 1.1 and 1.7 $\times 10^3$ and increased with increasingly deformed ice.

II.2 Introduction

Knowledge of the roughness characteristics and the spatial variability of a sea ice cover is important for several reasons. Roughness characteristics of the snow surface determine the air drag at the air-sea ice boundary and thereby the magnitude of the turbulent fluxes of sensible and latent heat. Roughness parameters can also be used to classify entire sea ice regimes in terms of geographical region or seasonal stage. On the

other hand roughness can be used as a qualifier or descriptor of the developmental history of a single floe. As such, roughness is an important variable for describing ice types.

Large scale roughness, such as sea ice ridging, has been measured with airborne laser profilometers [*Tucker et al.*, 1979; *Weeks et al.*, 1989; *Govoni et al.*, 1983] as well as with ship based acoustic sounders [*Lytle and Ackley*, 1991]. As a result of these studies, typical ridge frequencies and heights have been found for various regions of Antarctic and Arctic sea ice.

An additional potential technique for measuring roughness recently became available with the launch of spaceborne Synthetic Aperture Radar (SAR) systems. On SAR images 'smooth' surfaces with a vertical relief smaller than a critical value (depending on the radar wavelength and angle of incidence) appear dark (low back scatter) while 'rough' surfaces with a vertical relief larger than this critical value appear bright (high back scatter). Unfortunately this critical vertical relief is on the millimeter to centimeter scale for the most commonly used C-band SAR [*Paterson et al.*, 1991]. This makes it difficult with SAR to distinguish micro-scale roughness from macro-scale roughness features such as ridges, rubble, floe edges or rafted floes. Another complicating factor is that the back scatter is equally sensitive to material properties within the floe such as dielectric constants, brine volumes, surface wetness, density, salinity, grain and bubble size [*Paterson et al.*, 1991; *Tucker et al.*, 1992]. One of the most critical questions is to separate the contributions of surface and volume scattering in the SAR return signal. Whether surface scattering (which samples surface roughness) dominates over volume scattering depends sensitively on the material properties. In the case of low salinity ice at low temperatures, besides the snow/ice surface the ice/water surface and air bubbles in the ice volume also contribute to the SAR return [*Johansson and Askne*, 1987]. If, on the other hand, the overlying snow cover is wet, scatter of the air/snow surface also becomes important. *Ulander et al.* [1992] have shown that for Baltic sea ice scattering from the snow/ice interface generally dominates the ERS 1-SAR return. If one observes the

seasonal development in the SAR signature the relative importance of different scattering processes may change. *Winebrenner et al.* [1994] found a marked decrease in the backscatter of multiyear (MY) sea ice in the Beaufort Sea, as liquid water started to form in the snow layer at the onset of melt. However, for first year (FY) sea ice the onset of melt produced a much less conclusive change.

From the previous it is clear that it is very difficult to extract quantitative information on sea ice surface roughness from SAR returns. This is especially true for large-scale roughness. The direct identification of different ice types with the help of empirical SAR back scatter signatures seems more promising. To find the fractional coverage of different ice types over wide areas by remote sensing would be an important step towards an estimation of the heat balance in polar regions. *Fetterer et al.* [1994] were able to distinguish MY from FY ice in the Arctic but found a confusing variety of backscatter possibilities for new ice and open water. *Steffen and Heinrichs* [1994] proposed to use a combination of SAR and Landsat thematic mapper as a solution for this problem. With this combination they could distinguish ice free areas for calm wind conditions and they found two backscatter classes for nilas with and without frost flowers. However problems remain that the backscatter of gray and gray/white ice is not distinguishable from FY ice, and smooth and rough FY ice show essentially similar backscatter signatures. In Antarctica, MY ice, which is easier to evaluate with SAR, is rare and also probably morphologically different than in the Arctic. The predominance of FY ice and a variety of different forms of thin ice in combination with open water in Antarctica makes ice classification with SAR even more complicated. Another problem is the frequent occurrence of flooding in Antarctica [*Lange and Eicken*, 1991; *Adolphs*, 1] which also can obscure the source of backscatter.

The scope of the following investigation is a quantitative roughness study based on drilled profiles (consisting of 100 to 200 holes spaced at 1 m intervals) on individual sea ice floes. Given the finite sampling interval (which corresponds to a minimum wavelength

of 2 m) this is a study of macro-scale roughness with the upper wavelength limit given by the longest profile length. Three floe surfaces are of interest: The roughness of the ice underside, the ice surface roughness, which determines the accumulation pattern of the overlying snow layer, and the roughness of the snow surface itself. The roughnesses of the ice underside and the snow surface determine the drag coefficients for water and air; measures of the coupling strength of momentum and heat exchange between sea ice and the ocean, or sea ice and the atmosphere, respectively.

Most roughness studies so far have been done on Arctic sea ice using either laser profiling or submarine sonar data [*Wadhams*, 1980; *Hibler and LeSchack*, 1972; *Kozo and Tucker*, 1974]. To date, only a few investigations exist of the surface roughness characteristics of Antarctic sea ice have been done [*Andreas et al.*, 1993; *Lange and Eicken*, 1991; *Wadhams*, 1987]. The goal of the present investigation is to add to the sparse knowledge of Antarctic sea ice roughness in general, and to present roughness characteristics and variability for Antarctic regions (Amundsen/Bellingshausen and Ross Seas) other than the Weddell Sea.

The paper addresses the connection between roughness properties and ice type. First, a numerical cluster algorithm is applied to the measured sea ice floes in order to classify sea ice by thickness and roughness criteria. The ice groups identified by the cluster analysis are then examined in terms of roughness characteristics. In addition to the group analysis, individual profiles are studied with a new, two-dimensional space-scale approach. These results are compared to findings of a maximum entropy analysis on the same profiles. Finally, drag coefficients are derived using the previous results on roughness of the different profile surfaces. Central topics of this paper are how surface and roughness properties describe individual sea ice floes or whole ice groups and how a fuller characterization can be achieved by using different, complementary methods.

II.3 Data acquisition and limitations

The basis for this study are three distinct sets of drilling data which were collected during two trips of the research vessel *Nathaniel B. Palmer* (NBP) between May and September 1995. Figure II.1 shows three cruise tracks within the geographical area of the Ross, Amundsen and Bellingshausen Seas. The first cruise, NBP 95-3, took place in May and June and reached to 77.8°south and 179.5° west in the Ross Sea in the early winter of 1995 [*Jeffries and Adolphs*, in press]. Cruises two and three are two parts of the late winter expedition NBP 95-5 during which the Ross Sea was visited again in August 1995, another series of ice stations were occupied in the Bellingshausen and Amundsen Seas in September 1995.

As can be seen in Figure II.1 the cruise tracks were intended to be representative cuts through the study area; ice stations were nearly equally spaced with a typical distance of one degree of latitude (about 100 km) from one to the next. At each ice station, holes were drilled every meter along transects of 50 to 100 m in length. Snow thickness, ice thickness and freeboard were measured at each drilling location, which allowed the construction of a cross section of the floe along the transect. For each floe, one to three profiles were collected, which crossed each other and which were thus connected by the hole at the intersection. Only first year ice floes are considered in this study as the set of multiyear ice measurements was too small for meaningful statistical study. A total of 57 first year ice floes were sampled during all three cruises.

Each ice station was selected so as to be typical of floes in the area where the ship was operating on the particular day. However, bias was unavoidable. Very heavily deformed areas were not accessed representatively because the ship did not have enough power to break through very thick ice. A potentially greater bias occurred for very thin ice floes (mean thickness less than or equal to 30 cm) which were not sampled due to the dangers of working on thin ice.

Profile lines were laid out to collect a representative sample of the chosen floe. As a result each transect usually crossed at least one of the typical surface structures present on the particular floe, such as ridges or rafts. While this selection was intended to reflect the high amount of deformation observed in most of the study area [*Adolphs*, 1] it could have sometimes slightly underestimated the contribution of level ice without pronounced surface characteristics.

Each profile defines three surfaces of interest with respect to the zero or water line: the ice underside, the ice surface and the snow surface. Roughness characteristics of all three surfaces will be investigated in this study. Some limitations, imposed on the roughness calculations by the sampling method, have to be accounted for. Data resolution is limited by the 1m hole spacing which hides roughness features at shorter wavelengths. Similarly, the profile length puts an upper limit on roughness lengths. In order to cover the widest possible wavelength range, the longest possible profile was measured on each floe. This required that the profiles were not always straight lines but sometimes went at an angle along the axis of the floe.

II.4 Classification of floes into groups according to characteristic variables

For studies of the surface roughness properties of Antarctic sea ice, it has proven useful to classify the floes into appropriate groups first and then find common roughness characteristics for an ensemble of floes belonging to the same group [*Andreas et al.*, 1993; *Lange and Eicken*, 1991]. This approach is especially necessary for computing Fourier spectra because the spectra of single floes are far too noisy for a meaningful interpretation. By stacking floe data, characteristic wavelengths can be identified. *Lange and Eicken* [1991] performed a sea ice classification by subjectively grouping their floes in either deformed or undeformed categories. The goal of the following section is to find a similar grouping for the studied floes, however, with the help of an objective and hence reproducible classification scheme.

II.4.1 The choice of proper variables

Before a detailed classification procedure can be completed, an appropriate set of classifying variables has to be selected. The selection of the best variables to describe a floe is not easy. Thickness is intuitively the most important parameter for sea ice classification. However it is evident that not just thickness of snow and ice, but also some measure of deformation must play a role in characterizing floes. If all possible thickness and roughness variables were used, the resulting wealth of parameters would inevitably create a large number of indistinct ice groups. Hence, one has to concentrate on a few variables, judged to be most characteristic.

Short and long wave coefficients were defined in the following way as measures of surface roughness for each of the three profile surfaces. Given a matrix of normalized Gaussian functions

$$G_{ij} = \frac{1}{\sqrt{2\pi}\tilde{n}} \exp\left[\frac{(i-j)^2}{2\tilde{n}^2}\right],$$

with $\tilde{n} = \rho/\Delta x$, a unitless measure of distance defined as the quotient of the gaussian width ρ and the spacing $\Delta x = 1\ m$, a smoothed profile $\tilde{f}_i$ can be obtained from the original profile surface f_j by

$$\tilde{f}_i = \sum_j G_{ij} f_j \quad . \tag{1}$$

The standard deviation of $\tilde{f}_i$ is defined as the long wave coefficient and the standard deviation of $\left(f_i - \tilde{f}_i\right)$ shall be the corresponding short wave coefficient. The effect of this gaussian smoothing procedure is documented in Figure II.2 which shows is the underside of an ice profile, sampled at Julian Day 217 in the Ross Sea. The dotted line shows the ice underside profile as the result of smoothing with $\tilde{n}$=1.0, which was chosen for the calculation of the short wave coefficient. The dashed line shows the same ice underside

after a smoothing procedure with $\tilde{n}$=2.5, which was the chosen smoothing width for obtaining the long wave coefficient.

Sea ice floes were clustered with regard to a set of thickness variables (of ice, snow, freeboard) and roughness variables (such as long and short wave coeffients for the ice underside, ice surface and snow surface). Various combinations of variables and different cluster algorithms were tried. Non-redundant minimum sets of variables generally showed best results. Ice thickness proved to be the most crucial thickness variable, while short and long wave coefficients of the ice underside seemed to be the most distinct measures of roughness. Any addition/exchange of other thickness or roughness parameters made the results of the cluster algorithms less conclusive, creating too many and/or not significantly distinct ice groups.

II.4.2 The choice of the cluster method

There are two fundamentally different kinds of cluster algorithms to choose from: the hierarchical method and the partitioning method [*Kaufman and Rousseeuw*, 1990]. The hierarchical method starts out with as many clusters as objects (= ice floes) at step zero. At any successive step euclidean distances are computed between these objects according to a chosen linkage or amalgamation rule. Objects are then linked to clusters according to their mutual distances. The result is a hierarchical tree which ideally contains a clear structure (i.e. a few distinct branches or clusters). In contrast, the partitioning method is applied if one has already a hypothesis concerning the number of clusters. A typical partitioning algorithm, such as the k-means algorithm, produces exactly k different clusters of greatest possible distinction. The main disadvantage of the hierarchical method is its inability to correct erroneous decisions, whereas a drawback of the k-means algorithm is its possible effect of imposing a false structure on the set of objects.

For the hierarchical tree algorithm the Wards linkage rule was selected, which is widely used and generally efficient [*Romesburg*, 1984]. In each step it calculates the

hypothetical increase of E, the sum of cluster variances for all posssible mergers of two clusters. The merger that produces the minimum increase of E is then actually carried out.

For the partitioning method the k-means clustering algorithm was chosen which minimizes (in the space of the cluster variables) the average Euclidean distance of each cluster member (= ice floe) to the respective cluster center. "Bad" cluster members are identified in this scheme as being very distant from their cluster center but also not belonging to other clusters because they are even farther away from the centers of alternative clusters. Examples of both cluster methods have been applied to the set of all sea ice floes.

II.4.3 Presentation of three ice groups

Each floe was represented by its mean ice thickness, its short wave coefficient and its long wave coefficient for the ice underside. This set of three variables was used as input to the cluster algorithms described in section 3.2. In order not to overrate the importance of one of the parameters inappropriately, the variables were standardized for each cruise to mean zero and standard deviation one [*Romesburg*, 1984].

Both cluster schemes, the hierarchical algorithm as well as the k-means cluster routine were first applied separately to the sea ice floes of each cruise. This analysis showed that a successful classification also depends on the number of input floes. The early winter Ross Sea cruise with its 29 sampled floes clustered best, while the two late winter sets with 14 floes each formed less distinct clusters. The resultant tree diagram of the early winter cruise is shown in Figure II.3. Starting with all the input floes as separate clusters more and more floes and subclusters amalgamate to larger clusters with each step. Just below linkage distance 10 (euclidean distance, unitless) three distinct clusters have formed which were selected as ice groups. The outcome of a k-means algorithm with k equal to three produced identical partitions, which independently confirms the inherent group structure of the set of ice floes.

The same grouping within the floes of the early winter Ross Sea was still conserved when all 57 floes of all cruises were clustered together. As in Figure II.3, the result was a picture of three visibly distinct ice groups which could be classified as undeformed, medium deformed and strongly deformed ice by visual inspection of the respective floes. Also, it should be mentioned that in this definition for the three ice groups deformation is defined as rafting and ridging between ice sheets. Hence, it does not include rafting events between pancake or small cake ice floes. The k-means algorithm again found the same classification as in Figure II.3, except for two floes which were grouped in group 2 and 3 in the tree diagram and classified as belonging to group 1 and 2 by the partitioning method. Figure II.4 shows a graph of the standardized mean values for the cluster variables. Each of the three ice groups is represented by a distinct triple of values. Group 1 (undeformed ice) has below average values of ice thickness and the lowest, although less distinctly, values of long and short wave roughness. Group 2 (medium deformed ice) shows a visibly higher value in ice thickness and long wave roughness than group 1 and a similar order of magnitude for the short wave roughness coefficient. Above average values in all three variables are the characteristic attribute of group 3 (strongly deformed ice).

In summary, the presented cluster algorithm could classify the ice floes into the three ice groups at least as well as a subjective decision would. Difficulties in finding the appropriate group for a given floe occurred in cases where the floe showed almost equal shares of properties of two groups. A subjective decision would have also been difficult in those cases. An example for such a case are two late winter Ross Sea floes which are smooth but very thick (mean thickness > 1m). Biased by their thickness these floes were sorted into medium deformed ice while it could be argued that they belong to group 1. Another example are two medium thick but extremely rough ice floes of the late winter Ross Sea which were classified by the hierachical algorithm into group 3 because of their roughness while it could be reasoned that they belong to group 2 because of their thickness. A last example are two cases of floes, each consisting visibly of two pieces of

level ice with different mean thicknesses. While they could theoretically be classified as undeformed, it is not unreasonable to group them with the medium-deformed floes as the the algorithm does. All in all it can be concluded that the presented classification scheme satisfactorily fulfills the task of classifying the ice floes into meaningful groups. With a performance similar in quality to that of a subjective classification, the objective cluster scheme was preferred here as it has the advantage of being reproducible.

The medium deformed group (group 2) contains 28 floes, significantly more than each of the other two. This might reveal a bias introduced by the profile selection rule which favored the sampling of surface deformation features on floes. 19 floes were classified as undeformed (group 1) and 10 floes as strongly deformed (group 3). The early winter Ross Sea cruise had a somewhat higher number in group 1 floes as compared to the two late winter cruises, which in contrast, showed higher percentages of floes belonging to the medium or strongly deformed groups. This may reflect the build up of deformation during the seasonal evolution of the pack ice. The geographical distribution for the member floes of all three ice groups can be seen in Figure II.5. There is a slight tendency towards more frequent deformation with increasing latitude but even at the highest latitudes there are several group 1 floes, and group 3 floes are found at low latitudes. In summary, there is no strong dependency between longitude and latitude and the degree to which ice is deformed. Processes, like convergence/divergence of the ice motion, stage of ice development, and atmospheric and oceanographic conditions, that together determine whether a floe is undeformed, deformed or strongly deformed, do not appear to relate to geographic location in a simple way. In addition it should be noted that the Antarctic pack is quite mobile, a fact that would tend to blur any correlations between location and deformation, even if they were to exist.

II.5 Roughness measures

There are various ways to define and quantify the roughness of a surface. Each way emphasizes a particular aspect of the general picture and care has to be taken when the results from different roughness criteria are compared. There are two "classical" approaches to measuring surface roughness: the variance as a measure of amplitude roughness, and the Fourier spectrum analysis as a roughness distribution for a range of wavelengths. The findings of both analyses will be compared to the amplitudes, structure lengths and characteristic wavelengths found with a semivariogram method. In order to find characteristic roughness properties for the three ice groups, comparisons will be carried out between the ice groups and also between single representative profiles of each group.

II.5.1 Variance as a measure of amplitude roughness

The roughness of a surface can be quantified as the variance of its elevation around its mean value [*Andreas et al.*, 1993]. Defining the elevation of a line of N points at any point j with z_{xj} (with x being either s (snow surface), i (ice surface), or u (ice underside)) the roughness variance is defined as sum of the squares of deviations from its mean value $\langle z_x \rangle$,

$$\sigma_x^2 = \frac{1}{N}\sum_{j=1}^{N}\left(z_{xj} - \langle z_x \rangle\right)^2 . \qquad (2)$$

The variance, or the square root of the standard deviation, σ_x, is a measure of the deviation of vertical surface structures. σ_x can therefore be used as a measure of the roughness of the surface amplitudes (vertical scale) on a given horizontal scale. The resultant values for σ_i and σ_u for all profiles of each ice group are graphed versus the standard deviation of the snow surface (σ_s) in Figure II.6. As found by *Andreas et al.* [1993], the standard deviation of the ice underside (Figure II.6 b) can be 2 to 6 times as large as σ_i for the two groups of deformed ice. Also in agreement with their findings is

that σ_i is always below 10 cm and σ_s is rarely above 20 cm for undeformed floes (group 1), while the corresponding standard deviations for deformed floes (group 2 and 3) are mostly above these values. σ_s values range between 0 and 20 cm, as can be seen in Figure II.6a; they are generally greater than the corresponding σ_i values, which is in contrast to the finding of *Andreas et al.* [1993]. The snow surface standard deviation can be up to twice as large as the standard deviation of the ice surface, especially for the two deformed groups (group 2 and 3) as Figure II.6a shows.

II.5.2 Three profiles (and their roughness characteristics) as representatives for the ice groups

Figure II.7 shows three profiles which were selected as representatives of the ice groups. Figure II.7a shows a relatively thin, undeformed floe (group 1) which was sampled on Julian Day 231 in the late winter Ross Sea. It is quite uniform in appearance, has no trace of deformation but nevertheless has pronounced ice underside roughness. This floe was sampled at 65° south and 157° west and is a typical young ice edge floe with fairly regular ice underside fluctuations revealing its underlying pancake structure. The floe seen in Figure II.7b is a moderately thick, medium-deformed floe (group 2) sampled on Julian Day 136 in the early winter Ross Sea. It is dominated by low ridges of long wavelength. Interestingly, the small scale roughness of its ice underside is less pronounced than that of the group 1 floe in Figure II.7a. Figure II.7c shows a typical thick and strongly deformed floe (group 3) of the late winter Amundsen Sea, sampled on Julian Day 249. The inhomogenity of this floe is obvious and its roughness seems to be especially pronounced at the ice underside. These floes will serve as representative samples of the three ice groups in the following discussion and analysis.

II.5.3 Fourier (roughness) spectra of the three ice groups

From the profiles in Figure II.7 it is apparent why it is useful to calculate the contributions of roughness at different wavelengths instead of using just a single

roughness measure, such as variance. The ice underside in Figure II.7a clearly has more short wave roughness than the profile in Figure II.7b where the roughness contribution is mostly from long wavelengths. To gather information about the range and the weight of wavelengths which determine the roughness of a particular surface profile with elevation $z(x)$, a Fourier power spectrum $\Phi(k)$ for the wavenumber $k=2\pi/\lambda$ (and wavelength λ) is computed. The autocorrelation function is first calculated as

$$C(h) = \frac{1}{l}\int_0^l (z(x)-\mu)(z(x+h)-\mu)dx, \qquad (3)$$

where $\mu = \langle z(x) \rangle$ is the mean value of the surface elevation, l is the total length of the profile and h is the spatial lag. The power spectrum $\Phi(k)$ can then be expressed as the Fourier transform of (3),

$$\Phi(k) = \int_{-\infty}^{+\infty} C(h)\cos(kh)dh. \qquad (4)$$

Since the power or energy spectrum $\Phi(k)$ denotes the energy contribution of the signal at wavenumber k, one can obtain the total energy can be calculated as the integral over all wave numbers. In the spatial domain x the total energy is simply given by the variance σ^2 (equation 2) which implies the equality,

$$\sigma^2 = \int_0^{\infty} \Phi(k)dk. \qquad (5)$$

As the profile surfaces are sampled at discrete points and have finite lengths, integrals are replaced by sums when the actual calculations are carried out. Sums over k extend from the smallest wavenumber, $k=2\pi/l$ for a profile length l, to the longest wavenumber, $k=2\pi/(2\Delta x)$ for a sampling interval of Δx (1 m). To minimize the influence of boundary effects on the spectra, due to the limited signal length, a window function [*Kaimal and Kristensen*, 1991; *Hibler and LeSchack*, 1972; *Andreas et al.*, 1993] was applied to each profile. Spectra of single profiles were then computed but, due to the inherent properties

of the Fourier transform, they were far too noisy for direct interpretation. In analogy to *Andreas et al.*[1993] an averaged, non-dimensionalized spectrum of the form

$$k\phi_x(k)/\sigma^2 = \frac{k}{n_x}\sum_{i=1}^{n_x}\phi_{xi}(k)/\sigma_{xi}^2 \qquad (6)$$

was computed for each ice group. The summation includes all spectra n_x of a surface with x denoting either the snow, (s), ice, (i) or ice underside surface (u) within the selected ice group. Each spectrum Φ_{xi} is non-dimensionalized by its variance σ_{xi}^2 and the wavenumber k. The factor σ^2 on the right side of equation 6 indicates the non-dimensional character of the averaged spectrum.

The averaged surface spectra computed for the three surfaces are shown in Figure II.8a (snow surface), b (ice surface) and c (ice underside) as log-log graphs. Error bars show the 95% confidence intervals calculated with the appropriate chi-squared probability distribution. Despite averaging, these error bars are large enough that none of the local peaks at specific wavenumbers k can be considered significant. Therefore, only the general shape and slope of the spectra in Figure II.8 are of use. For all curves in Figure II.8 wavenumbers range between 0.1 and 3 rad m^{-1} corresponding to wavelengths between 2 and 60m. Shape and slope of the spectral curves are different for the different surfaces and also, less distinctly, for the same surfaces of different ice groups. Spectra for the ice underside and snow surfaces (Figure II.8a,c) slope down towards higher wavenumbers (short wavelengths), corresponding to an energy concentration at low wavenumbers (long wavelengths). In contrast, ice surface spectra (Figure II.8b) remain constant or even increase with increasing wavenumber k (decreasing wavelength). This tendency of shape and slope in the spectra is broadly similar to what was observed by *Andreas et al.*[1993] for their groups of first year ice.

The range of wavelengths (2-60m) is a direct result of the limited resolution and profile lengths. Incidentally, this study is comparable to that of *Andreas et al.*[1993] for the Weddell Sea, because of the similarity of the profile lengths and the identical spacing

of individual measurements (1 m). A drawback of the relatively short profile lengths is the exclusion of potential peaks in the spectra at long wavelengths. Sonar and laser profiles of Arctic sea ice, whose profiles are much longer than those of existing Antarctic sets show significant spectral peaks for long wavelengths. *Banke and Smith* [1973], for instance, suggest a spectral peak for the Arctic snow surface at λ equal to 200 m while *Hibler* [1975] proposes 100 m. *Kozo and Tucker* [1974] suggest a wavelength of 200 m as spectral peak for the ice underside. It would be interesting to see whether Antarctic sea ice shows similar characteristic peaks at low wave numbers, making the acquisition of longer profiles desirable in the future. The ice surface spectra in Figure II.8b reveal a significant increase in spectral intensity for wavenumbers greater than 1 rad m^{-1} (wavelengths smaller than 6-7 m). For the Weddell Sea, *Andreas et al.* [1993] speculated that this signature in the ice surface spectrum might reflect a particular ice formation process, which is typical for the Antarctic: the so-called "pancake cycle" [*Ackley et al.*, 1987; *Wadhams et al.*, 1987; *Lange et al.*, 1989]. Pancakes, with diameters of several centimeters to several meters, raft and consolidate by interstitial freezing into an ice surface whose roughness would be dominated by typical pancake dimensions; this would correspond to the pronounced increase in spectral energy at wavelengths smaller than 7 m. At intermediate wavelengths, *Ackley et al.*[1976] found a spectral peak for Arctic multiyear ice at about 30 m (k=0.2 rad m^{-1}), which was not found in the ice surface spectra of Figure II.8b. Ackley's 30 m peak is probably caused by the frequent occurrence of summer melt ponds in the Arctic [*Andreas and Ackley*, 1982], which also has a smoothing effect on the ice surface at smaller wavelengths. In the Antarctic, melting on the ice surface is rare; however, widespread flooding of Antarctic sea ice [*Ackley et al.*, 1990, *Eicken et al.*, 1994] could, to some extent, analogously diminish high wavenumber roughness.

II.5.4 Slopes and fractal dimensions from the Fourier spectra

In order to quantify the slope of the power spectra, a least squares regression line was fitted to the log-log plots of $\phi(k)$ versus k; the slope of the regression line is the exponential decay parameter γ of an assumed power law dependence

$$\phi(k) \propto k^{-\gamma} \tag{7}$$

of the spectra $\phi(k)$. The resultant γ values are presented in Table II.1; $\gamma > 1$ for the snow and ice underside surfaces and $\gamma < 1$ for the ice surface. As a consequence, the snow and ice underside surfaces (but not the upper ice surface) can be interpreted as fractional Brownian motion or red noise [*Wornell*, 1996]. For red noise, a fractal (Hausdorff) dimension

$$D = \frac{5-\gamma}{2} \tag{8}$$

can be calculated, provided $3 > \gamma > 1$, which is the case here. These so-called $1/f$ processes (since the power spectrum fits $1/f^{\gamma}$) with fractal behavior occur frequently within natural phenomena, such as in studies of textural variations in natural topography [*Turcotte*, 1993; *Barton and LaPointe*, 1995].

The fractal dimension D is a useful quantitative measure for the roughness and topography of sea ice. Values of D derived from the power law behavior of the Fourier spectra are given in Table II.1 for both the snow and ice underside surface. It can be seen from Table II.1 that fractal dimensions are generally higher (and γ values correspondingly lower) for the ice underside than for the snow surface. This finding is in contrast to *Andreas et al.*[1993] who suggested larger γ (hence lower D) for the ice underside than for snow surface. The range of γ for the ice underside (between 1.2 and 1.6) is very similar to the range found by *Andreas et al.* [1993]; the range of γ for the snow surface (Table II.1) however exceeds the range found by *Andreas et al.* [1993].

The fractal dimension D is high in group 1 (undeformed ice) for both snow surface and ice underside while it is smaller in group 2 (medium deformed ice) for both surfaces.

For groups 2 and 3 (strongly deformed ice) D is similar for the snow surface but the D for the ice underside is higher in group 3 than in group 2. Since a high fractal dimension means a small γ and hence a shallower slope of the spectrum towards higher wavenumbers (smaller wavelengths), a large D describes a high contribution of short wavelength roughness. The fractal dimension can therefore be applied as a measure for short wavelength roughness of the corresponding surface.

All fractal dimensions given in Table II.1 for the three ice groups range between 1.6 and 2.0. Values found for the Arctic seem to be generally lower. *Bishop and Chellis* [1989] found a range of 1.2 to 1.6, *Key and McLaren* [1991] found 1.4 and 1.6 for the ice underside of Arctic first and multiyear ice respectively and *Wadhams and Davis* [1994] found values between 1.4 and 1.7 dependent on the geographic region. *Hibler* [1975] and *Kozo and Tucker* [1974] find γ values of 2.2 and 2.3 corresponding to fractal dimensions of 1.4 or 1.35 respectively. *Rothrock and Thorndike* [1980] find γ equal to 3 (hence $D=1$) for the obviously rather smooth underside of sea ice in the Beaufort Sea.

It can be concluded that:

(1) A comparison of fractal dimensions from the two polar regions shows that Antarctic sea ice has a higher short wavelength roughness than Arctic sea ice, which has more long wavelength roughness. This finding further confirms the results of past investigations [*Andreas et al*, 1993; *Lytle and Ackley*, 1991].

(2) The ice underside has more short wave roughness than the snow surface. However, the ice surface has the highest contribution in the shorter wavelengths of all three surfaces. The ice surface variance (which is the integral over the spectrum, section 4.3) is similar to or lower than the variance of the snow surface.

(3) Fractal dimensions or short wave roughness of the snow surface decrease with increasing deformation as seen between group 1 and 2 and becomes almost constant between group 2 and 3. Short wave roughness of the ice underside is lowest for medium

deformed ice (group 3) and higher for undeformed and strongly deformed ice (group 1 and 3).

II.5.5 Structure lengths and amplitudes, characteristic wavelength and fractal dimensions from semivariograms

The semivariogram method, another tool from spatial statistics [*Isaaks and Srivastava*, 1989; *Robert and Richards*, 1988; *Oliver and Webster*, 1986], is an elegant way to identify structure lengths and amplitudes as well as characteristic wavelengths for the three surfaces of the sea ice profiles. Given a profile surface, z, the semivariogram $\gamma(h)$ for a lag distance h is defined by

$$\gamma(h) = \frac{1}{2(N-h)} \sum_{i=1}^{N-h} \left[z(x_i + h) - z(x_i) \right]^2 , \qquad (9)$$

where N is the number of data points and the summation runs over all sample locations x_i that have a neighbor at distance h. Equation 9 shows that the semivariogram depends on spatial correlations, with $\gamma(h)$ low for those h where surface structures are strongly correlated and high where they are uncorrelated. The semivariogram bears some similarity to the autocorrelation function, $C(h)$, and for second order stationary processes $\gamma(h)$ becomes

$$\gamma(h) = \sigma^2 \left[1 - C(h) \right] , \qquad (10)$$

where σ^2 is the variance of z.

The semivariogram is usually zero at $h = 0$ and increases thereafter with increasing h. If a maximum or sill is reached at a certain distance h, this marks the decorrelation or structural length R. As $C(h)$ is zero at this h, the semivariogram is equal to the variance which determines the structural amplitude $A=\sigma$ at this point. If $\gamma(h)$ shows periodic, fine scale variations at larger h, a small scale characteristic wavelength λ can also be determined. Semivariograms were computed for each profile and the parameters A, R and

λ were estimated via visual inspection. Table II.2 presents the mean values of the parameters for each of the three profile surfaces of all ice groups.

Similar to the Fourier spectra, semivariograms can be used to calculate a Hausdorff dimension D (section 4.4) [*McBratney and Webster*, 1986]. For this purpose, a power law relation of the form

$$\gamma(h) = \frac{1}{2}h^{\theta} \tag{11}$$

is fitted to the semivariogram and a fractal or Haussdorff dimension is calculated according to

$$D = 2 - \theta/2. \tag{12}$$

This approach is used to determine fractal dimensions for the representative single profiles given in Figure II.7. Mean values of D for all floes belonging to one ice group are also calculated and are compared to the mean dimensions obtained via the Fourier spectra.

The fractal dimensions obtained with semivariograms for the representative floes of Figure II.7 as well as for the ice groups are listed in Table II.1. As shown in Table II.2 almost all parameters increase with increasing deformation (group 1 to group 3). Structural amplitudes A vary distinctly between the different surfaces. The amplitude of the ice surface is approximately two times larger than for the snow surface and about five times larger than for the ice underside. Structure lengths R and characteristic wavelengths λ are similar in range for the snow and ice underside surfaces, but somewhat smaller for the ice surface.

II.5.6 Comparison between roughness measures

The observed inter-surface variations of the structural amplitude, A, derived from the semivariograms, compare well with those of the standard deviation, σ, previously presented in section 4.1. The range of σ_4 (ice underside) in Figure II.6 was about five

times that of σ_i for the ice surface. This is in agreement with the relation of ice underside and ice surface structural amplitudes in Table II.2. Similarly, σ_s was up to two times larger than σ_i which again compares well to the relation between the structural amplitudes given for the snow and ice surface. The fact that the semivariogram structure length and characteristic wavelength are smallest for the ice surface agrees with the results of the Fourier spectra where the ice surface also showed the highest contributions to short wave roughness. However, while the semivariogram attributes similar structure lengths and characteristic wavelengths to the snow and ice underside surfaces (Table II.2), higher short wave roughness was suggested for the ice underside by the Fourier analysis of sections 4.3 and 4.4. Results from the semivariograms show that the rougher appearance of the ice underside is expressed solely by its higher structural amplitude with respect to the ice and snow surfaces. Between groups, the structure length of the ice underside is smallest for the strongly deformed group (group 3 in Table II.2).

In conclusion, two phenomena are found for the ice underside and the snow surface as compared to the ice surface: larger structural lengths and characteristic wavelengths λ on the one hand and larger structural amplitudes on the other hand. Larger structural amplitudes indicate larger amplitude roughness. But together with the simultaneous increase of the structure lengths and characteristic wavelengths, larger amplitudes can be interpreted as part of a smoothing action on the ice underside and the snow surface in contrast to the ice surface. A similar interpretation has been given by *Sturm et al.* [submitted] who reported a smoother snow surface in comparison to the underlying ice surface. The results of Table II.2 show further that structural amplitudes and lengths generally become larger with increasing deformation. This signifies a corresponding shift from short wave to long wave roughness in agreement with the results of the fractal dimension analysis presented in Table II.1. The only exception to this general trend is the reduction in the structure length of the ice underside from the medium deformed ice group 2 to the strongly deformed ice group 3. That this reduction in structure length (equivalent

to an increase in short wave roughness) is a real phenomenon is corroborated by a corresponding increase of the fractal dimension in Table II.1.

The fractal dimensions, D, obtained with the semivariograms (Table II.1) show trends similar to those obtained with the Fourier spectra of section 4.4. D for the snow surface becomes smaller with increasing deformation, from group 1 to group 3. D of the ice underside is at a minimum for group 2 and larger for both groups 1 and 3. This trend of fractal dimension is also shared by the representative profiles of Figure II.7. The snow and ice underside surfaces of the group 1 floe in Figure II.7a exhibit the highest small scale roughness, and also the largest D. For the snow surfaces, small scale roughness and D then decreases between the group 2 and 3 floes. In contrast, small scale roughness and D are smallest for the ice underside of the group 2 floe. These results also agree with a qualitative judgment of the profiles in Figure II.7. Apparent from Table II.1 is finally a close similarity between the two fractal dimensions for the group 1 floe while the difference between the two D's becomes larger, the older and more deformed the floe is.

II.6 Wavelets and Maximum entropy spectra

One major drawback of the Fourier spectrum is the loss of all spatial information in the signal that is inherent to a complete amplitude/ frequency representation. This drawback becomes a problem if the signal is not stationary in space, as is the case for a significant portion of the profiles of this study. By transforming a signal with wavelet functions into a two dimensional space-scale domain, characteristic structures can be identified at various scales and these structures can also be localized in space. By integrating the two-dimensional wavelet transform over the space dimension one obtains the wavelet variance which now only depends on scale. The wavelet variance can be used to reveal dominant structure lengths and results can be compared to those of the other space independent tools of the previous sections, like Fourier spectra and semivariograms. This wavelet approach will be carried out in the following two sections.

A further serious drawback to the Fourier spectra method is that individual profiles are difficult to study due to the inherent noisiness of the spectral amplitudes. This drawback is circumvented by other methods that provide qualitative but smoother spectral estimates. One such method is the maximum entropy approach which is presented in section 6.3.

II.6.1 Wavelets applied to snow and ice surfaces

A wavelet is a waveform of limited extension in either time or space with an average value of zero. The transformation of a signal $f(x)$ with a wavelet $\psi(a,b)$ is defined as

$$(W_\psi f)(a,b) = \frac{1}{\sqrt{|a|}} \int f(x)\psi\left(\frac{x-b}{a}\right)dx, \qquad (13)$$

with b being the translation parameter which shifts the wavelet through space and a being the scaling parameter. If the scale a is constant, the wavelet transform (WT) is very similar to a windowed Fourier transform (WFT). But unlike a WFT, the wavelet transform (WT) provides a mechanism for examining structures at different scales [*Kaiser*, 1994; *Meyer*, 1993]. Starting with a chosen wavelet at scale a = 1 (the so-called mother wavelet) variation of a creates a whole family of wavelets whose shape is compressed or stretched in order to cover different scales. The factor $1/\sqrt{|a|}$ guarantees that the energy (which is the spatial integral over the square of the wavelet) of each scaled wavelet will be equal to the energy of the mother wavelet (at a = 1). As mother wavelet for the following study, the so-called Mexican hat wavelet

$$\psi(x) = (1 - 16x^2)\exp(-8x^2)$$

was chosen. This wavelet function $\psi(x)$ is identical to the second-order derivative of a Gaussian bell.

Figure II.9 shows the space(b)-scale(a) representation for the snow surface of the group 2 profile of Figure II.7b. The result is a continuous, two-dimensional picture of wavelet coefficients $c(a,b) = WV_f(a,b)$ where the brightness at each point (a,b) is related to

the magnitude of $c(a,b)$ and hence to the degree of resemblance between the wavelet and the signal at this space-scale point. In Figure II.9 there is a bright vertical band in the wavelet coefficients at a spatial scale b of roughly 85 m which corresponds to the local trough in the snow surface in the center of the shallow ridge of the profile in Figure II.7b. The scale parameter (a) has horizontal brightness maxima at scales a of about 7 and 25 m. These maxima indicate a high similarity of the signal with the wavelet at these scales. The two scales (7 and 25 m) can therefore be interpreted as dominant scales or structure lengths in the profile in Figure II.7b. The typical brightness pattern in the wavelet coefficients on one scale in Figure II.9 are seen to repeat similarly on other scales. This shows that the correlation between the signal and the wavelet is similar on different scales, thus qualitatively verifying the fractal nature of the snow and ice profiles, which was already shown in section 4.

II.6.2 Wavelet variance for single profiles

The wavelet variance WV_f for the signal f is defined as

$$WV_f(a) = \frac{1}{x_2(a) - x_1(a)} \int_{x_1(a)}^{x_2(a)} \left[(W_\psi f)(a,b) \right]^2 db, \qquad (14)$$

with $x_1(a)$ and $x_2(a)$ being the lower and upper limits of the spatial range, b [*Li and Loehle*, 1995]. So defined, the wavelet variance is a measure for the average energy content of all spatial wavelet coefficients for a given scale a. Since the energy is conserved by a wavelet transformation, the area under the wavelet variance is equal to the signal energy. Local peaks in the wavelet variance therefore indicate energy maxima and the respective scales where they occur can be interpreted as dominant structure lengths in the signal.

Figure II.10a and b show the wavelet variance of the snow surface and the ice underside for the group 2 floe (Figure II.7b). Two maxima are seen for the snow surface at structure lengths 7 m and 25 m, which evidently agrees with the two brightness maxima

observed in Figure II.9. The wavelet variance of the ice underside shows only one maximum at a structure length of about 27 m.

The wavelet variances of the ice underside for the group 1 floe (Figure II.7a) and the group 3 floe (Figure II.7c) are shown in Figure II.11 a and b. For the group 1 floe, there is a local maximum at about 5-7 m and another at about 2 m; for the group 3 floe the wavelet variance shows a plateau at about 6 m and increases steadily thereafter.

The dotted curves in Figure II.11 a and b show the wavelet variances of the first part (1) and the second part (2) of the profiles, which were divided at distance 80 m (group 1 floe) and 85 m (group 3 floe), respectively. For the group 3 floe, a local maximum can be detected at 10 m only for the first part of the profile. The wavelet variance of the second part of the profile lacks the 10 m maximum and shows more contribution of longer structure lengths. This is in agreement with the divide in the profile at about 85 m (Figure II.7c). For the group 1 floe, the maxima of the all profile variance show up in the variance of second profile part but not for the first part. The latter finding was also in agreement with the space (b)-scale (a) representation of this profile, where two different zones could be seen with brightness maxima showing up at a scale of 5-7 m only in the second part (80-150 m) of the profile. The strength of the wavelet method is thus illustrated by this last example as it provides a way to divide a profile which looks quite uniform upon quick observation (Figure II.7a) into two different spatial zones. In this way the use of wavelets opens the possibility of subclassifying floes where floe segments, identified by the WT, could possibly be fed again into a cluster algorithm.

II.6.3 Maximum entropy for single profiles

For the maximum entropy approach [*Therrien*, 1992], the spectral density of a signal f is computed by assuming the signal as a linear Markov process of order M. This means that each of the N signal points depends linearly on its M nearest neighbors according to

$$\{f\}_i = \sum_{j=(i-M)}^{i-1} [a_j f_{i-j}] + \varepsilon_i \qquad , \quad \forall_{i=M+1..N-M} \tag{15}$$

The error term ε_i is minimized in a least square sense by varying the coefficients a_i of the linear approximation. The advantage of this method is that the Markov process can be continued beyond the data length. In this way windowing effects which contribute to the high noise level of Fourier spectra are reduced and a much smoother spectral estimate is obtained. Typical frequencies are discernible more clearly and the fine resolution of nearby frequencies is enhanced. However, there is the disadvantage that the relative heights of individual peaks do not correspond to their respective contributions to the true power spectrum.

Maximum entropy spectral densities for the group 2 floe are shown in Figure II.10c and d. For the snow surface, one large maximum can be discerned at a wavelength of 25 m and several smaller ones at lower wavelengths. For the ice underside there are spectral maxima at about 27-30 m, at 15 m and at several lower peaks at small wavelengths. The spectral density for the ice underside of the group 1 floe (Figure II.11c) features one maximum at around 7 m, while at about 25 m it climbs to a plateau. Conversely, for the group 3 floe no high spectral maxima are seen (Figure II.11d); besides insignificant peaks at small wavelengths the spectral curve ascends steadily with wavelength.

In comparison with the results of the wavelet variance (section 5.2), the maximum entropy spectra essentially reproduce, as distinct maxima, the dominant structure lengths found with the former method. For example, the structure lengths found with the wavelet variance method for the group 2 floe, at 25 m for its snow surface and at 27 m for its ice underside, show up as distinct maxima in the maximum entropy spectra of Figure II.10. Similarly, the peak in the maximum entropy spectrum of the group 1 floe at about 7 m (Figure II.11c) corresponds to the dominant structure length derived with the wavelet variance and seen in Figure II.11a. Finally, the non-stationary character of the wavelet variance for the group 3 floe (Figure II.11b) is also reflected in the spectrum of Figure

II.11d. The maximum entropy approach also shows several additional peaks compared to the wavelet variance, especially at short wavelengths. For instance, several additional maxima were found by the maximum entropy method for the snow surface of the group 2 floe in Figure II.10c. These additional maxima are located in the vicinity of the second structure length at 7 m which was also found by the wavelet variance (Figure II.10a). Similarly, for the ice underside of the same floe other smaller wavelengths peaks were found near to the dominant structure length of 27 m (Figure II.10d). How much of this additional structure is real or an artifact of a too high order M, chosen for the maximum entropy method, has to be decided from case to case.

II.7 Drag coefficients for snow, ice and ice underside surfaces

Profile surface characteristics such as typical wavelengths and amplitudes were determined in the preceding sections. These surface characteristics can be used to calculate water and air drag coefficients which influence the nature of energy transfer processes at the interfaces of a sea ice profile. From the air drag coefficient C_D, which is the transfer coefficient of momentum at the air-sea ice interface, the latent and sensible heat transfer coefficients, C_H and C_E can be derived [*Andreas*, 1987; *Andreas and Murphy*, 1986]. In determining the turbulent heat exchange, C_D plays an important role in energy balance models.

In order to use C_D as a comparable measure for the surface drag it is usually standardized to its neutral stable value at 10 m height. This convention will be followed here. The usual way to determine drag coefficients is by wind profile measurements [*Banke et al.*, 1980; *Allison and Akerman*, 1980; *Andreas and Makshtas*, 1985]. But *Banke et al.*[1980] have also shown a relationship between drag coefficient and surface characteristics. Using the same spacing (1 m) and similar profile lengths as used in this study, they defined a surface elevation ζ as

$$\zeta^2 = \int_{k_0}^{k_{max}} \phi(k)dk, \qquad (16)$$

which is the integral over the spectrum $\phi(k)$ with the lower limit k_0 equal to 0.5 rad m^{-1}, corresponding to a wavelength of about 13 m. The upper limit is defined by the smallest wavelength, which is 2 m (k_{max}=3 rad m^{-1}) for a sampling distance of 1 m. For this surface elevation ζ *Banke et al.*[1980] found the following empirical relationship to C_D

$$10^3 C_D = 1.10 + 0.072\zeta \quad , \qquad (17)$$

with a correlation coefficient r =*0.9*. Another relation connects the root mean square (rms) of the surface slopes (S_{rms}) to the drag coefficient,

$$10^3 C_D = 1.17 + 7.09 S_{rms} \quad , \qquad (18)$$

with *r=0.82*. Equation 17 is preferred here for its slightly higher correlation. Note, from equation 16 that ζ^2 is simply the variance contribution between the wavelengths of 2 and 13 m (see equation 5). A comparison between ζ^2 and σ^2 for each profile showed a strongly linear relation between the two with ζ^2 being lower in value since it represents only part of the integral. Drag coefficients are consequently linked to the variance and hence to the measure of amplitude roughness (section 4.1).

Using equations 16 and 17 the drag coefficients for each surface profile were computed. Figure II.12 shows a histogram of the air drag coefficients for all three ice groups. As can be seen one finds a range of 1.1-1.5 $\times$ 10^{-3} for undeformed ice (group 1) and values between 1.2-1.7 $\times$ 10^{-3} for medium to strongly deformed ice (group 2 and group 3). Drag coefficients were also computed for the ice surface and the ice underside. Table II.3 contains mean drag coefficients per ice group for all three surfaces. The drag for all three surfaces generally increases with increasing deformation (group 1 to group 3). The relationship of ice surface and underside drag compared to the air drag of the snow surface is shown in Figure II.13. Drag coefficients of the ice underside are almost always distinctly higher than snow surface drag (Figure II.13b). This difference is more pronounced for strongly deformed ice (group 3). Ice and snow surface drag are generally

of the same order of magnitude. If all ice groups (1-3) are combined, ice surface drag is generally lower than snow surface drag (Figure II.13a), although a few rare exceptions occur.

Drag coefficients computed with the alternative equation 18 (slopes) are almost linearly related to the drag coefficients calculated with the Fourier spectra; and their values were systematically higher by about $0.1\text{-}0.2 \times 10^{-3}$. This result is in agreement with *Lange and Eicken* [1991] who used equation 18 and calculated slightly higher drag coefficients for the Weddell Sea than *Andreas et al.*[1993] who used equation 17.

It should be noted that the calculated drag coefficients represent only the local surface drag or frictional stress. By having only wavelengths smaller than 13 m contribute to C_D , *Banke et al.*[1973,1980] assumed that the small scale roughness dominates the local surface drag. The same assumption underlies the work of *Andreas* [1995]. Area-averaged values for the drag coefficients, measured by airborne laser profilometers, are, on the other hand, usually greater than these "local" drag coefficients [*Overland*, 1985]. This discrepancy is caused by the influence of large scale roughness, such as form drag of ridges, on the area averaged drag coefficient. *Banke*[1980], *Arya* [1973b,1975] and *Joffre* [1983] estimated the contribution of form drag as ranging from 5 to 30 % of the total drag for the Arctic. For the Antarctic, it can be argued that ridge heights are often lower and buried underneath the snow so that they should be contained in frictional surface stress measurements [*Arya*, 1973a]. However *Dierken* [1995] found that drag could be considerable in the Weddell Sea region of the Antarctic.

In conclusion, it is found here that calculated air drag coefficients are very similar to those given by *Andreas et al.* [1993] for undeformed and deformed Weddell sea ice. They further compare well with values derived from vertical wind profiles measured in East Antarctica [*Allison and Akerman*, 1980] and to measurements by *Andreas and Makshtas* [1985] and *Wamser and Martinson* [1993] in the Weddell Sea. Water drag coefficients which are presented here are comparable to those found by *Lange and Eicken* [1991] if

differences in the methods of calculation are accounted for. Compared to the Antarctic drag coefficients discussed here, Arctic air drag values are generally higher [*Guest and Davidson*, 1987, 1991; *Anderson*, 1987]. However, for both, the Arctic and Antarctic regions, drag coefficients are found to increase with increasing deformation.

II.8 Discussion and conclusions

In this study a combination of methods from classical and modern spatial statistics was applied to a data set of Antarctic first year sea ice profiles to reveal their roughness characteristics and variability. The results of the different methods were either similar or complementary and were useful when applied to single profiles as well as to ice groups.

First, a numeric group classification scheme was applied to the data. This objective cluster scheme performed at least as well as subjective methods but has the advantage of being reproducible and unbiased. Three characteristic clusters were found. They correspond to ice groups of undeformed, medium deformed and strongly deformed floes.

The variance (σ^2), computed for three profile surfaces (snow surface, ice surface and ice underside) was used as a measure of (vertical) amplitude roughness. The range of σ for the snow surface and ice surface were similar: σ of the snow surface could be up to twice as large as σ of the ice surface, especially for deformed ice (groups 2 and 3), while σ of the ice underside was two to five times as large as σ of the snow surface; the difference was also more pronounced on floes with greater deformation. All three surface variances therefore show distinct characteristics compared to each other as well as a direct dependency on deformation.

Averaged and normalized Fourier spectra were computed for the snow, ice and ice underside surfaces of each of the three ice groups. The shapes and slopes of the spectra were broadly similar to spectra previously obtained from other Antarctic sea ice regions. The ice surface spectrum had the highest contribution of short scale roughness, indicative of the signature of the ice formation process in the pancake cycle [*Andreas et al.*, 1993]. Through an analogy with fractional Brownian processes, fractal dimensions D were

calculated for the snow and ice underside surfaces. Fractal dimensions D proved to be a useful measures of short wavelength roughness. Values of D were generally higher for the ice underside than for the snow surface, confirming that the former is rougher than the latter. For the snow surface, D gradually decreased with increasing deformation, showing a smoothing effect (less short wave roughness) with age of the floe as increasing amounts of snow filled in between ice surface irregularities. For the ice underside of undeformed and strongly deformed floes, fractal dimensions were high while they showed lower values for medium deformed floes. This tendency was in agreement with the trend of D values, calculated with semivariograms for each ice group as well as for representative single profiles. The knowledge of the fractal structure of snow and ice profiles could be useful for modeling purposes, as different types of sea ice could be simulated as red noise of different fractal dimensions, which in turn could characterize different reflective properties.

Structure lengths and amplitudes and characteristic wavelengths between 3-10 m were obtained for all profile surfaces, using semivariograms. The structural amplitudes of the semivariograms confirmed the findings of the variance analysis. Snow surface structural amplitudes are slightly higher than ice surface amplitudes; ice underside structural amplitudes are distinctly larger (2-5 times). The discrepancy between structural amplitudes generally increased with increasing deformation. A trend of larger structure lengths as well as larger structural amplitudes of the snow surface and the ice underside in contrast to the ice surface can be interpreted as a smoothing tendency of the former two surfaces towards the latter. This indicates that the various processes which occur at the snow/air interface or at the ice/water interface tend to reduce the ice surface roughness.

The wavelet transformation technique is a new two-dimensional space/scale method which can be applied successfully to individual sea ice surface profiles. Wavelets have the advantage of localizing structures and their typical scales in the studied profile; they further reveal the fractal structure of the profile. Spatial summation over the wavelet

transformation gives the scale dependent wavelet variance. With the help of the wavelet variance, dominant structure lengths of a profile can be detected. Wavelets are superior to visual inspection and facilitate the finding of hidden segments and substructures within profiles. This opens the possibility to further subclassify sea ice.

The maximum entropy method is a suitable approach for computing individual profile spectra that are less noisy than Fourier spectra. Typical scales found with the maximum entropy approach compare well to the dominant structure lengths found with the wavelet variance.

Drag coefficients were computed from the surface characteristics of the three profile surfaces. The air drag coefficients are broadly similar to values found for other places in Antarctica and range between 1.1 and 1.7×10^3 with higher drag correlated with increased deformation. Water drag coefficients range between 1.2 and 2.8×10^3. Ice surface drag is similar to or slightly smaller than snow surface (air) drag. This last finding is in contrast to *Andreas et al.* [1993] who computed drag coefficients for the Weddell Sea but found that drag over bare ice is higher than over snow covered ice. Since the drag coefficients are shown to be directly related to the variances for a certain range of wavelengths they are also related to the vertical (amplitude) roughness. The discrepancy between the results of *Andreas et al.*[1993] and the results presented here could therefore be explained in different ways. One possibility for the drag of bare ice to be lower than that of snow covered ice could be the effect of blowing snow and windblown sastrugi structures leading to higher snow surface amplitudes. Another possibility could be a smoothing of the ice surface roughness as a consequence of flooding and snow ice formation, two processes which were frequently observed in the area of study [*Adolphs*, 1; *Sturm et al.*, submitted].

Application of various methods showed an intricate relation between ice group and roughness properties of sea ice. Roughness properties are crucial parameters for classifying sea ice. Ice classification, is on the other hand, an important precondition for classifying roughness properties. With roughness determining the spectral and reflective

characteristics of a surface, the identification of ice groups with remote sensing methods is possible. For future research on roughness characteristics of sea ice in the Antarctic it would be desirable to explore, beyond the limits given in this paper (2-60 m), broader ranges of scales and wavelengths. This requires longer profile lengths as well as smaller sampling intervals, which could be best achieved in using airborne laser or underwater upward looking sonar methods.

II.9 References

Adolphs, U., Spatial and temporal variability of snow and ice thickness in the South polar pacific ocean, thesis paper 1.

Ackley, S.F., W.D.Hibler III, F.K.Kugzruk, A.Kovacs and W.F.Weeks, Thickness and roughness variations of Arctic multiyear sea ice, *CRREL Rep. 76-18*, 25 pp., U.S.Army Cold Reg.Res. and Eng.Lab., Hanover, N.H., 1976.

Ackley , S.F., M.A. Lange and P.Wadhams, Snow cover effects on Antarctic sea ice thickness, in Sea Ice Properties and Processes, edited by S.F. Ackley and W.F.Weeks, *CRREL Monograph 90-1*, pp. 16-21, U.S. Army Corps of Engineers, Hanover, NH, 1990.

Ackley, S.F., P.Wadhams and M.Lange, Sea-ice investigations during the Winter Weddell Sea Project, *Antarct.J.U.S.*, 22, 88-89, 1987.

Allison, I. and G. Akerman, Sea ice and ocean energy balance studies at Mawson, Antarctica, in *Sea Ice Processes and Models*, edited by R.S.Pritchard, pp 347-359, University of Washington Press, Seattle, 1980.

Allison, I. and A.P. Worby, 1994, Seasonal changes of sea-ice characteristics off East Antarctica, *Ann. Glaciol., 20*, 195-201.

Anderson, R.J., Wind stress measurements over rough ice during the 1984 marginal ice zone experiment, *J.Geophys.Res.*, 92(C7), 6933-6941, 1987.

Andreas, E.L., A theory for the scalar roughness and the scalar transfer coefficients over snow and sea ice, *Boundary Layer Met., 38*, 159-184, 1987.

Andreas, E.L., Air-ice drag coefficients in the western Weddell Sea, *J.Geophys.Res., 100* (C3), 4833-4843, 1995.

Andreas, E.L. and S.F.Ackley, On the differences in ablation seasons of Arctic and Antarctic sea ice, *J.Atmos.Sci.,39*, 440-447, 1982.

Andreas, E.L., Lange, M.A., Ackley, S.F. and P. Wadhams, Roughness of Weddell Sea ice and estimates of the air-ice drag coefficient, *J.Geophys.Res., 98*(C7), 12,439-12,452,1993.

Andreas, E.L. and A.P.Makshtas, Energy exchange over Antarctic sea ice in the spring, *J.Geophys.Res., 90*(C4), 7199-7212, 1985.

Andreas, E.L. and B.Murphy, Bulk transfer coefficients for heat and momentum over leads and polynyas, *J.Phys.Oceanogr., 16*, 1875-1883, 1986.

Arya, S.P.S., Air friction and form drag on Arctic sea ice, AIDJEX Bulletin, 43-57, 1973a.

Arya, S.P.S., Contribution of form drag on pressure ridges to the air stress on Arctic ice, *J.Geophys.Res., 78*(30), 7092-7099, 1973b.

Arya, S.P.S., A drag partition theory for determining the large-scale roughness parameter and wind stress on the Arctic pack ice, *J.Geophys.Res.*, 80(24), 3447-3454, 1975.

Banke, E.G. and S.D.Smith, Wind stress on Arctic sea ice, J.Geophys.Res., 78, 7871-7883, 1973.

Banke, E.G., S.D. Smith and R.J.Anderson, Drag coefficients at AIDJEX from sonic anemometer measurements, in *Sea Ice Processes and Models*, edited by R.S.Pritchard, pp 430-442, University of Washington Press, Seattle, 1980.

Barton, C.C., P.R.La Pointe, Fractals in the Earth Sciences, Plenum Press, New York, 1995.

Bishop, G.C. and S.E.Chellis, Fractal dimension: A descriptor of ice keel surface roughness, *Geophys.Res.Lett.*,*16*(9), 1007-1010, 1989.

Dierking, W., Laser profiling of the ice surface topography during the Winter Weddell gyre study, *J.Geophys.Res.*, *100*(C3), 1995.

Eicken, H., M.A.Lange, H.W.Hubberten and P.Wadhams, Characteristics and distribution patterns of snow and meteoric ice in the Weddell Sea and their contribution to the mass balance of sea ice, *Ann. Geophys.*, 12, 80-93, 1994.

Fetterer, F.M., D.Gineris and R.Kwok, Sea ice type maps from Alaska Sythetic Aperture Radar Facility imagery: An assessment, *J.Geophys.Res.*, 99(C11), 22,443-22,458, 1994.

Govoni, J.W., S.F. Ackley and E.T.Holt, Surface roughness of Ross Sea pack ice, *Ant. J. U.S.*, *18*(5), 123-124, 1983.

Guest, P.S. and K.L.Davidson, The effect of observed ice conditions on the drag coefficient in the summer East Greenland sea marginal ice zone, *J.Geophys.Res.*, *92* (C7), 6943-6954, 1987.

Guest, P.S. and K.L.Davidson, The aerodynamic roughness of different types of sea ice, *J.Geophys.Res.*, 96(C3), 4709-4721, 1991.

Hibler, W.D.,III, Characterization of cold-regions terrain using airborne laser profilometry, *J.Glaciol.*, *15*, 329-347, 1975.

Hibler, W.D.,III and L.A.LeSchack, Power spectrum analysis of undersea and surface sea-ice profiles, *J.Glaciol.*,*11*,345-356, 1972.

Isaaks, E.H. and R.M. Srivastava, Applied Geostatistics, Oxford University Press, 1989.

Joffre, S.M., Determining the form drag contribution to the total stress of the atmospheric flow over ridged sea ice, *J.Geophys.Res.*, *88*(C7), 4524-4530, 1983.

Johansson, R. and J.Askne, Modelling of radar backscattering from low-salinity ice with ice ridges, *Int.J.Remote Sens.*, *8*(11), 1667-1677, 1987.

Kaimal, J.C. and L.Kristensen, Time series tapering for short data samples, *Boundary Layer Meteorol.*, *57*, 187-194, 1991.

Kaiser, G., A friendly guide to wavelets, Birkhauser, 300pp, 1994.

Kaufman, L., P.J. Rousseeuw, Finding groups in data, Wiley Series in Probability and Mathematical statistics, 342pp, 1990.

Key, J. and A.S. McLaren, Fractal nature of the sea ice draft profile, *Geophys.Res.Lett.*, *18*(8), 1437-1440, 1991.

Kozo, T.L. and W.B. Tucker, Sea ice bottomside features in the Denmark Strait, *J.Geophys.Res.*,79(30), 1974.

Lange, M.A., S.F.Ackley, P.Wadhams, G.S.Dieckmann and H.Eicken, Development of sea ice in the Weddell Sea, *Ann. Glaciol.*, *12*, 92-96, 1989.

Lange, M.A. and H.Eicken, The sea ice thickness distribution in the Northwestern Weddell Sea, *J. Geophys.Res.*, *96*(C3), 4821-4837, 1991.

Li, B.L. and C. Loehle, Wavelet analysis of multiscale permeabilities in the subsurface, *Geophys. Res. Lett.*, 22(23), 3123-3126, 1995.

Lytle, V.I. and S.F. Ackley, Sea ice ridging in the Eastern Weddell Sea, *J.Geophys.Res.*, *96* (C10), 18,411-18,416, 1991.

Meyer, Y., Wavelets: Algorithmen and Applications, SIAM, Philadelphia, 1993.

McBratney, A.B. and Webster, R., Choosing functions for semi-variograms of soil properties and fitting them to sampling estimates, *J.Soil Science*, *37*, 617-639, 1986.

Oliver, M.A. and R.Webster, Semi-variograms for modelling the spatial pattern of landform and soil properties, *Earth Surface Processes and Landforms*, *11*, 491-504, 1986.

Overland, J.E., Atmopheric boundary layer structure and drag coefficients over sea ice, *J.Geophys.Res.*, *90*(C5), 9029-9049, 1985.

Paterson, J.S., B.Brisco, S.Argus and G.Jones, *In situ* Measurements of micro-scale surface roughness of sea ice, *Arctic*, *44*(1), 140-146, 1991.

Robert, A. and K.S.Richards, On the modelling of sand bedforms using the semivariogram, *Earth Surface Processes and Landforms*, *13*, 459-473, 1988.

Romesburg, H. C., Cluster Analysis for Researchers, Lifetime Learning Publications, 334pp, 1984.

Rothrock, D.A. and A.S. Thorndike, Geometric properties of the underside of sea ice, *J.Geophys.Res.*, *85* (C7), 3955-3963, 1980.

Steffen, K. and J.Heinrichs, Feasibility of sea ice typing with synthetic aperture radar (SAR): Merging of Landsat thematic mapper and ERS 1, *J.Geophys.Res.*, 99(C11), 22,413-22,424, 1994.

Sturm, M., K. Morris and R. Massom, The character and distribution of the winter snow cover on the sea ice of the Bellingshausen, Amundsen and Ross Seas, Antarctica, 1994-1995, [J.G.R. in press].

Therrien, C.W., Discrete Random Signals and Statistical Signal Processing, Prentice Hall Signal Proc.Series, 1992.

Tucker, W.B.III, D.K.Perovich, A.J.Gow, W.F.Weeks and M.R.Drinkwater, Physical Properties of sea ice relevant to remote sensing, in Microwave Remote Sensing of Sea ice, *Geophys.Monogr.Ser.*, *68*, edited by F.Carsey, pp 9-28, AGU, Washington DC, 1992.

Tucker, W.B.III, W.F.Weeks and M.Frank, Sea ice ridging over the Alaskan continental shelf, *J.Geophys.Res.*, *84*(C8), 4885-4897, 1979.

Turcotte, D.L., Fractals and chaos in geology and geophysics, Cambridge University Press, 1992.

Wadhams, P., A comparison of sonar and laser profiles along corresponding tracks in the Arctic ocean, in *Sea Ice Processes and Models*, edited by R.S.Pritchard, pp 283-299, University of Washington Press, Seattle, 1980.

Wadhams, P. and N.R. Davis, The fractal properties of the underside of Arctic sea ice, in *Marine, Offshore and Ice Technology*, 353-363, 1994.

Wadhams, P., M.A. Lange and S.F. Ackley, The ice thickness distribution across the Atlantic sector of the Antarctic Ocean in midwinter, *J.Geophys.Res.*, *92*(C13), 14,535 14,552, 1987.

Wamser, C. and D.G. Martinson, Drag coefficients for winter Antarctic pack ice, *J.Geophys.Res.*, *93*(C7), 12,431-12,437, 1993.

Weeks, W.F., S.F. Ackley and J.Govoni, Sea ice ridging in the Ross Sea, Antarctica as compared with sites in the Arctic, *J.Geophys.Res.*, *94*(C4), 1989.

Winebrenner, D.P., E.D.Nelson, R.Colony and R.D.West, Observation of melt onset on multiyear Arctic sea ice using the ERS 1 synthetic aperture radar, *J.Geophys.Res.*, 99(C11), 22,425-22,441, 1994.

Wornell, G., Signal Processing with Fractals: A wavelet-based approach, Prentice-Hall, 1996.

II.10 Figures

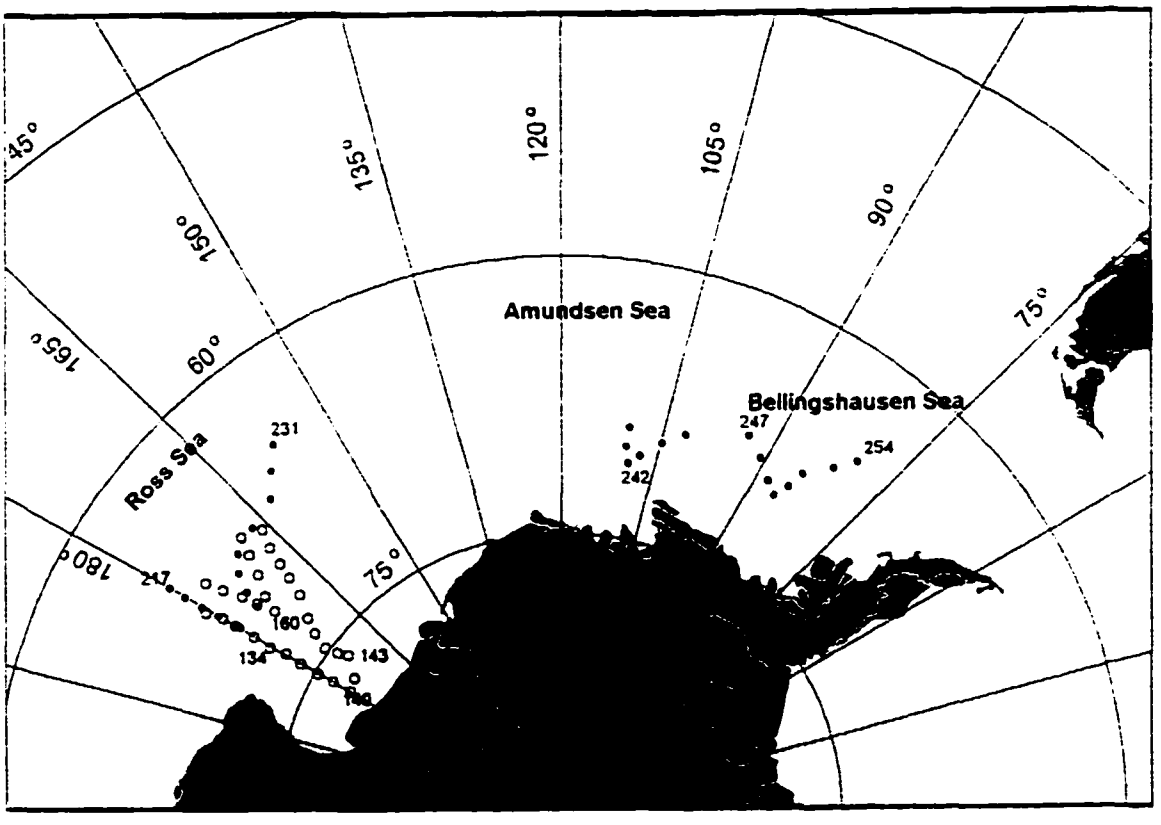

Figure II.1: Ice stations along three track lines followed by the Nathaniel B. Palmer (NBP) between May and September 1995. NBP 95-3 (open circles) visited the Ross Sea in early winter (May/June 95), NBP 95-5/1 (filled circles) in late winter (August 95). During cruise NBP 95-5/2 (September 95) a track of another 14 ice stations was laid out in the Amundsen/ Bellingshausen Seas.

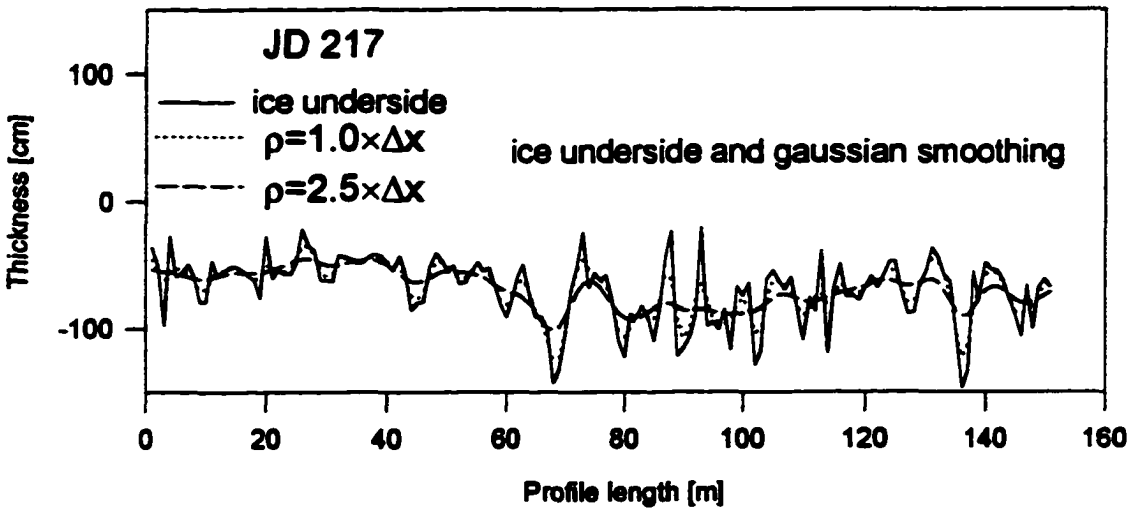

Figure II.2: Ice underside of a floe, sampled on Julian Day 217 in the Ross Sea. Both, measured and smoothed versions with gaussian widths $\rho = 1\ \Delta x$ and $2.5\ \Delta x$ are shown ($\Delta x = 1$ m).

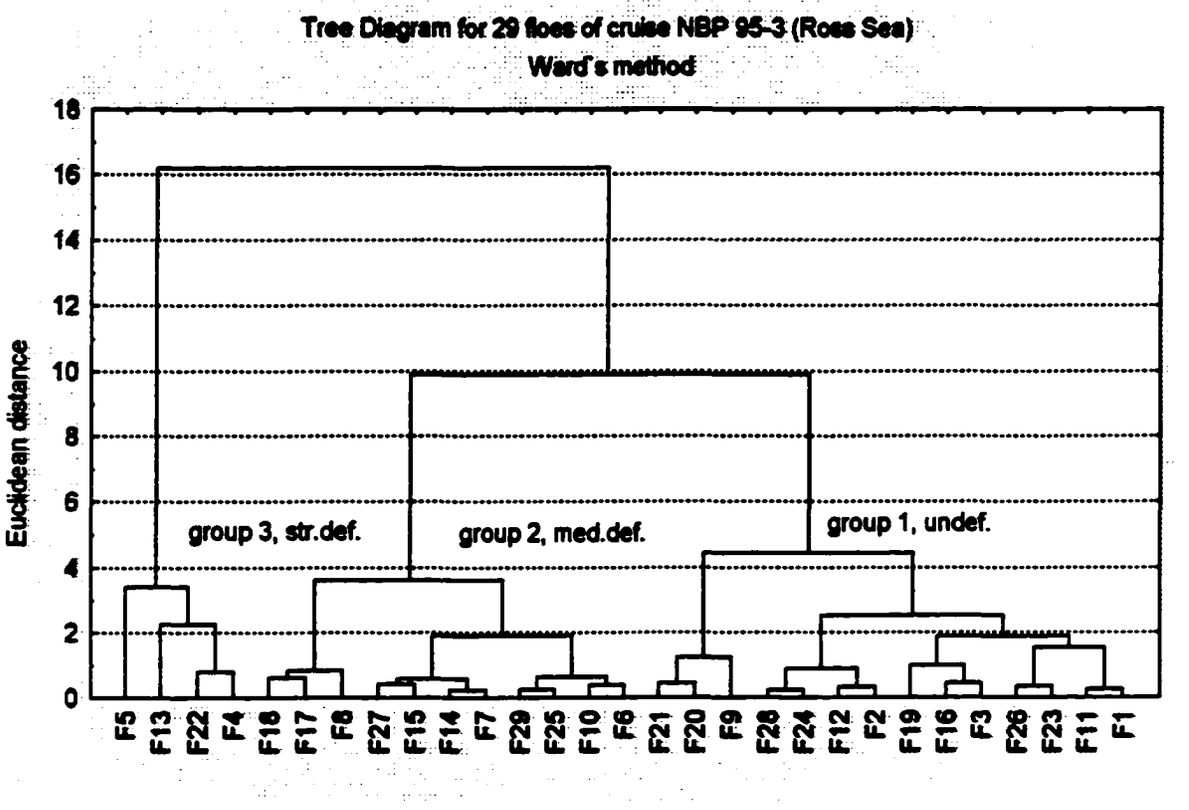

Figure II.3: Hierarchical cluster diagram for the 29 floes of the early winter Ross Sea cruise. Individual floes branch together to subcluster with increasing distance. Below distance 10 three distinct branches have formed, representing three different visibly distinct ice groups.

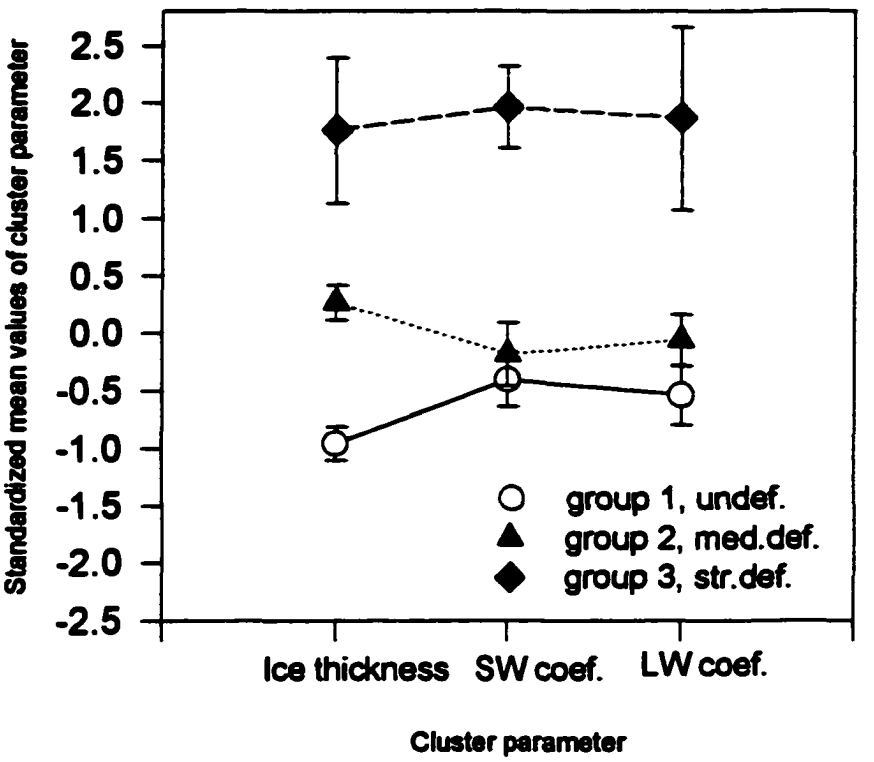

Figure II.4: Mean values of the three selected cluster variables (ice thickness, short wave coefficient and long wave coefficient) for the three resultant groups of a k-means algorithm applied on all 57 given ice floes.
Group 1 contains undeformed, group 2 medium deformed and group 3 strongly deformed floes. Attached error bars represent 95% confidence intervals.

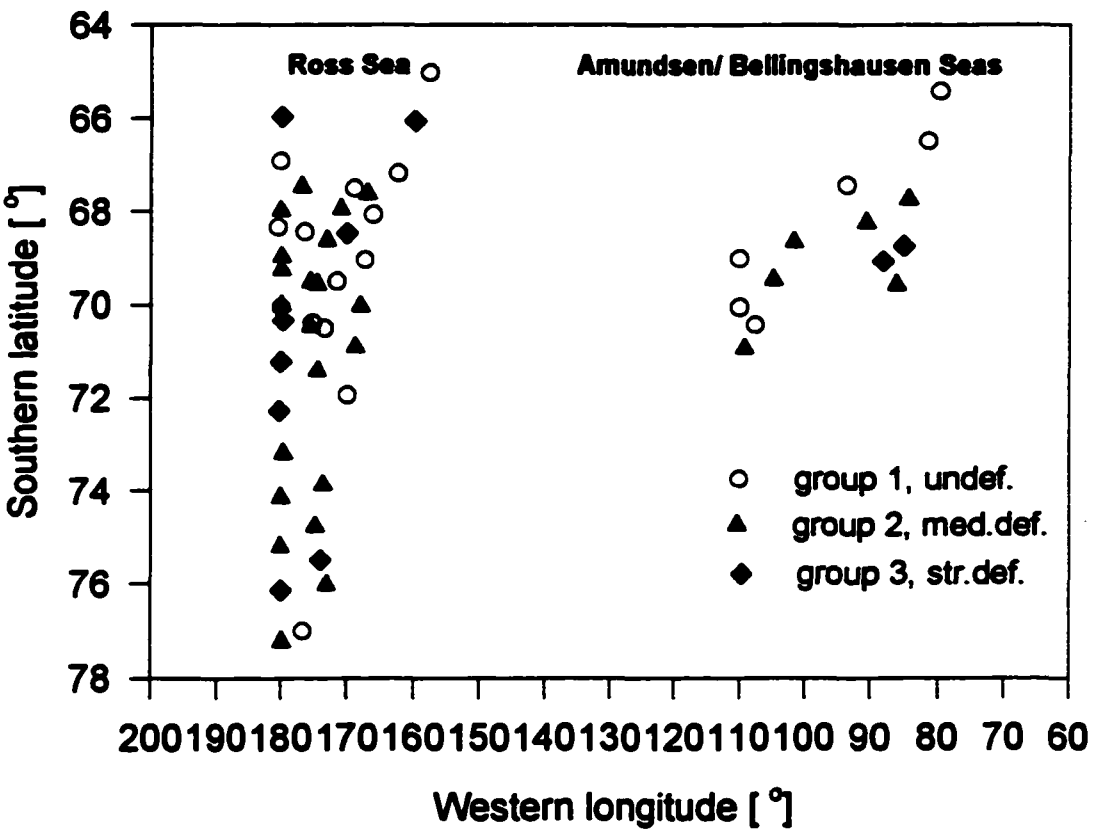

Figure II.5: Distribution of group 1,2 and 3 floes in a longitude-latitude diagram. Drilling locations in the Amundsen/Bellingshausen Seas are fewer and in a longitudinal sector (between 80° and 110°) which is visibly apart from the Ross Sea sites.

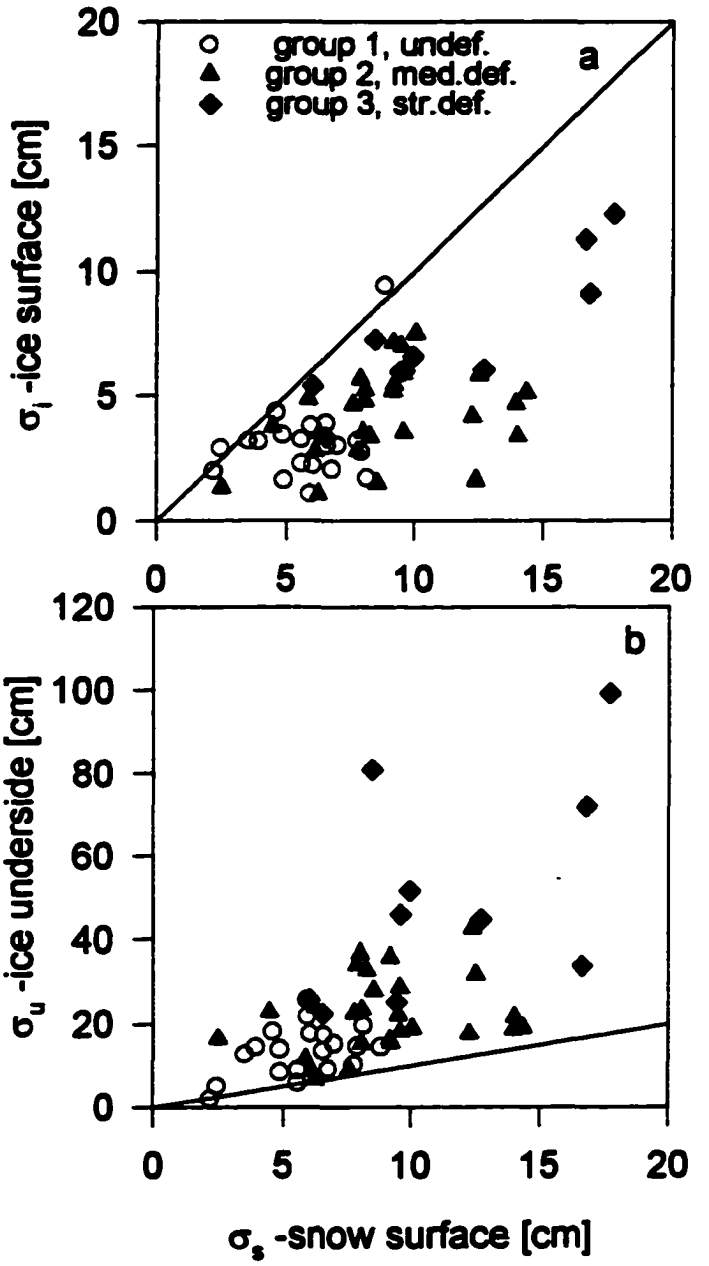

Figure II.6: Standard deviations of the ice surface and ice underside versus standard deviations of the snow surface for all 57 floes of the three ice groups. The solid line shows a 1:1 relationship for comparison.

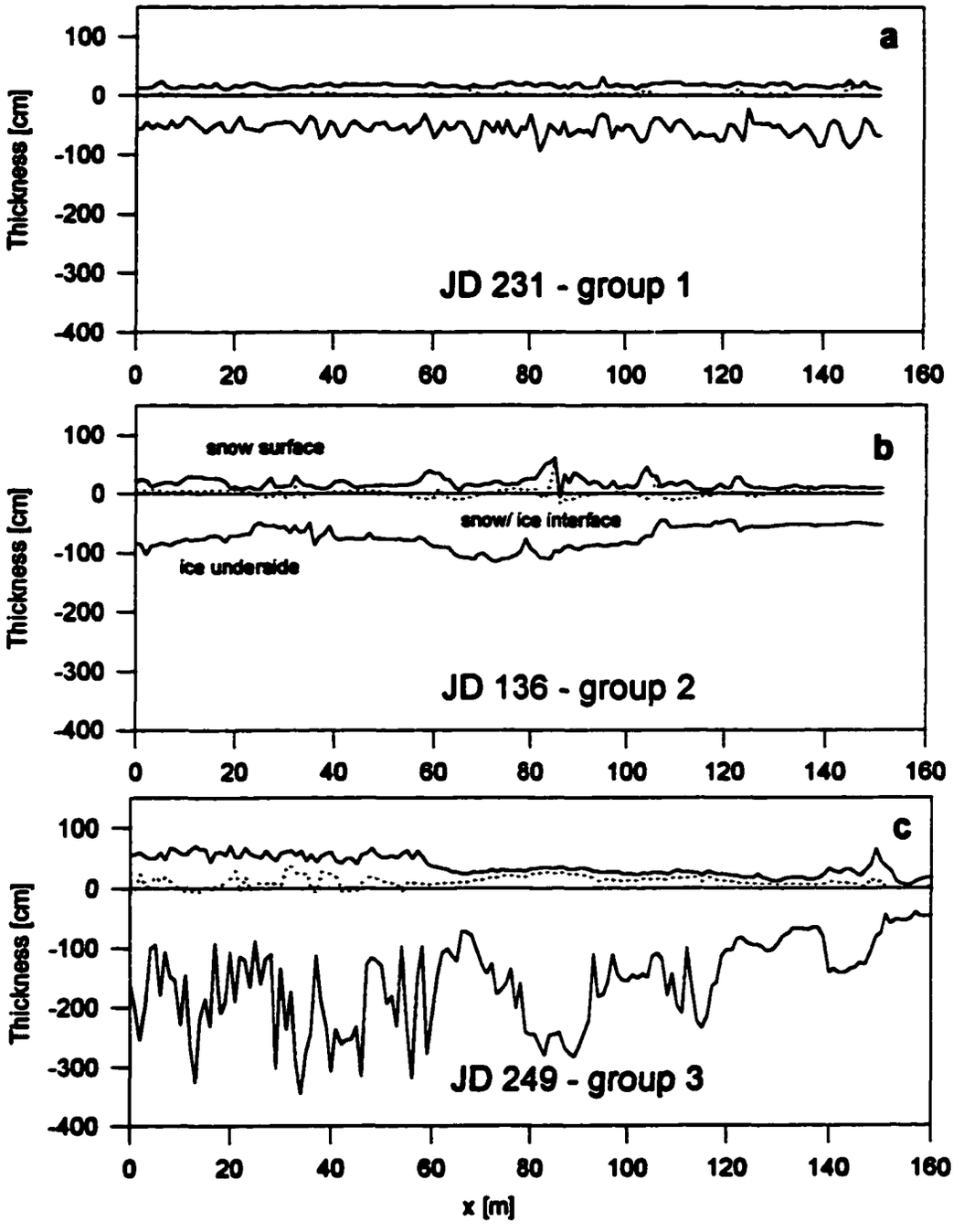

Figure II.7: Snow and ice thickness profiles chosen as representative for the three ice groups. The floe (a) sampled at JD (Julian Day) 231 belongs to group 1 (undeformed floes), floe (b) of JD 136 belongs to group 2 (medium deformed floes) and floe (c) at JD 249 belongs to group 3 (strongly deformed floes). Lines of thickness are referenced to the water level (zero line).

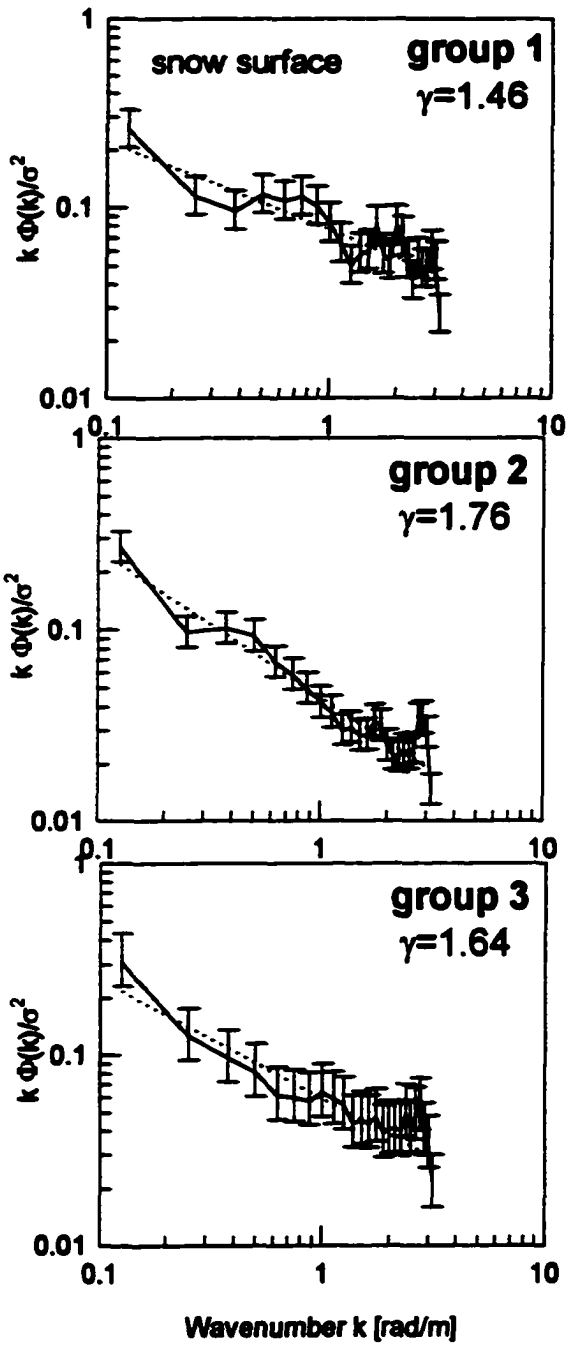

Figure II.8: Averaged and nondimensionalized Fourier spectra for the snow surface (a), ice surface (b) and ice underside (c) for each of the three ice groups. The error bars indicate 95% confidence intervals. Dotted lines indicate least squares regression lines fitted to the log-log plots of the spectra.

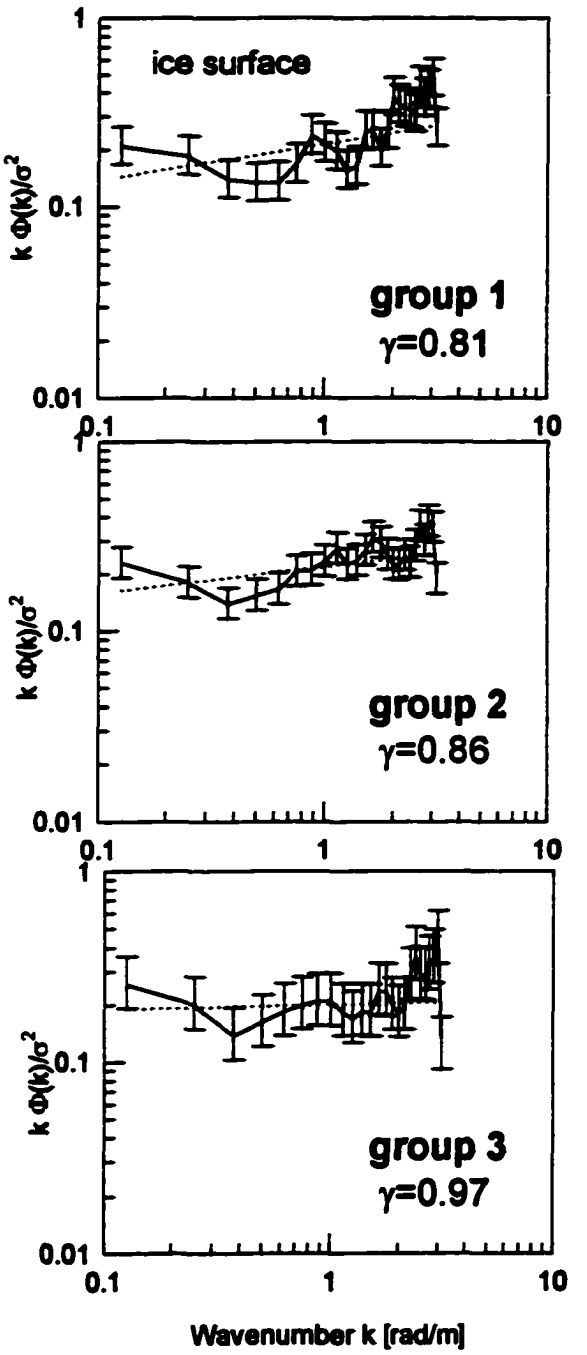

Figure II.8: (continued).

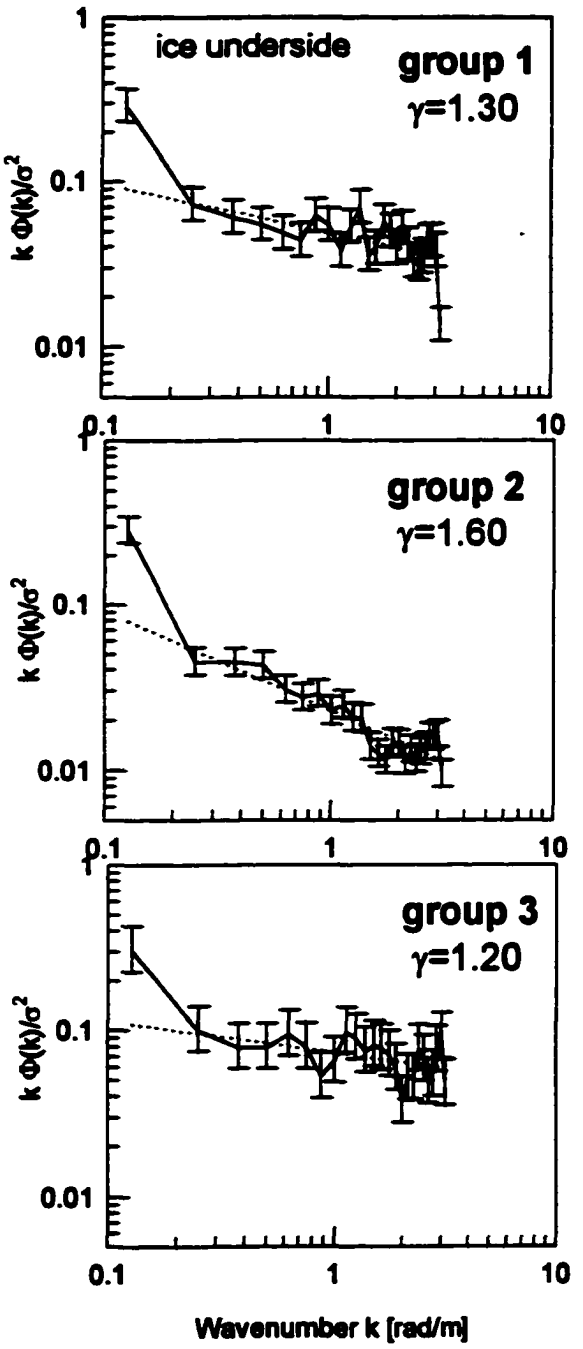

Figure II.8: (continued).

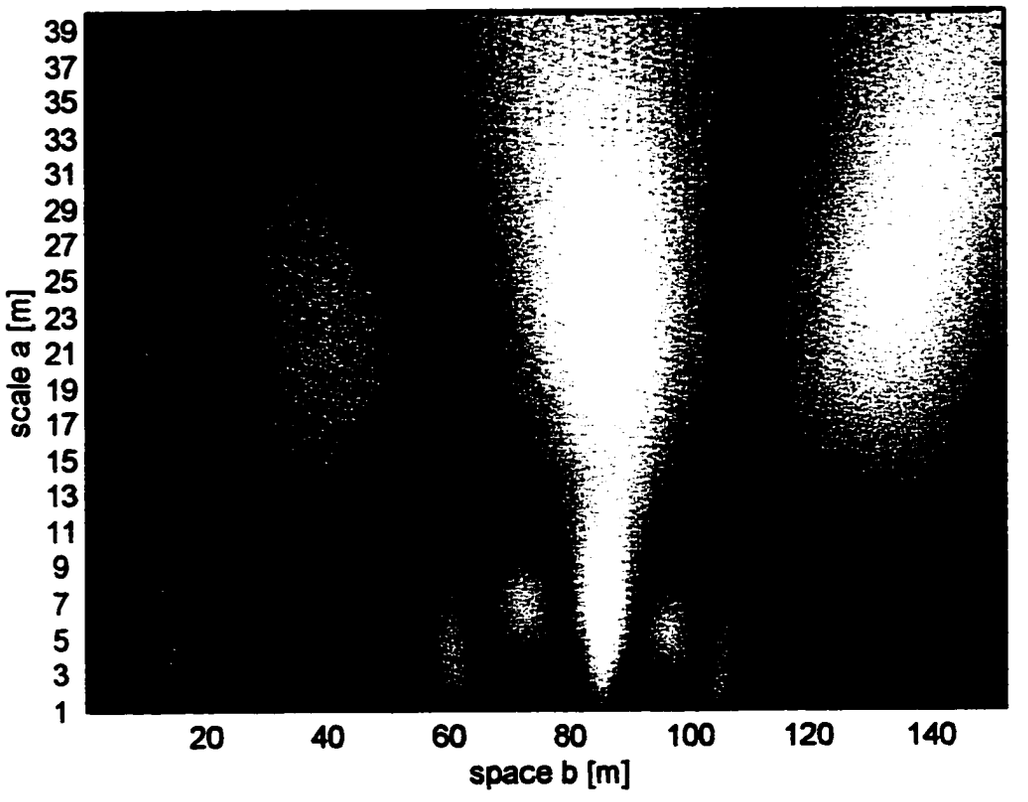

Figure II.9: Two-dimensional space-scale presentation with wavelets for the snow surface of the group 2 floe, shown in Figure II.7b.

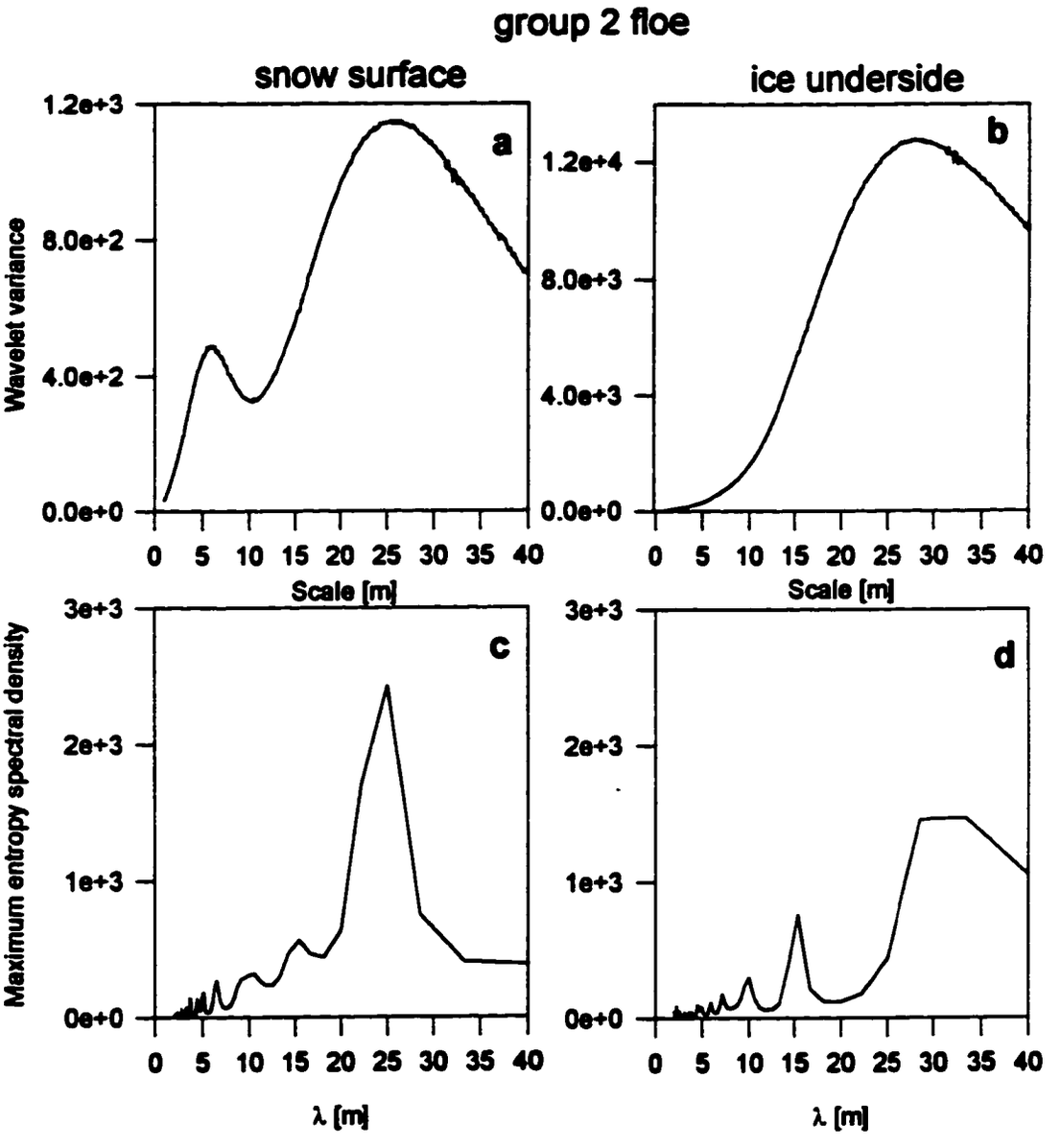

Figure II.10: Wavelet variances and maximum entropy spectral densities (order M=40) for the snow surface and ice surface of the group 2 floe (Figure 7b).

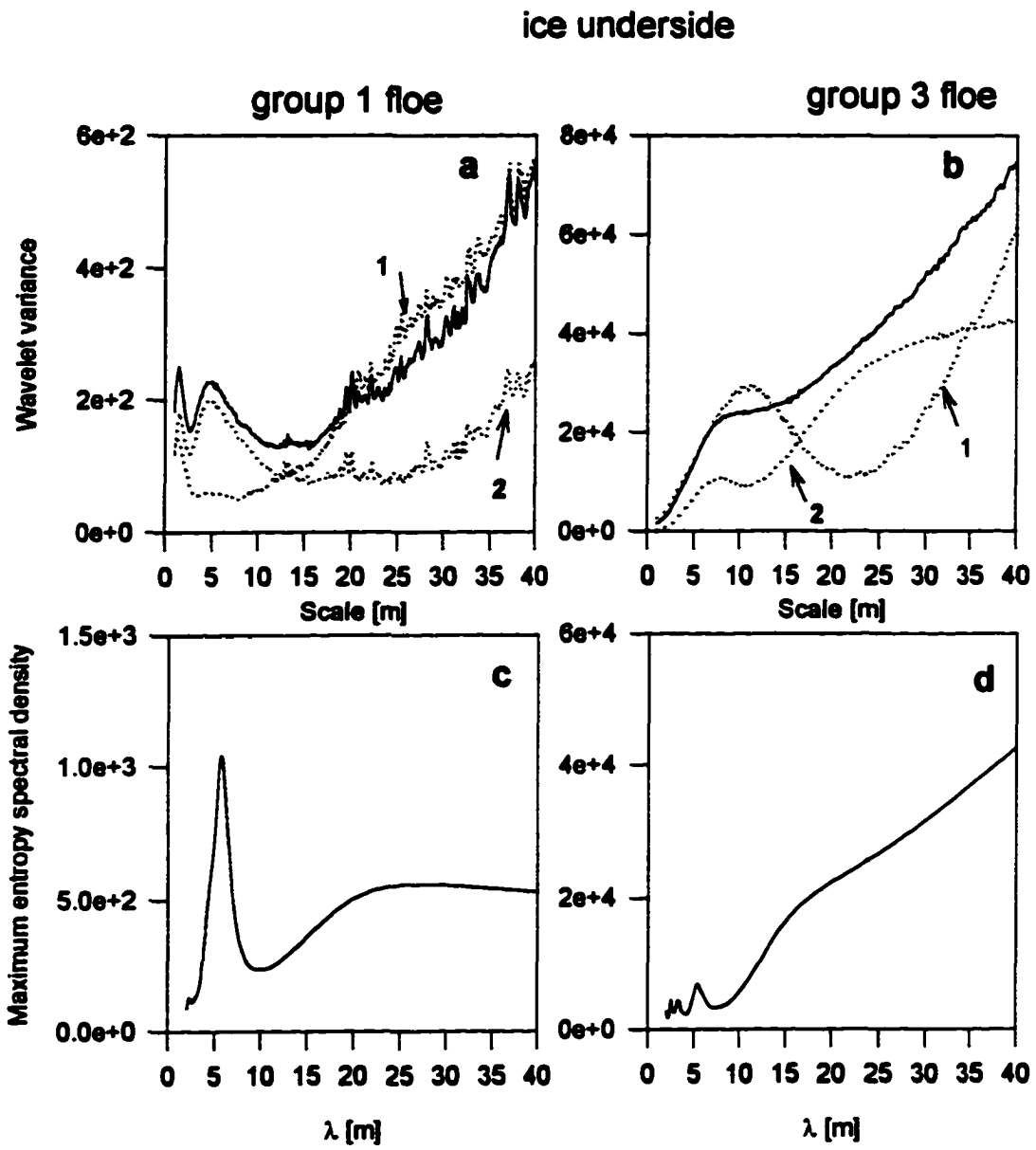

Figure II.11: Wavelet variances and maximum entropy spectral densities (order M=10) for the ice underside of group 1 and group 3 floe (Figure 7).

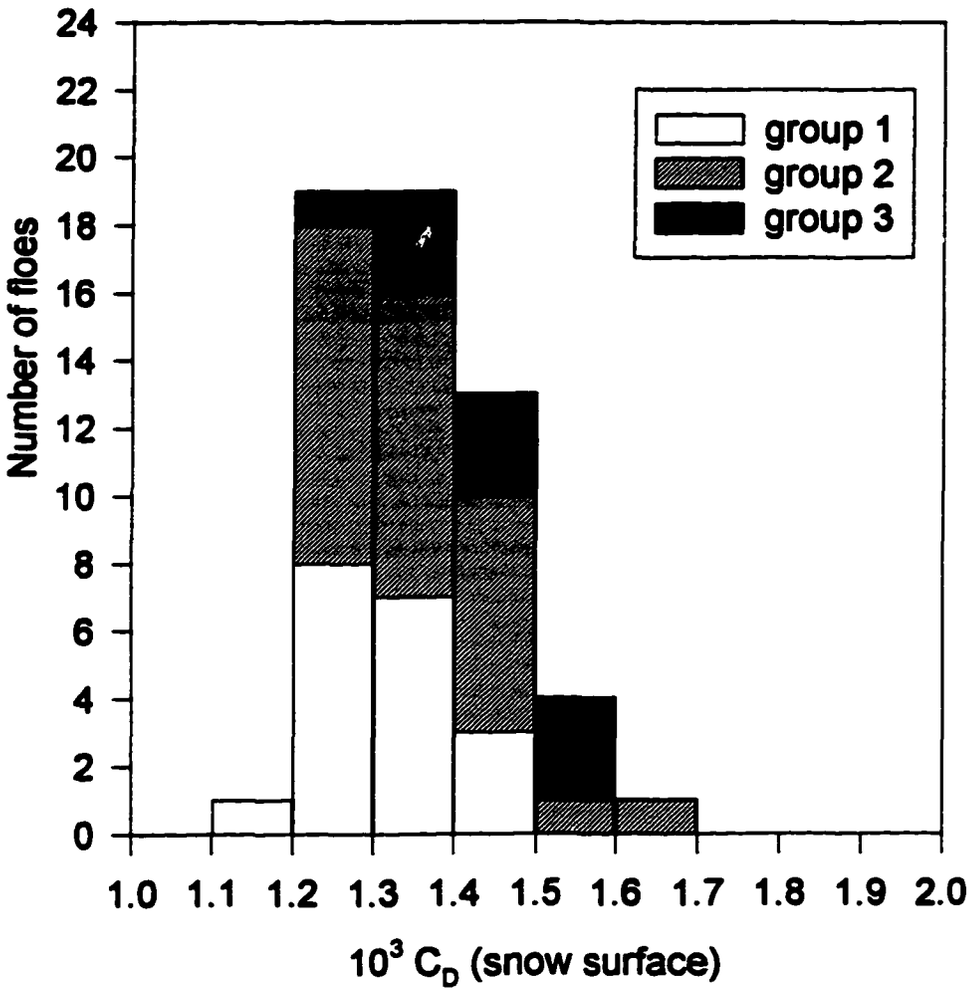

Figure II.12: Histogram showing the distribution of the neutral stable, 10 m air-ice drag coefficients for all floes of the three ice groups.

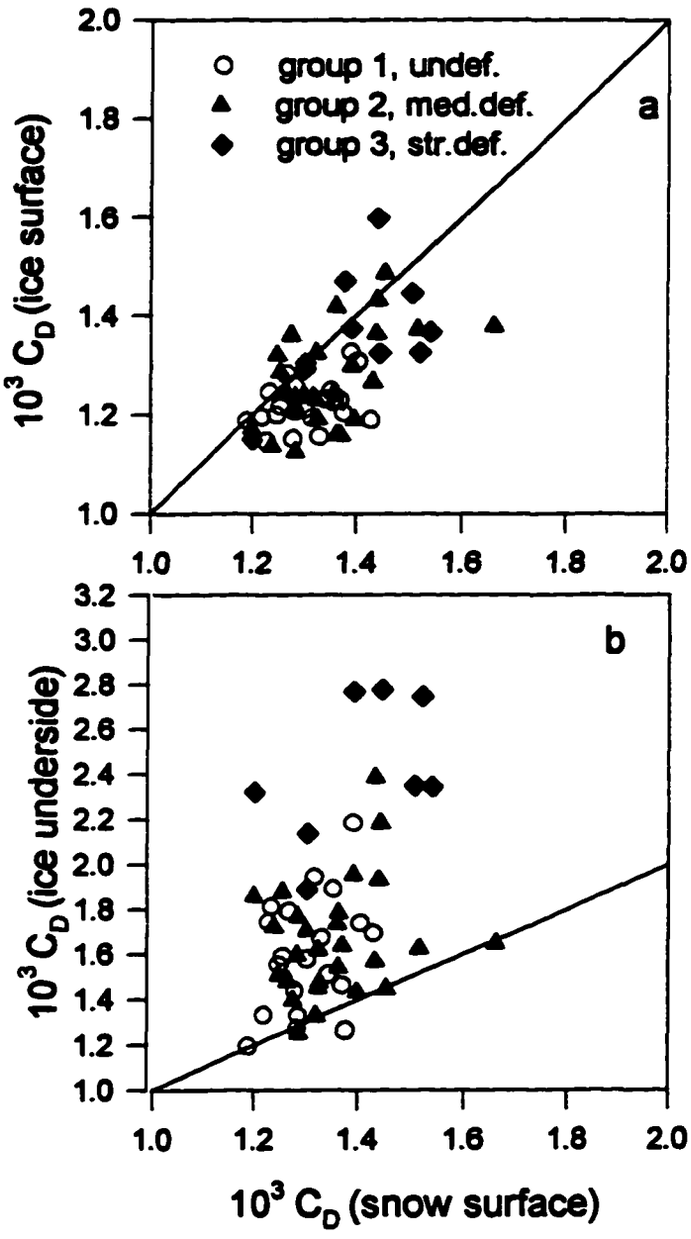

Figure II.13: Drag coefficients of the ice surface and ice underside as compared to the air drag coefficients for all floes of the three ice groups. The solid line shows a 1:1 for comparison.

II.11 Tables

Table II.1. Decay parameter γ and fractal dimensions D determined by Fourier spectra and semivariograms for all groups and single profiles.

	snow surface		ice underside		single profiles from SV		ice surface
	Fourier[1)]	SV[2)]	Fourier	SV	snow surface	ice underside	Fourier
group 1 (19 floes)	γ=1.46 D=1.77	D=1.85	γ=1.30 D=1.85	D=1.83	D=1.96	D=1.98	γ=0.81
group2 (28 floes)	γ=1.76 D=1.62	D=1.79	γ=1.60 D=1.70	D=1.75	D=1.89	D=1.66	γ=0.86
group3 (10 floes)	γ=1.64 D=1.68	D=1.76	γ=1.20 D=1.90	D=1.80	D=1.69	D=1.86	γ=0.97

[1)] from Fourier spectra
[2)] from Semivariograms (SV)

Table II.2. Mean structural amplitudes *A*, structure lengths *R* and characteristic wavelengths λ, determined with semivariograms for the snow and ice and ice underside surfaces of all ice groups.

	ice underside			ice surface			snow surface		
	A_u [1] [cm]	R_u [m]	λ_u [cm]	A_i [cm]	R_i [m]	λ_i [cm]	A_s [cm]	R_s [m]	λ_s [cm]
group 1	13.2	11.4	5.4	3.7	8.2	3.7	7.4	16.3	6.3
group 2	22.1	19.0	8.8	4.1	9.6	6.3	9.2	15.8	7.1
group 3	36.8	7.8	10.4	7.6	12.0	5.2	10.6	14.9	9.1

[1] Subscripts u,i,s stand for underside, ice surface and snow surface.

Table II.3. Mean drag coefficients for snow and ice surface and ice underside for all ice groups.

	drag coefficients $C_D \times 10^3$		
	snow surface	ice surface	ice underside
group 1	1.31	1.22	1.59
group 2	1.35	1.27	1.67
group 3	1.40	1.37	2.66

III. Sea ice profiles: how much data is needed to obtain spatially representative estimates of mean ice and snow thicknesses in the Southern Ocean

III.1 Abstract

Drilling profiles and shipboard observations of ice and snow thickness, made during three Antarctic expeditions in the Ross, Amundsen and Bellingshausen Seas are studied to discern their tolerance towards subsampling. Three different subsampling methods: 'weedout', 'random' and 'sectional', were used on the drilling profiles of individual floes and on groups of profiles separated with respect to the specific cruise involved and to the degree of ice deformation. The resulting subsampling errors, associated with the means and standard deviations of ice-, snow thicknesses and freeboard were generally smallest for the 'weedout' method, where the spacing between drilling points was increased with increasing subsampling degree n (while the profile length was unchanged). On the 'cruise' level, floe drilling data and shipboard observations (consisting of individual sets of 25 single observations) were subsampled by picking every n-th floe (or observation set). Up to a subsampling degree of $n = 3$, errors were negligible against the inherent errors of the full data sets. The influence of sampling methods on the shape of the measured probability density functions (PDFs) is studied indirectly by considering the statistical properties of the full data sets. It was found that *lognormal* or *gamma* distributions are better statistical representations for both drilling and shipboard data than *normal* distributions. A simple statistical ice thickness model is presented which explains how different ice growth and development processes influence the shape of the ice thickness PDF. Appropriate choices of the parameters, consistent with cruise dates and observational evidence of ice

deformation, gives good representations of the measured ice thickness PDFs for the three cruises.

III.2 Introduction

Due to lack of submarine sonar-measured ice thickness, information concerning antarctic sea ice stems mainly from drilling profiles, [*Lange and Eicken*, 1991; *Worby et al.*, 1996]. Because the acquisition of drilling data is comparatively time-consuming, it is useful to examine how representative such data are and how much data are needed in order to obtain reliable estimates about any sea ice area. A study with similar focus has been carried out for Arctic data, where large sets of sonar data exist [*Eicken and Lange*, 1989]. They showed that even short drilling profiles can supply as much representative information about sea ice thickness as extensive measurements of ice draft by submarines.

This study considers two different data sets of antarctic sea ice, denoted as *Sets A* and *B*. *Set A* consists of drilling profile data while *Set B* is a set of continuous shipboard observations of snow and ice thickness. These two data sets were acquired during three cruises on board the research vessel *Nathaniel B. Palmer* (NBP) between May and September 1995. The cruise tracks are shown in Figure III.1. NBP 95-3 was an early winter (May/June 95) expedition to the Ross Sea, NBP 95-5/2 was a repeat visit of the Ross Sea in late winter (August 95) and NBP 95-5/1 crossed the late winter Amundsen/Bellingshausen Seas (September 95).

The advantages, drawbacks and mutual representativeness of the different sampling used to obtain the data in *Sets A* and *B* are discussed in *Adolphs* [1]. For *Set A*, a characteristic floe was selected as a drilling station at about every degree of latitude along the cruise track. At each station typically 150 holes were drilled at a spacing of 1 m along straight or angled lines. On the basis of both ice thickness and roughness characteristics, the 57 floes, which were sampled during these three cruises, were grouped into three different floe groups, according to their degree of deformation (group 1 to 3) [*Adolphs*, 2]. The shipboard measurements (*Set B*) were obtained by making 25 visual estimates of

snow and ice thickness hourly for individual floe pieces which were tipped over by the ship. A distance class algorithm, which picks one set of 25 snow and ice thickness values for each 10 km, was used in order to sort the data according to distance from the ice edge. As discussed in [*Adolphs*, 1] the *Set B* data best represent the thin to medium thick ice, whereas the drilling data (*Set A*) sample most representatively medium (> 30 cm) to thick ice. However, a relationship of mutual representativeness of both methods in the area of overlap was also observed [*Adolphs*, 1].

In the following two sections, data *Sets A* and *B* will be considered separately. The tolerance of mean values and standard deviations of these data sets is examined with respect to different strategies and degrees of subsampling. The goal is to find a more optimized way to attain regionally representative information about mean snow and ice thickness that requires the least amount of data. The direct use of this analysis is to show the degree of reliability and intercomparability of present data sets; for future studies it offers the possibility of organizing measurement programs that are both more cost and time efficient. Finally, in section 4, the statistical characteristics of typical ice thickness distributions are explored beyond just mean values and standard deviations. It will be shown that the shape of an individual ice thickness Probability Density Function (PDF) does not fit a simple normal distribution, but can be interpreted as the superposition of several distributions, each characterizing different growth and development processes.

It is important to note that the present subsampling study is focussed on conserving information about the statistical distribution of the data; i.e. the data are treated as sets of independent elements with no spatial relationship between them. For other than statistical information, which depends on the spatial relationship of the individual data points, subsampling may not be a desirable option. An example is the roughness information, which can be obtained from ice thickness profiles. In this case, subsampling would further reduce the wavelength spectrum, which is already limited to a relatively narrow range of 2 to 60 m for the original data [*Adolphs*, 2].

III.3 Statistical properties of the drilling data (Set A)

III.3.1 Directional bias

The drilling data were usually sampled across a long (100 m) profile, parallel to the heading of the ship, and a short (50 m) profile, perpendicular to the first one. The placement of the long profile was based on the need to representatively cover level and ridged ice. The direction of the perpendicular short profile was then determined and its placement was less influenced by direct subjective judgement. This raises the question whether a possible anisotropy or bias can be found between these two profile types. In order to investigate this, mean ice thickness values along two 50 m sections of the long profile and along the short profile were compared. Figure III.2 shows the bar graphs for the difference in mean ice thickness values for all floes of all considered cruises. While there can be distinct differences between two 50 m sections of individual floes, these differences do not appear to be more pronounced for sections oriented in different directions in contrast to sections along the same direction. As can be seen in Figure III.2, the standard deviations for both cases describe a very similar width around the means -2 cm and 0.9 cm which are sufficiently close to zero. This confirms a general directional independence. It therefore can be concluded that in the Antarctic sea ice is generally isotropic and that the choice of profile direction does not introduce a bias (both graphs in Figure III.2 are centered at zero difference).

III.3.2 Subsampling bias

III.3.2.1 Three different subsampling methods

There are different methods for picking smaller subsets from an original data set of profile lines. A comparison, based on the associated subsampling errors, can be used to decide on an optimum subsampling method. In the following, three different methods are considered. Starting with a typical spacing of 1 m between drilling points, for the first

method (*'weedout'*) the spacing (or subsampling degree) n is progressively enlarged to 2 m, 3 m up to 25 m. As a consequence of this subsampling method the number of subsampling possibilities increases with n. For the second method (*'random'*), sets of m drilling points are drawn randomly for each floe. The number of sets formed is chosen to be inversely proportional to m. The third method (*'sectional'*) chooses contingent subsections of m drilling points (with measurements spaced at 1 m distance). Again, the number of possible sets (subsections) is inversely proportional to m. These different approaches will be applied first to representative floes from each of the three ice groups (group 1: undeformed floes, group 2: medium deformed floes, group 3: strongly deformed floes) which were established in [*Adolphs*, 2]. Following this analysis, subsampling of the data set of a whole cruise will be considered.

III.3.2.2 Results for representative individual floes

Three individual floes that were found to be representative of undeformed (group 1), medium deformed (group 2) and strongly deformed (group 3) ice in [*Adolphs* 2] were subsampled. Figure III.3 shows results of mean ice thickness, mean snow thickness and mean freeboard of subsets obtained with the *'weedout' method* for the group 3 floe, which was sampled at Julian Day 249 in the Amundsen Sea. The scatter of the different subset means at a given subsampling degree n (the number of possible subsets increases with n, while the number of data points per subset decreases) is illustrated by Figure III.3a, b and c. At $n = 1$ the 95% error intervals of the original, not subsampled data sets are marked. It can generally be seen that the scatter increases considerably between $n = 5$ and $n = 10$. To obtain a clearer picture of the scatter variability with increasing subsampling spacing n the standard deviation of the mean values in Figure III.3a, b and c were computed and are graphed in Figure III.3d, e and f respectively. In the following this quantity is abbreviated as *std*. The random statistical standard error of the means is drawn as a solid line in Figure III.3d, e and f for comparison. It can be seen that the *std* of freeboard values is closest to the solid line (Figure III.3e), followed by the *std*s of the ice thickness values (Figure

III.3d) and the snow thickness values (Figure III.3f), which are both systematically below the solid line. The same trend was observed for the floe which is representative of group 2, while all the values (freeboard, ice and snow thickness) of the group 1 floe were in close vicinity of the solid line. *Std*s for the group 1 and group 2 floes' ice thicknesses are presented in Figure III.4a and b, respectively.

Figure III.5a and b show the *std*s of the group 3 floe for the two other subsampling methods *'random'* and *'sectional'*. The solid line again represents the expected standard error associated with the subsampling. In Figure III.5a it can seen that if m data point are randomly picked, they are closely distributed around the line of the standard error. This was similarly observed for the *std*s of the mean snow thickness and freeboard values, as well as for the corresponding *std*s of the group 1 and group 2 floes. Figure III.5b shows that for the third sampling method (subsections of m successive points along a profile) the *std* of the mean ice thickness values is generally above the expected random error line. This was found for the *std*s of mean values of snow thickness and freeboard as well as for the respective values of the group 2 floe. In contrast, the corresponding *std*s of the mean freeboard, ice and snow thicknesses for the group 1 floe were observed to be close to the random error line.

It can be concluded that among the three subsampling methods presented the *'sectional'* method involves the largest errors, especially for medium and strongly deformed floes. This finding is probably related to the fact that the subsampled sections in this case are too short in comparison to a minimum spatial scale which is required for stationary means of ice and snow thickness. This minimum spatial scale generally increases as ice becomes more deformed. The sampling error of the *'random'* method decreases with the number of sampled points according to the theoretically expected statistical error. In general the *'weedout'* method seems to perform best, with a smaller sampling error than predicted by random statistics.

There are marked differences between ice, snow and freeboard data with respect to subsampling. For the *'weedout'* method, the sampling error for the freeboard values was close to the theoretical random error, while sampling errors of ice and snow thickness were considerably smaller. This finding can be interpreted with the help of the roughness differences between snow, freeboard and ice. As shown in [*Adolphs*, 2] the freeboard line, which defines the ice surface with respect to the water line, was shown to contain the highest contribution of short-wave roughness in contrast to the snow and ice underside surface. As a consequence of this, the freeboard has the shortest 'spatial memory'; it seems to be the most uncorrelated and hence the most randomly distributed quantity (Figure III.3f). The snow thickness on this particular group 3 floe seems, on the other hand, to be the most correlated and coherent quantity, as its subsampling error increases much slower than the solid line. This is in agreement with the findings in [*Adolphs*, 2] where the snow surface of this floe was shown to be smoother at short wavelengths than the ice underside. In conclusion, this investigation suggests that the best strategy for reducing data collected on individual floes while introducing the least additional error, is to regularly increase the data point spacing while keeping the total profile length at 50-100 m. However, it should be restated that such subsampling will cause loss of roughness information at shorter wavelengths.

III.3.2.3 results for the early winter Ross Sea cruise

Considering the data for the different floe groups (1 to 3) of a whole cruise, the effect of the *'weedout'* subsampling method on the mean values can be investigated. For that purpose the early winter Ross Sea cruise was selected as it contains the largest number of floes. Figure III.6 shows the scatter graphs of mean ice and snow thicknesses for the *'weedout'* method. The standard error intervals (95% confidence), inherent in the full data sets (1 m spacing) are again indicated at $n = 1$. Comparison of these error intervals with the increasing spread in the subset means (with increasing n) shows that the deviations around the original mean value are generally smaller than the standard error up

to at least $n = 10$. Snow thickness shows less scatter in the subset means than ice thickness and is even more tolerant to subsampling. For fixed n the scatter is only slightly larger for group 2 than for group 1 and this is true for both ice thickness and snow thickness values (Figure III.6a, b, d and e). In contrast, the scatter is markedly larger for group 3 (Figure III.6c and f). However, this may stem partly from the fact that group 3 contains only five floes, which also enlarges the error confidence bar. Nevertheless, there seems to be a tendency towards more scatter with increasing deformation. The same trend was also observed between group 1 and group 2 of the late winter Ross and Amundsen/Bellingshausen Seas; group 3 showed even more scatter for these two cruises (compared to Figure III.6e, f) as it contained only two floes.

Another variety of the *'weedout'* method will be pursued now. Instead of subsampling along profile lines in terms of spacing, it will be subsampled on the 'floe' level. This means at $n = 2$ every second floe is picked, at $n = 3$ every third and so on. The resultant scatter in the corresponding subset means for ice, snow and freeboard, as a function of n are graphed in Figure III.7a, b and c for the early winter Ross Sea cruise. Solid lines indicate minimum and maximum scatter at each n; the inherent standard errors of the full data sets are again graphed at $n = 1$. In view of the results of Figure III.7 it can be concluded that collecting less data on the 'floe' level by factors of up to $n = 3$ (or at the most $n = 4$) seems to be 'safe' in the sense that the additionally introduced subsampling error is smaller than the inherent standard error of the original data sets.

III.4 Statistical properties of the shipboard observations (Set B)

III.4.1 Subsets: equidistant sub-sampling

For the continuous shipboard observations, 25 snow and ice thickness estimates were acquired hourly (details see [*Adolphs*, 1]). To make these observations spatially equidistant, only one of these sets per 10 km segment of the cruise track was used to form

the *Set B* data. For the early winter Ross Sea cruise the *Set B* data was then divided into seven distance classes from the ice edge (at distance 0 km) to the continent (at 1200 km). A pattern of increasing ice thickness was observed from the ice edge towards the inner pack ice followed by a sharp decrease from there to the continent. For brevity, three representative distance classes were selected and are exclusively used: the observations close to the ice edge (0-200 km, class 1), the thickest inner pack ice class (800-1000 km, class 2) and the thin ice class close to the continent (1200-1300 km, class 3). Analogous to the application of the *'weedout'* method at the 'floe' level in section 2.2.3, this method is applied, with individual shipboard observation sets corresponding to floes. Subsets containing every *n*th observation set are formed. As one set represents a 10 km observation interval, a subsampling degree of n approximately corresponds to a spatial resolution of $n \times 10$ km.

Analogous to Figure III.7, curves of minimum and maximum spread in mean ice and snow thickness, are presented in Figure III.8 as a function of subsampling degree n for the three selected distance classes. With the exception of a few statistical fluctuations the spread of the mean thickness values generally increases with subsampling degree n. Class 1 shows the least spread, because of the fact that it includes the highest number of observations. If the inherent standard error (95% confidence) at $n = 1$ is compared to the minimum and maximum line for each class, then, similar to the results of the floe subsampling (Figure III.7), the observation set subsampling seems to be tolerant to subsampling of degrees up to $n = 3$ or $n = 4$.

III.5 Distribution functions

This far, the focus has been on how specific sampling methods and spatial resolutions can be expected to affect the associated subset means and their standard deviations. In this sense two sampling strategies are judged to be 'equivalent' to another if the scatter of their respective subset means and standard deviations were reasonably close. While the

first and second statistical moments of data *sets A* and *B* turned out to be relatively robust towards subsampling, at least at the cruise level, the detailed shapes of the PDFs are much less so. On the other hand a qualitative analysis of PDF shapes for different sampling strategies is difficult as it depends on subjective decisions whether observed differences are numerical artifacts or significant results. The uneven loss of information between mean values and PDF shapes with increasing subsampling makes it desirable to know what creates the detailed shape of a PDF. Hence it is interesting to investigate how different sea ice formation processes determine the shape of a PDF. For this purpose the complete *Set A* and *Set B* data of all three cruises (early and late winter Ross Sea cruise, late winter Amundsen/Bellingshausen Seas cruise) will be considered in the following. First an attempt is made to find a common theoretical probability distribution that describes the different PDFs. Second, a simple statistical ice thickness model is developed to reveal the different effects of thermodynamic and deformational ice growth processes on the shape of a PDF. Modeled PDFs are found that resemble the observed ones. This allows one to intercompare the observed PDFs in terms of the corresponding model parameters.

III.5.1 Theoretical distribution functions

Three theoretical distributions (normal, lognormal and gamma) [*Bronstein and Semendjajew*, 1985; *Ostle and Malone*, 1988] were fitted to the measured distributions of *Set A* and *Set B* for all cruises. All three distributions are determined by two parameters, a and b, for the normal (Gaussian) distribution these parameters are identical to the mean and standard deviation, calculated over the interval $[-\infty, \infty]$. For all distributions a and b were calculated from the condition that the mean and standard deviations of the theoretical distributions (calculated over the interval $[0, h_{max}]$, with h_{max} being the maximum measured ice thickness) agree with those of the data.

Figure III.9 shows the ice thickness distributions of *Set A* and *Set B* data for all three cruises. The three calculated theoretical distributions are drawn in each graph and can be

compared to the measured PDF. Mean values and standard deviations of the measured PDF and the parameters of the fitted distributions are presented in Table III.1.

A Kolmogorov-Smirnov test was performed [*Conover*, 1980] that tests the null hypothesis as to of whether the data obey the statistics of the theoretical distributions (with parameters *a* and *b* from Table III.1). The probability measure for this test is defined as

$$T = \sup_h |F(h) - S(h)|.$$

Here, $\sup_h$ stands for supremum over the continuous range $h \in [h_{min}, h_{max}]$ that is covered by the M individual data points h_i, i = 1 to M, and F, S are theoretical and empirical cumulative distribution functions (CDF), respectively. $F(h)$ is given by the integral over the theoretical distribution function (PDF), $f(h)$

$$F(h) = \int_{-\infty}^{h} f(h')\,dh',$$

while $S(h)$ is given by the ratio of the number of data points h_i smaller than h and the number of all data points

$$S(h) = \frac{1}{M} \sum_{h_i < h} 1 \quad .$$

The hypothesis $S(h) = F(h)$ is rejected on the 1-α confidence level if $T > T_0$, where T_0 is the critical value of the test statistics T for the corresponding α. For $\alpha = 0.1$ (90% confidence) and number of observations *n.o.* >>40 (*n.o.* > 1000 for all data sets in Figure III.9) T_0 is well approximated by

$$T_0 = \frac{1.22}{\sqrt{n.o.} + \sqrt{n.o./10}}.$$

Results for T and T_0 are given in Table III.1. They show that the null hypothesis is clearly rejected ($T > T_0$) in all cases, indicating that none of the theoretical distributions fits the data in a pure statistical sense. However there is a 'hierarchy of rejection' for the different distributions. T for the log normal and gamma distributions is mostly an order of

magnitude less than T for the normal distribution. This agrees with a visual inspection of the graphs in Figure III.9 from which it is evident that for all sets of the drilling data (Figure III.9a, b and c) the gamma and/or lognormal distribution provide good fits while the normal distribution provides a poor fit. For the shipboard observations (Figure III.9 d, e and f) the decision for the gamma or lognormal distribution seems to be less clear as the normal distribution fits somewhat better than in the case of the drilling data.

For the case of the Amundsen Sea drilling data (Figure III.9c) all three distributions give poor statistical representations. Therefore, for this particular data set, a superposition of two normal or two gamma distributions was also considered and the results are presented in Figure III.10 and Table III.2. The parameters a_1, b_1, a_2, b_2 of the two distributions and their relative strengths c_1 and $c_2 = 1 - c_1$ were determined by minimizing the least squares difference between the empirical and theoretical cumulative distribution functions (CDF). The empirical CDF and the resulting (best-fit) CDFs for two normal and for two gamma distributions are shown in Figure III.10a, while the corresponding PDFs are shown in Figure III.10b. The results of the Kolmogorov-Smirnov test in Table III.2 still show rejection of the null hypothesis: however the statistical representation of the data is improved nevertheless. On the other hand, the use of 5 free distribution parameters (a_1, b_1, a_2, b_2 and c_1) instead of just 2 casts doubt on whether this improvement is significant. However, the ice thickness model presented in the next section will lend considerable support to the idea that the ice thickness distribution is a superposition of a basic gamma distribution with several weaker distributions of more complicated structure.

III.5.2 Statistical ice thickness model

From the previous section it is evident that, generally, there is no simple theoretical probability distribution that matches the statistical properties of the ice thickness data sets close enough to pass the Kolmogorov-Smirnov test. This should not be particularly unexpected because the ice thickness distribution in a geographical area is governed by

several different sea-ice growth processes, each with distinct properties and distributions. Consequently the PDF may be a superposition of several probability distributions. In the following, a statistical ice growth model is developed that illustrates this effect. This model does *not* describe the sea ice growth processes in detail; instead it uses only the main characteristics of each process, which are necessary to predict its influence on the shape of the PDF.

III.5.2.1 Model description

The time evolution of a set of M ice thickness measurements is tracked in a geographic area that is large enough so that thermodynamic growth conditions (such as air temperature, oceanic heat flux) show significant spatial variation at most times. (For brevity we denote the ice thickness measurements as 'floes'; such a 'floe' represents a region of a real composite floe, that is small enough so that it could be represented by one ice thickness measurement). The 'floes' are sorted into i = 1 to N bins of width Δh = 10 cm. At time t, bin i contains n_i^t 'floes' which have thicknesses between $h_i + (\Delta h)/2$ and $h_i - (\Delta h)/2$. The influence of the different ice growth processes on the bin populations n_i^t is modeled as follows:

1. Thermodynamic growth:

Until time t+1, a fraction $a\frac{(h_0 - h_i)}{h_0}$ of the 'floes' in bin i will grow and 'move' to bin i+1 while a corresponding fraction of new 'floes' will 'arrive' from bin i-1. Both terms decrease linearly with increasing ice thickness; h_0 is an upper limiting ice thickness beyond which no more ice growth occurs. If thin ice is assumed to grow faster than thick ice the following linear relation is obtained

$$n_i^{t+1} = n_i^t\left[1 - a\frac{(h_0 - h_i)}{h_0}\right] + n_{i-1}^t a\frac{(h_0 - h_{i-1})}{h_0}, \qquad (1)$$

with a, ranging between 0 and 1, being the dimensionless parameter for thermodynamic growth. During all model runs presented later, h_0 is taken as a constant (350 cm). One could interpret h_0 as the thermodynamic thickness limit of multi year floes which depends on mean air temperature, oceanic heat flux, snow cover and other factors (which all depend on time). For short simulation times corresponding to first year ice (as is the case in this study) the model results are insensitive to the exact value of h_0 used. Besides, for thermodynamic growth the form of Equation (1) will be applicable also for gradual deformational processes whose likelihood decreases linearly with ice thickness. One example could be the aggregation of floes through collisions of pancake ice.

2. Lead formation:

At each time step a fraction bM is added to the first ice thickness bin to mimic the formation of new ice during pack ice expansion and lead formation,

$$n_1^{t+1} = n_1^t + bM \quad , \tag{2}$$

where b is the dimensionless parameter for lead formation, which ranges between 0 and 1.

3. Deformation: Ridging and rafting

During pack ice compression, rafting and ridging events diminish the population of thin ice below a threshold h_{th} by the formation of much thicker ice above this threshold. Significant deformation only occurs in ice below this threshold. At time t a fraction $c(h_{th} - h_i)$ of the floes in bin i will leave for bin $i \times R$ while an amount of $\frac{c}{R} n_{i/R}^t (h_{th} - h_{i/R})$ floes enters from bin $\frac{c}{R}$; R is the *thickening ratio* (dimensionless, see explanation below) and c is the parameter for the amount of deformation (ranging between 0 and 1). Summing up the two terms gives

$$n_i^{t+1} = n_i^t \left[1 - c \frac{(h_{th} - h_i)}{h_{th}} \right] + \frac{c}{R} n_{i/R}^t \frac{(h_{th} - h_{i/R})}{h_{th}} \qquad (3)$$

for the equation governing deformation.

Strictly, the thin ice threshold h_{th} is different for ridging and rafting. Using mean material properties of arctic sea ice, *Parmerter* [1974] derives that rafting should be largely restricted to ice thicknesses < 20 cm, even if occasionally, rafts of up to 100 cm thick ice have been observed [*Weeks and Kovacs*, 1970]. For ridging there is no true threshold, even very thick floes can continue to form a ridge provided that this ridge is already large enough to break the floe by isostatic imbalance [*Parmerter and Coon*; 1973]. However *Parmerter and Coon* [1973] also state that the vast majority of ridges form in thin ice (smaller than 20-50 cm thickness). Here, h_{th} = 50 cm is used, describing ridging and rafting as one combined process

The thickening ratio also depends on the type of deformation process. For rafting of equally thick floes R is about 2, which represents a minimum value, while maximum values of R equal to about 8 are obtained for ridges that reach limiting height within the kinematic ridge model of *Parmerter and Coon* [1973]. For a lead containing 20 cm thick ice the resulting ridges of maximum height are therefore about 160 cm high. Values between the extremes $R = 2$ and $R = 8$ should yield effective values for a combination of ridging and rafting.

III.5.2.2 Results

In the following, a series of model runs is discussed. At time $t = 0$ the first bin contains $n_1 = 500$ floes while all the other bins are empty. One can then study the influences of the parameters a, b and c (representing the respective amounts of thermodynamic growth, lead formation and ice deformation) on the shape of the resulting PDF. For instance, Figure III.11a, b and c show the time evolution of the special case, where just thermodynamic growth is considered ($a = 0.35$, b and c are zero). Equation (1)

corresponds to a diffusive process with a rigid wall on the left (non-existence of negative ice thicknesses). From the initial stage at time $t = 0$ (Figure III.11a) the ensemble of floe thicknesses develops first into a gamma distribution (Figure III.11b) which then evolves into a normal distribution (Figure III.11 c). In the next model run, new ice formation ($b > 0$) was added to the scenario. This is considered in Figure III.11d, e and f. The resultant ice thickness PDF after time step $t = 25$ for a lead formation parameter $b = 0.03$ is shown in Figure III.11d. In comparison to Figure III.11c the thin ice bins are clearly increased at the cost of a little less medium thick ice as shown by the more asymmetric and flatter shape in Figure III.11d. As a last process ridging and rafting are added to the scenario of Figure III.11d. The deformational parameter was chosen as $c = 0.015$ and the thickening ratio R was chosen equal to 2 in the first run (Figure III.11e) and equal to 4 in the second run (Figure III.11f). As can be seen in both Figure III.11 e and f, a thick ice tail (to the right) has developed after time step $t = 25$ for $R = 2$. This tail illustrates the efficient transfer of 'floes' from thin to thick ice bins by deformation. For $R = 4$ this transfer is even more efficient leading to a stronger thick ice tail.

By understanding the different processes and their influence on the shape of the distribution an attempt was made to reproduce the principal traits of the ice thickness distribution of the three cruises. The results of this modeling attempt can be seen in Figure III.12 a, b and c. For both Ross Sea cruises essentially the same set of parameters (a=0.35, $b = 0.01$, $c = 0.015$ and $R = 3$) was selected. After time step $t = 20$ a PDF results (Figure III.12 a), which is similar in shape to the drilling PDF of the early winter Ross Sea cruise (Figure III.9 a) but includes somewhat more thin ice. After time step $t = 32$ the shape of the PDF has not changed very much as compared to $t = 20$ (Figure III.12a) but has shifted to the right (Figure III.12b). This reproduces the principal difference between the *Set A* PDFs of Figure III.9 a and b. In order to reproduce the PDF of the late winter Amundsen and Bellingshausen Seas a different set of parameters was chosen, with more thin ice formation in leads ($b = 0.04$), more deformation ($c = 0.03$) and higher thickening

ratio ($R = 5$). The result of this simulation at time step $t = 35$ can be seen in Figure III.12c. One sees in comparison to Figure III.9c that the modeled PDF does reproduce important characteristics of the measured PDF, for example the extended tail towards higher ice thicknesses and hence the general asymmetric shape. The fact that there is more thin ice in the modeled PDF than in the field data is undoubtedly the result of the fact that the model, unlike the drilling data [*Adolphs*, 1], does not contain a bias against ice thinner than 30 cm, which was generally not sampled.

In conclusion it can be stated that this simple statistical ice thickness model does adequately simulate the relevant influences of major ice formation processes on the PDF. The model allows the principal characteristics of the real data PDFs to be modeled. In addition, the selected sets of parameters for the Ross and the Amundsen/Bellingshausen Seas show that lead formation and deformation are important in the latter area while the relative contribution of thermodynamic ice growth is more important in the Ross Sea. This agrees well with the finding of previous studies, where much higher amounts of congelation ice growth were discovered in the calmer Ross Sea embayment [*Jeffries and Adolphs*, in press]. This is in contrast to the Amundsen/Bellingshausen Sea region which is prone to more divergent and convergent ice motion, which leads to increased new ice formation and ridging/rafting, respectively [*Adolphs*, 1]

III.6 Conclusions

Two different sets (*Set A* and *Set B*) of snow and ice thickness data, which were acquired during three cruises in the Ross, Amundsen and Bellingshausen Seas were examined regarding statistical tolerance with respect to different subsampling methods. The results can be summarized as follows.

The *Set A* (drilling data) behaved isotropically, which means that changes between mean thicknesses along profile lines of equal length were independent of the direction of the profile lines.

Three different subsampling methods were tested along profiles from representative floes. Among these methods the first *'weedout'* subsampling strategy performed best. According to this strategy drilling points are spaced farther from each other with increasing subsampling degree n (equivalent to a spacing of n m). The subsampling error was found to increase slower with increasing n than the random statistical standard error. This is due to spatial coherence in the snow and ice thickness profiles.

Considering the scatter in the means of ice and snow thickness of *'weedout'* subsets taken from each floe during the whole cruise, it was shown that subsampling errors remain usually within the 95% confidence intervals of the original data sets up to a subsampling degree of $n = 10$.

'Weedout' on the 'floe' level, i.e. picking every n-th floe for a subsampling degree n suggests that mean thickness values of a whole cruise are generally tolerant (within 95% confidence interval) to subsampling up to degree n = 3. The *Set B* (shipboard observations) were similarly subsampled on the level of individual observation sets. The effect of increasing subsampling degree n (equivalent to picking every n-th observation set, which corresponds to a spatial interval of $n \times 10$ km between individual sets) on the statistics of three representative distance classes (defined in terms of distance from the ice edge) of the early winter Ross Sea cruise was studied. Mean ice and snow thicknesses stayed within the 95% error interval up to subsampling degrees of $n = 3$ or 4.

Theoretical probability distributions (normal, lognormal and gamma) were fitted to the ice thickness PDFs of the field data. The lognormal and gamma distributions fitted the drilling data better than the normal distribution. A simple statistical ice thickness model was developed in order to learn how different ice growth and development processes influence the shape of the ice thickness PDF. The principal characteristics of the real data PDFs could be simulated using sets of model parameters, which are consistent with the relative acquisition times of the different data sets and observational evidence on the degree of ice deformation.

III.7 References

Adolphs, U., Spatial and temporal variability of snow and ice thickness in the South polar Pacific Ocean, thesis paper 1.

Adolphs, U., Roughness variability of sea ice and snow cover thickness profiles in the Ross, Amundsen and Bellingshausen Seas, thesis paper 2.

Bronstein, I.N. and K.A. Semendjajew, Taschenbuch der Mathematik, 838pp, Teubner, 1985.

Conover, W.J., Practical nonparametric statistics, 493pp, Wiley & Sons, 1980.

Eicken, H. and M.A. Lange, Sea ice thickness data: the many vs. the few, *Geophys. Res. Lett.*, *16*(6), 495-498, 1989.

Jeffries, M.O. and U. Adolphs, Early winter ice and snow thickness distribution, ice structure and development of the western Ross Sea pack ice between the ice edge and the Ross ice shelf, *Antarc. Sci.*, *9*(2), 1997, in press.

Lange, M.A. and H. Eicken, The sea ice thickness distribution in the Northwestern Weddell Sea, *J. Geophys. Res.*, *96*(C3), 4821-4837, 1991.

Ostle, B. and L.C. Malone, Statistics in Research, Iowa State University Press, 651pp, 1988.

Parmerter, R.R., A mechanical model of rafting, *Aidjex Bulletin*, *23*, 97- 115, 1974.

Parmerter, R.R. and M.D.Coon, Mechanical Models of ridging in the Arctic sea ice cover, *Aidjex Bulletin*, *19*, 59-98, 1973.

Weeks, W.F. and A. Kovacs, On pressure ridges, Report for the U.S. Army Cold Regions Research and Engineering Laboratory, Hanover, N.H., 1970.

Worby, A.P., M.O. Jeffries, W.F. Weeks, K. Morris and R. Jana, The thickness distribution of sea ice and snow cover during late winter in the Bellingshausen and Amundsen Seas, Antarctica, *J. Geophys. Res.*, *101*(C12), 28,441-28,455, 1996.

III.8 Figures

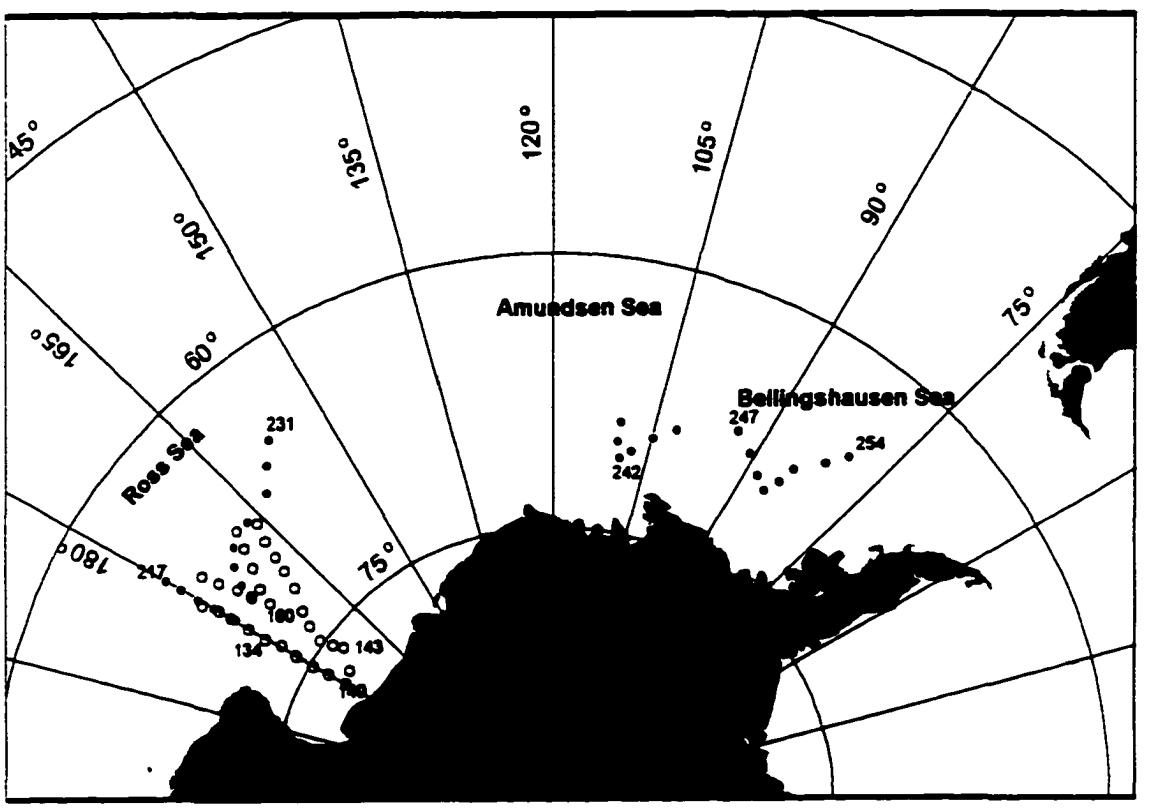

Figure III.1: Ice stations along three track lines followed by the Nathaniel B. Palmer (NBP) between May and September 1995. NBP 95-3 (open circles) visited the Ross Sea in early winter (May/June 95), NBP 95-5/1 (filled circles) in late winter (August 95). During cruise NBP 95-5/2 (September 95) a track of another 14 ice stations was laid out in the Amundsen/ Bellingshausen Seas.

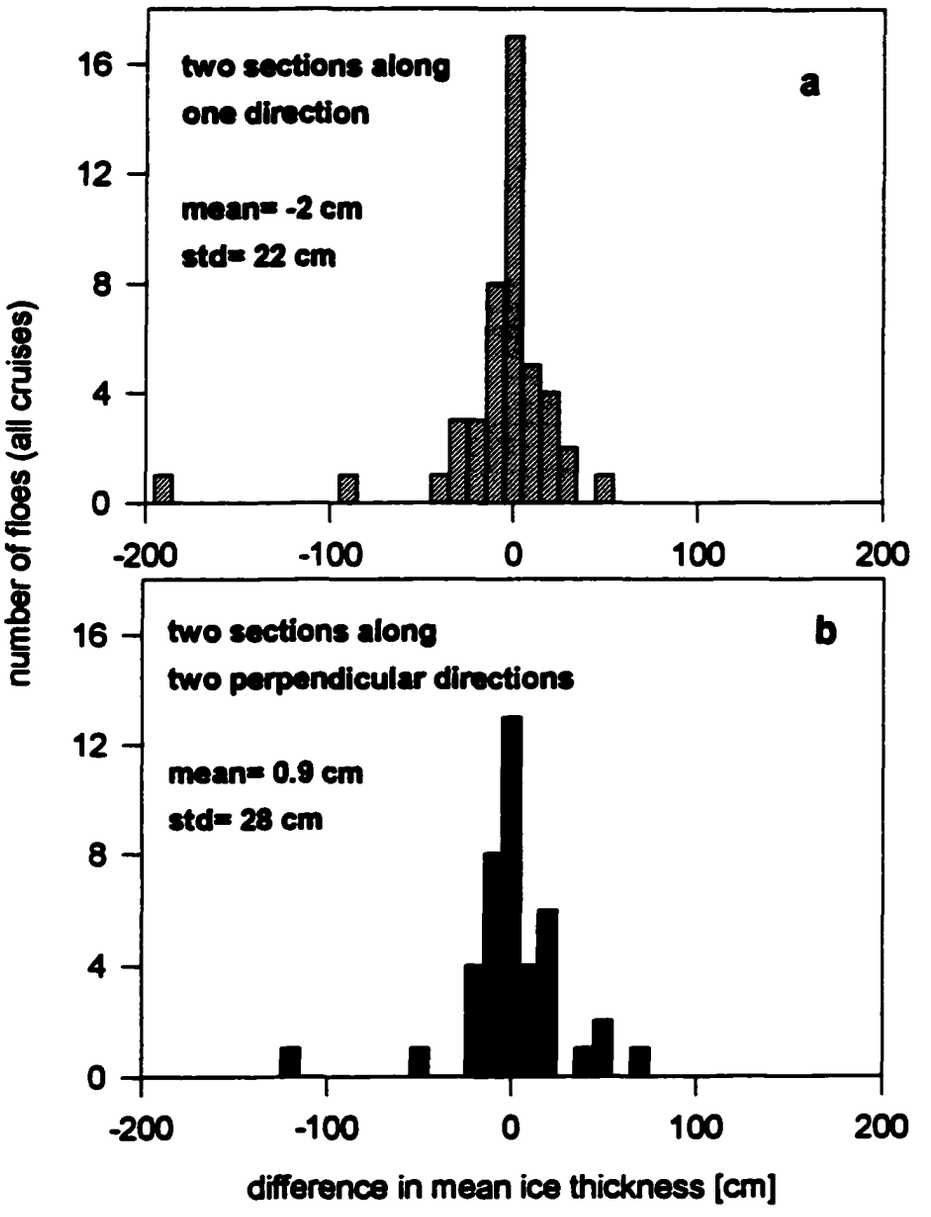

Figure III.2. Histograms of mean value differences between two profile sections, (a) parallel and (b) perpendicular to each other, for all floes of all cruises. Individual sections consist of 50 holes spaced at 1 m distance.

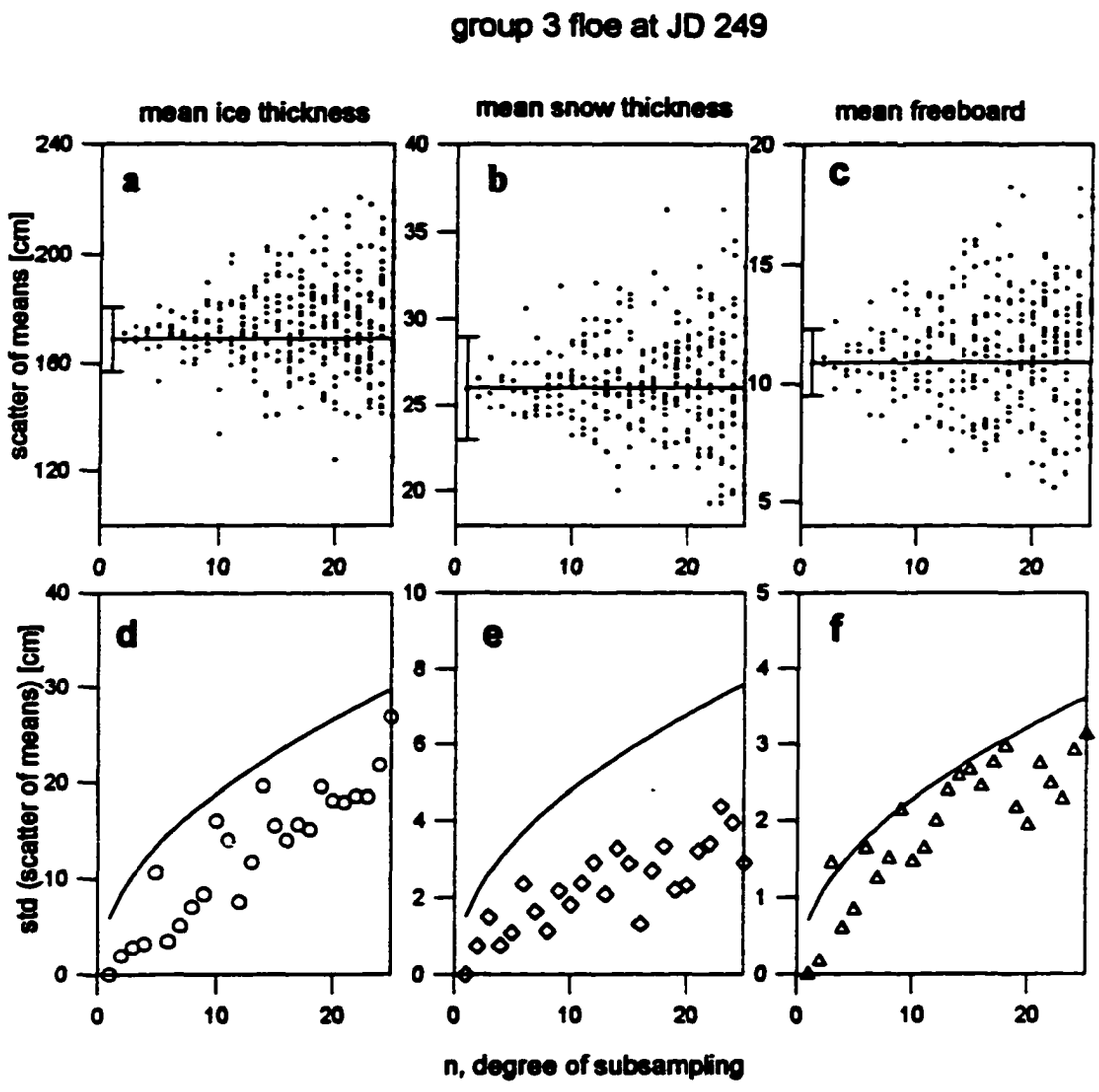

Figure III.3. Scatter of mean ice thicknesses (a), mean snow thicknesses (b) and mean freeboard (c) as a function of the subsampling degree *n* for a representative group 3 floe, sampled at Julian Day 249 in the Amundsen/Bellingshausen Seas. The *'weedout'* method was used, i.e. *n* corresponds to a hole spacing of *n* meters. The corresponding standard deviations of the subset means (*stds*) are graphed in figures (d), (e) and (f) and can be compared to the theoretical expected additional random error for given n (solid line). Error bars at *n* = 1 in (a), (b) and (c) indicate 95% confidence intervals for the original (not subsampled) data set, horizontal lines (solid lines) in (a), (b) and (c) indicate the constant means as reference.

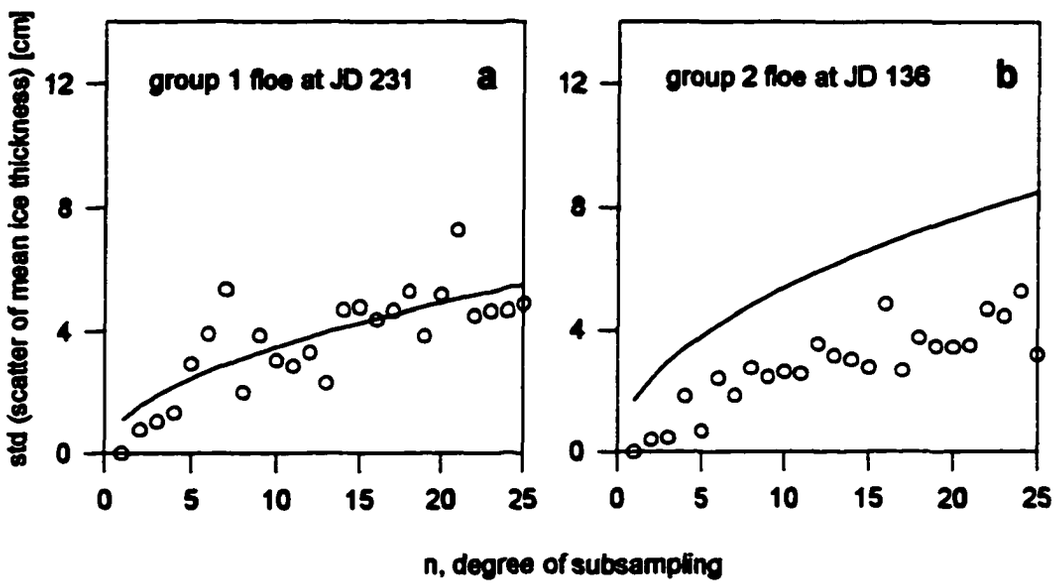

Figure III.4. Standard deviations (*std*) of mean ice thicknesses for representative floes of (a) group 1 and (b) group 2 obtained, using the *'weedout'* method. They can be compared to the standard error lines (solid lines).

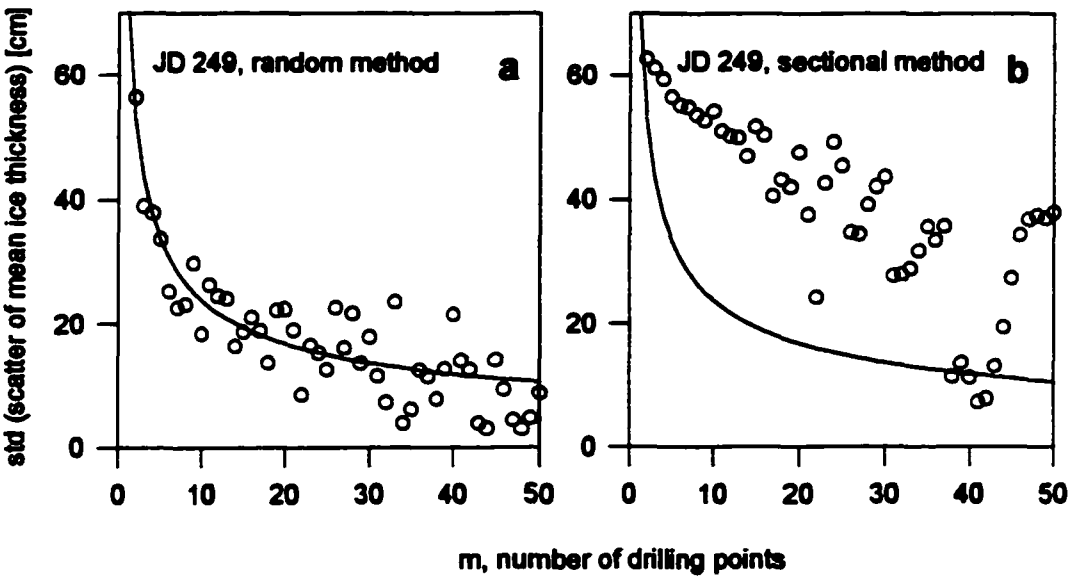

Figure III.5. Standard deviations of the subset means (*stds*) of ice thickness are graphed for the group 3 floe as a function of *m*, the number of selected drilling points for the (a) *'random'* and (b) *'sectional'* subsampling methods. *Stds* are closely distributed along the expected additional standard error for a given *m* (solid line) for the *'random'* method (a) while they deviate substantially for the *'sectional'* method (b).

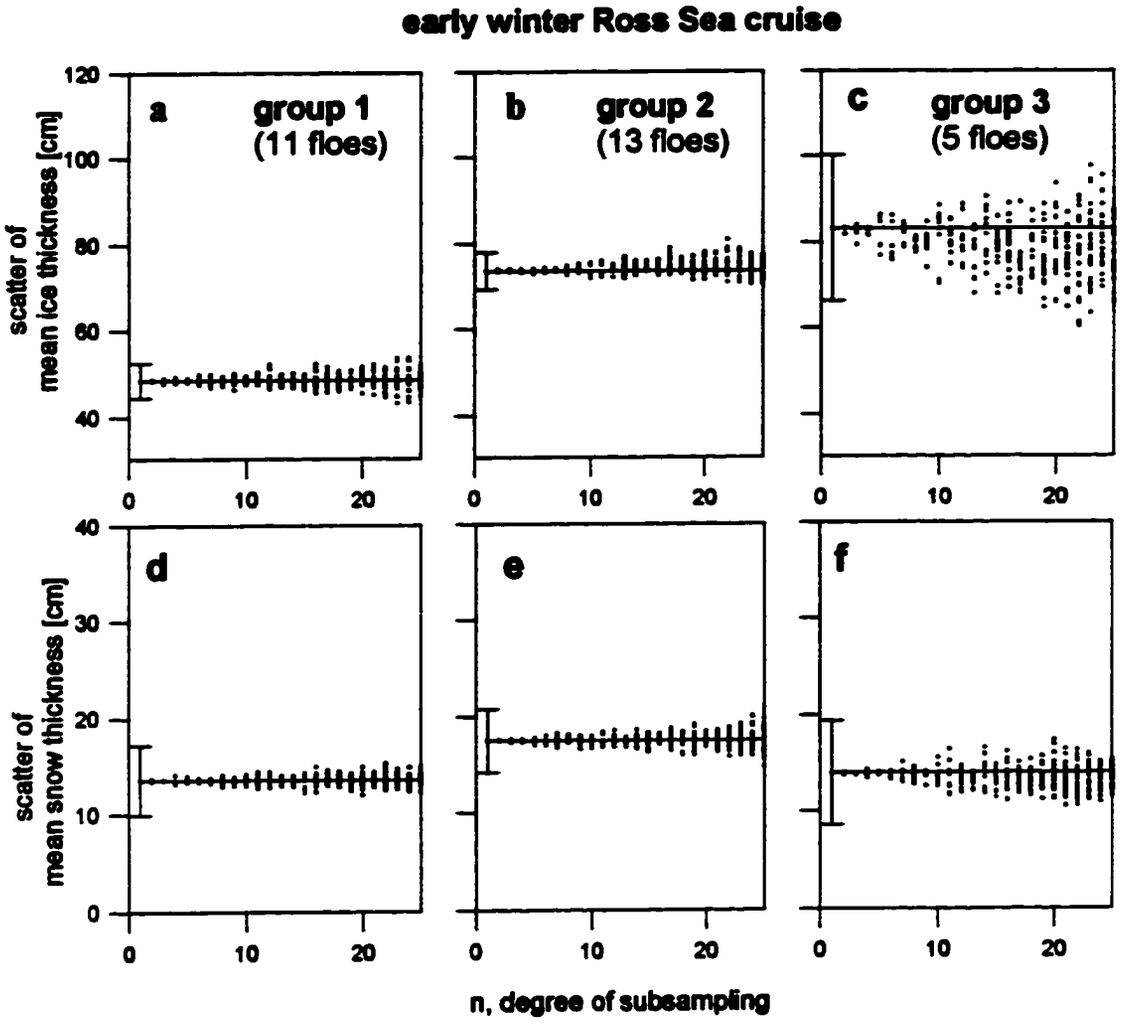

Figure III.6. Scatter graphs of mean ice (a),(b) and (c) and snow thicknesses (d), (e) and (f) for the three deformational floe groups of the early winter Ross Sea cruise using the 'weedout' method. 95% confidence error bars of the original data sets are given at n = 1, horizontal lines (solid lines) indicate the constant means as reference.

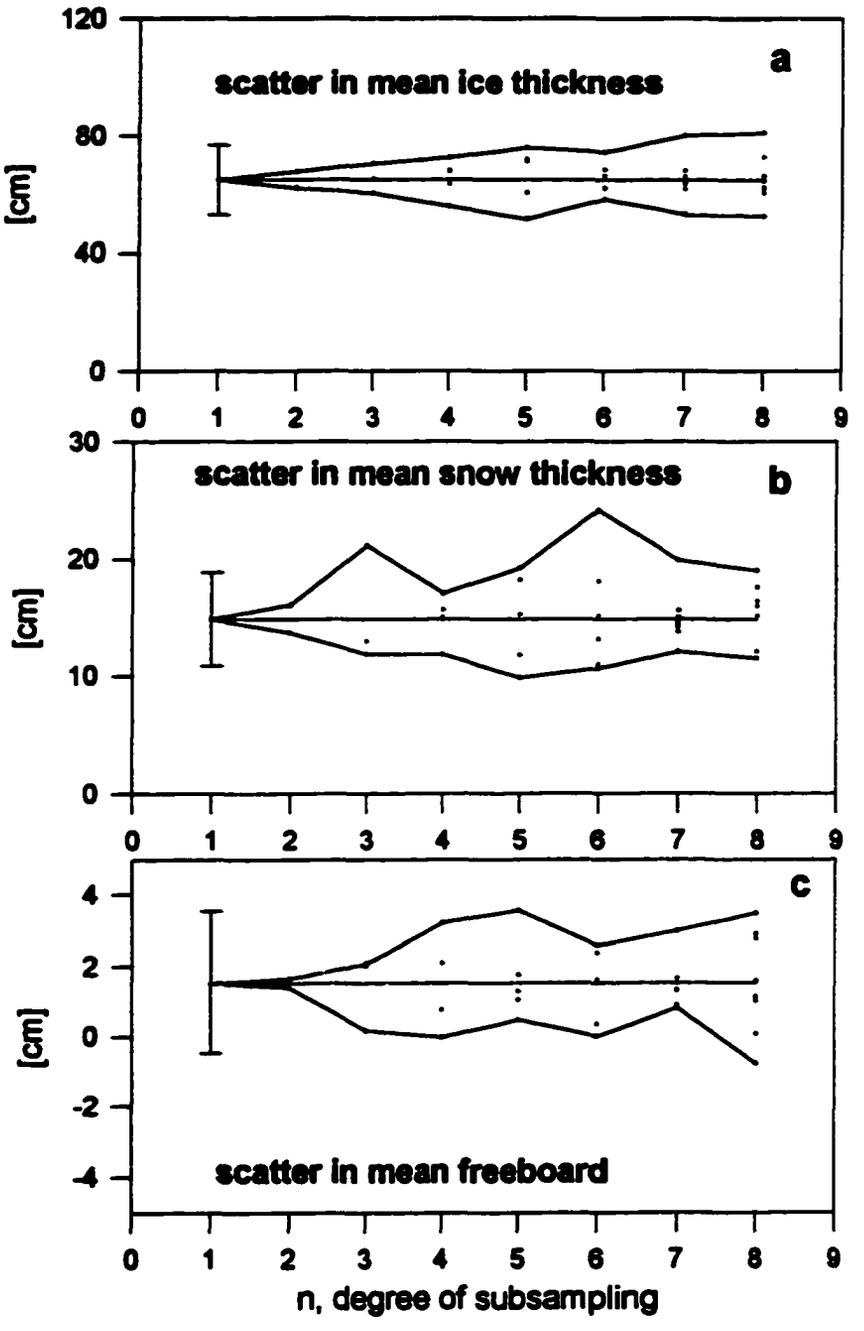

Figure III.7. Subsampling of the drilling data of the early winter Ross Sea cruise on the 'floe' level using the *'weedout'* method. The subset means of ice thickness, snow thickness and mean freeboard, together with lines of maximum and minimum scatter (solid lines) are graphed against subsampling degree *n* (on the 'floe' level this corresponds to picking every *n*th floe to obtain a subset). 95% confidence error bars (for the original data set of all 29 floes) are given at *n* = 1, horizontal lines (solid) indicate the constant means as reference.

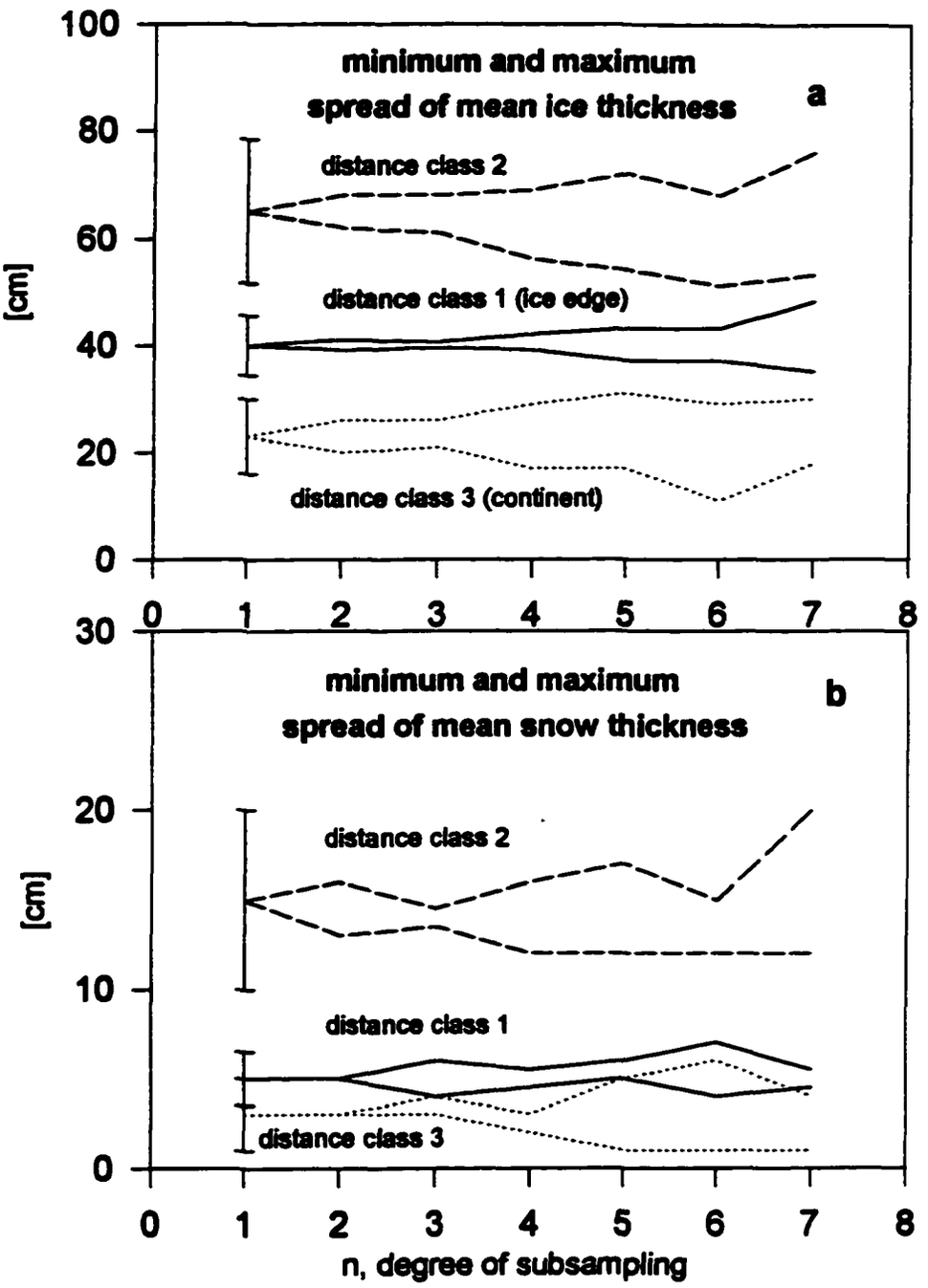

Figure III.8. Shipboard data (Set B) of the early winter Ross Sea cruise: The minimum and maximum spread of the subset means of ice and snow thicknesses plotted against subsampling degree *n* (here every *n*th observation set was picked to obtain a subset) for three selected distance classes (data sorted in terms of distance from the ice edge). 95% confidence intervals of the complete data set is given at *n* = 1.

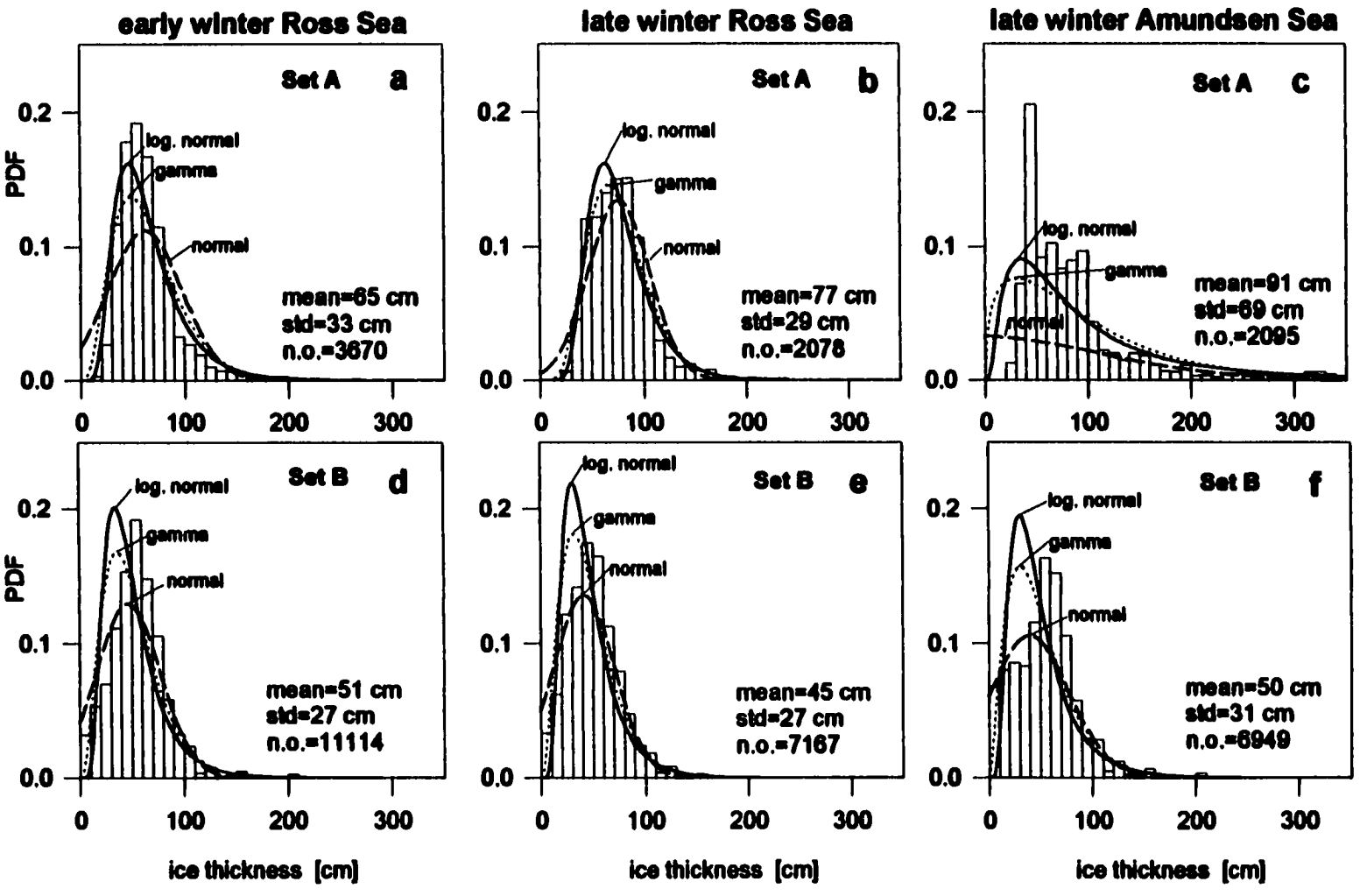

Figure III.9. Ice thickness PDFs of Set A and Set B data in comparison to three theoretical distributions (normal, lognormal and gamma) with optimum parameters a and *b* (Table III.1) for all three cruises. Mean values, standard deviations (*std*) and the number of observations (*n.o.*) for the field data are also given.

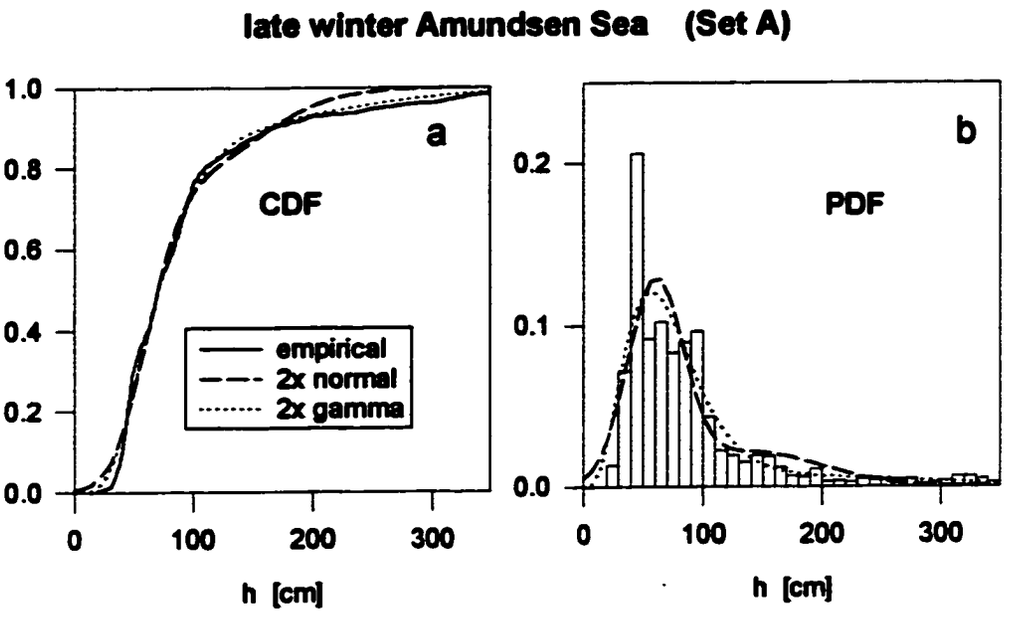

Figure III.10. Cumulative distribution functions (CDF) and probability density functions (PDF) for the drilling data of the late winter Amundsen Sea (empirical) and for a superposition of either two normal or two gamma distributions (theoretical). As can be seen in Table III.2 the Kolmogorov-Smirnov test performs better for the gamma distributions fit.

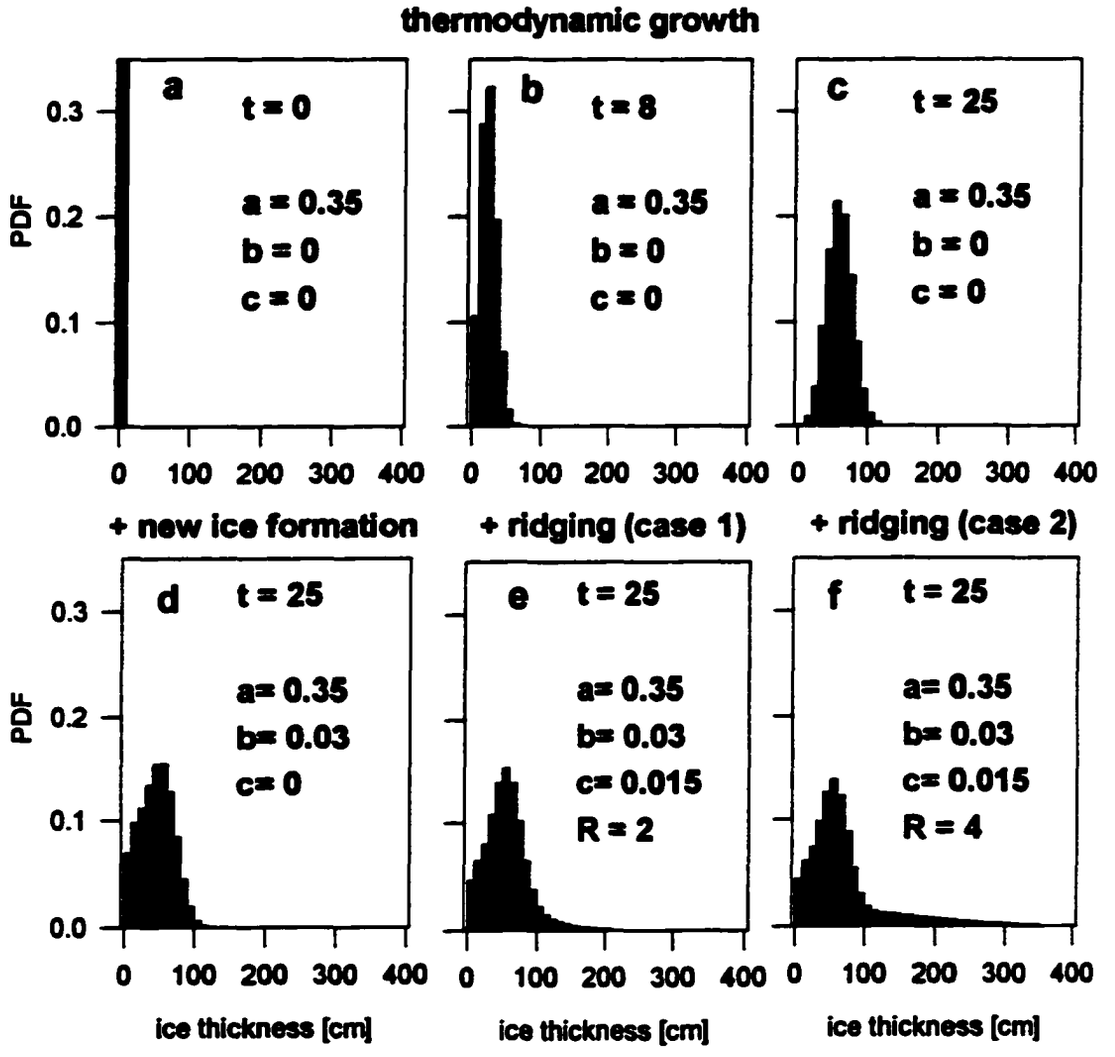

Figure III.11. Theoretical runs of the statistical ice thickness model, with parameters *a* (for thermodynamic growth), *b* (for the amount of lead formation), *c* (representing ice deformation) and *R* (dimensionless, ridging thickening ratio); (a), (b) and (c) shows the time evolution (time step $t = 0$, 8 and 25) considering only thermodynamic growth (b, $c = 0$); in (d) new ice formation in leads is included; and in (e) and (f) ridging with different thickening ratios is considered.

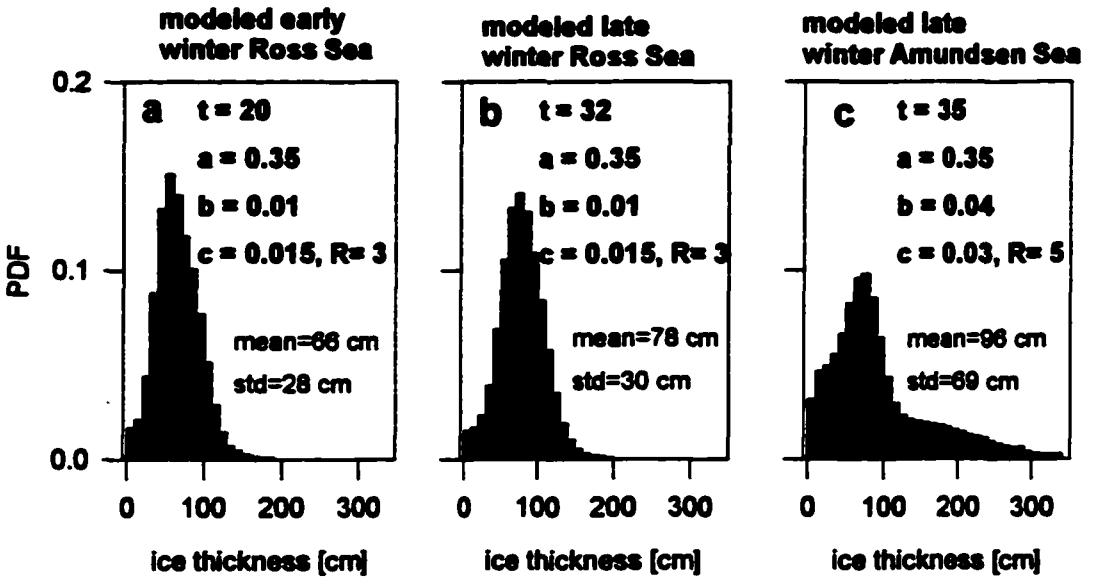

Figure III.12. Simulations of the characteristic traits of the ice thickness PDFs of the early and late winter Ross Sea and the late winter Amundsen/Bellingshausen Seas using the statistical ice thickness model. Model parameters (*t*, *a*, *b*, *c*, *R*) and mean values as well as standard deviations (*std*) are given for the modeled PDFs.

III.9 Tables

Table III.1. Distribution parameters and results of the Kolmogorov-Smirnov test

			normal			log. normal			gamma			
Cruise	mean [cm]	stdev. [cm]	a [5]	b	T [4]	a	b	T	a	b	T	T_0
Ro1 [1] (Set A)	65	33	62.0	35.5	0.156	4.1	0.48	0.087	4.0	16.4	0.091	0.020
Ro1 (Set B)	51	27	46.7	30.7	0.089	3.8	0.51	0.086	3.4	14.7	0.078	0.011
Ro2 [2] (Set A)	77	29	76.2	29.7	0.075	4.3	0.37	0.051	6.9	11.1	0.042	0.027
Ro2 (Set B)	46	26	41.4	29.3	0.118	3.7	0.52	0.055	3.2	14.3	0.038	0.014
Am [3] (Set A)	92	70	-10.2	122.0	0.617	4.3	0.86	0.157	1.5	64.5	0.178	0.027
Am (Set B)	50	31	40.1	37.7	0.152	3.7	0.57	0.144	2.6	18.9	0.097	0.015

[1] early winter Ross Sea (May/June 1995)

[2] late winter Ross Sea (August 1995)

[3] late winter Amundsen and Bellingshausen Seas (August/ September 1995)

[4] T is the Kolmogorov-Smirnov probability measure, $\sup_h |F(h)-S(h)|$. Here, h is the data, and F, S are theoretical and empirical cumulative functions (CDF), respectively. The hypothesis S(h) = F(h) is rejected on the 90% confidence level if $T > T_0$.

[5] units of a, b depend on distribution type: normal: [a] = cm, [b] = cm, gamma: [a] = 1, [b] = cm and log.normal: [a] = 1, [b] = 1.

Table III.2. Superposition of two distributions: results for *Set A* of the late winter Amundsen Sea.

distribution	a_1 [1)]	b_1	c_1 [2)]	a_2	b_2	c_2	T	T_θ
2x normal	60.6	23.0	0.70	141.8	56.9	0.30	0.065	0.027
2x gamma	4.95	14.31	0.88	5.92	38.00	0.12	0.056	0.027

[1)] units of a_i, b_i ($i = 1, 2$), depend on distribution type: e.g. normal: $[a_i]$ = cm, $[b_i]$ = cm, gamma: $[a_i]$ = 1, $[b_i]$ = cm.

[2)] c_i ($i = 1, 2$) indicates the relative strength of each distribution.